

UNIVERSITÄT HAMBURG  
DEPARTMENT PHYSIK

---

# Measurement of $Z$ Boson production with the ATLAS Experiment at the LHC

## Dissertation

zur Erlangung des Doktorgrades  
des Department Physik  
der Universität Hamburg

vorgelegt von

James Dassoulas

von der Insel Man

Hamburg

2014

Gutachter/in der Dissertation:	Dr. Alexandre Glazov Prof. Dr. Peter Schleper
Gutachter/in der Disputation:	Dr. Alexandre Glazov Prof. Dr. Erika Garutti
Datum der Disputation:	04. März 2014
Vorsitzender des Prüfungsausschusses:	Dr. Michael Martins
Vorsitzender des Promotionsausschusses:	Prof. Dr. Daniela Pfannkuche
Dekan des Fachbereichs Physik:	Prof. Dr. Heinrich Graener

## Abstract

A measurement of the differential  $pp \rightarrow Z/\gamma^* \rightarrow e^+e^-$  cross section as a function of di-electron invariant mass in the region  $66 < m_Z < 116$  GeV using  $4.58 \text{ fb}^{-1}$  of data collected at a center-of-mass energy of  $\sqrt{s} = 7$  TeV in 2011 with the ATLAS detector at the LHC is performed. The measurement is performed with a comprehensive treatment of systematic and statistical uncertainties evaluated using Monte Carlo simulation and data-driven techniques. The contribution from electroweak and  $t\bar{t}$  background processes is estimated using simulation, while the contribution from QCD backgrounds is estimated using a data-driven method. The measured cross section is compared with various theoretical predictions from parton distribution function (PDF) fits to next-to-next-to-leading order QCD calculations with next-to-leading order electroweak corrections. The precision of the measurement is of the order of 1 – 2% and provides strong PDF discrimination, with none of the state of the art PDFs showing good agreement with the data. The measurement can be used as an input to constrain future PDF fits.

A combination of separate electron and muon  $W^\pm$  and  $Z/\gamma^*$  cross section measurements is also presented, with full treatment of each channel's systematic uncertainties and the correlations between them. These measurements are performed as a function of lepton pseudo-rapidity and  $Z$  boson rapidity for the  $W^\pm$  and  $Z/\gamma^*$  production processes respectively. These serve as a precise probe of QCD dynamics and proton PDFs. The combined cross sections are compared with theoretical predictions and strongly discriminate between, and in some cases exclude, different PDF fits. The precision of the measurements is better than the PDF uncertainties, and NNLO QCD and NLO EW theory are limiting factors in interpretation of the data.

## Zusammenfassung

Eine Messung des differentiellen  $pp \rightarrow Z/\gamma^* \rightarrow e^+e^-$  Wirkungsquerschnitts als Funktion der invarianten Masse in der Region  $66 < m_Z < 116$  GeV wird durchgeführt. Dazu werden die bei einer Schwerpunktsenergie von  $\sqrt{s} = 7$  TeV im Jahre 2011 gesammelten Daten, die einer integrierten Luminosität von  $4.58 \text{ fb}^{-1}$  entsprechen, analysiert. Die Messung wird mit einer umfassenden Behandlung von systematischen und statistischen Unsicherheiten - durch Monte Carlo Simulationen und datengetriebene Techniken bewertet. Der Beitrag von elektroschwachen und  $t\bar{t}$  Hintergrundprozessen wird mit Simulationen geschätzt, und der Beitrag von QCD Hintergründen wird mit einer datengetriebenen Methode geschätzt. Der gemessene Wirkungsquerschnitt wurde mit verschiedenen theoretischen Vorhersagen von Partonenverteilungsfunktion (PDF) Fits für NNLO QCD Berechnungen mit NLO elektroschwachen (EW) Korrekturen verglichen. Die Präzision der Messung liegt bei 1 – 2% und bietet eine starke PDF Diskriminierung. Keiner der Fits ist in guter Übereinstimmung mit den Daten. Die Messung kann verwendet werden, um zukünftige PDF Fits beschränken.

Eine Kombination von separaten Elektron und Myon  $W^\pm$  and  $Z/\gamma^*$  Wirkungsquerschnitt-Messungen mit einer kompletten Behandlung von systematischen Unsicherheiten für jeden Kanal, und die Korrelationen wird präsentiert. Entsprechend wurden diese Messungen als Funktion der Lepton Pseudo-Rapidity und der  $Z$ -Boson-Rapidity für die  $W^\pm$  and  $Z/\gamma^*$  Prozess durchgeführt. Diese dienen als Präzisionsfühler der QCD Dynamik und Proton PDFs. Die kombinierte Wirkungsquerschnitte sind mit verschiedenen theoretischen Vorhersagen verglichen worden.

Die Präzision der Messungen ist besser als die PDF Unsicherheiten, und die NNLO QCD und NLO EW Theorien sind limitierende Faktoren bei der Interpretation der Daten.

*For my mother.*

# Contents

<b>List of Tables</b>	<b>iv</b>
<b>List of Figures</b>	<b>vii</b>
<b>1 Overview</b>	<b>2</b>
<b>2 Theoretical Introduction</b>	<b>3</b>
2.1 Introduction to the Parton Model . . . . .	3
2.1.1 Structure Functions and Scaling . . . . .	3
2.1.2 The Parton Model . . . . .	6
2.2 Quantum Chromo-Dynamics . . . . .	6
2.3 Parton Distribution Functions . . . . .	8
2.3.1 PDF Determination . . . . .	8
2.4 The Drell-Yan Process . . . . .	10
2.4.1 Z Boson Measurements . . . . .	14
2.5 Theoretical Predictions and Monte Carlo Generators . . . . .	17
<b>3 The Large Hadron Collider</b>	<b>19</b>
3.1 The LHC Accelerator Complex . . . . .	19
3.2 Beam Preparation . . . . .	20
3.3 Luminosity . . . . .	20
<b>4 The ATLAS Detector</b>	<b>22</b>
4.1 The Magnet System . . . . .	23
4.2 The Inner Detector . . . . .	24
4.2.1 The Pixel Detector . . . . .	25
4.2.2 The Semiconductor Tracker . . . . .	25
4.2.3 The Transition Radiation Tracker . . . . .	25
4.3 The Calorimeter System . . . . .	26
4.3.1 The EM Calorimeter . . . . .	27
4.3.2 The Hadronic Calorimeter . . . . .	29
4.4 The Muon System . . . . .	30
4.5 The Trigger System . . . . .	30
<b>5 Measurement of the <math>Z \rightarrow ee</math> Inclusive Cross Section</b>	<b>33</b>
5.1 Data Sample . . . . .	33
5.2 Monte Carlo Samples . . . . .	34
5.3 Cross-Section Measurement Definition . . . . .	36

5.4	Event Reconstruction and Selection . . . . .	38
5.4.1	Reconstruction of Electrons in ATLAS . . . . .	38
5.4.2	Electron Trigger . . . . .	38
5.4.3	Electron Reconstruction . . . . .	38
5.4.4	Electron Identification . . . . .	39
5.4.5	$Z \rightarrow ee$ Event Selection . . . . .	40
5.5	Electron Performance and Corrections . . . . .	44
5.5.1	Scale Factors . . . . .	44
5.5.2	Electron Energy Scale and EM Calorimeter Calibration . . . . .	44
5.5.3	Electron Energy Resolution . . . . .	46
5.5.4	Energy scale studies to improve electron $\eta$ distribution . . . . .	46
5.6	MC Corrections . . . . .	49
5.6.1	Pileup Reweighting . . . . .	49
5.6.2	$Z$ Boson $p_T$ Reweighting . . . . .	49
5.6.3	Primary Vertex $z$ Reweighting . . . . .	50
5.6.4	$Z$ Lineshape Reweighting . . . . .	51
5.7	Background Estimation . . . . .	53
5.7.1	$t\bar{t}$ and Electroweak Backgrounds . . . . .	53
5.7.2	Multi-jet Background Estimation . . . . .	54
5.7.3	Estimation Method . . . . .	54
5.7.4	Systematic Uncertainty from the Multi-jet Background Estimation . . . . .	57
<b>6</b>	<b>Unfolding</b> . . . . .	<b>61</b>
6.1	Fiducial Measurement . . . . .	62
6.2	Purity and Stability . . . . .	64
<b>7</b>	<b>Systematic Uncertainties on the Cross Section Measurement</b> . . . . .	<b>66</b>
7.1	Propagation of Uncertainties Using the Toy Monte Carlo Method . . . . .	66
7.1.1	Extraction of Correlated Uncertainties . . . . .	67
7.2	Experimental Systematic Uncertainties . . . . .	68
7.2.1	Electron Energy Scale and Resolution Uncertainty . . . . .	68
7.2.2	Di-Electron Trigger Efficiency Uncertainty . . . . .	68
7.2.3	Reconstruction and Identification Efficiency Uncertainty . . . . .	68
7.2.4	Electroweak and $t\bar{t}$ Background Uncertainty . . . . .	68
7.2.5	Multi-jet Background Uncertainty . . . . .	69
7.3	Theoretical Systematic Uncertainties . . . . .	69
7.3.1	PDF Uncertainty . . . . .	69
7.3.2	Generator (Matrix Element) Uncertainty . . . . .	69

---

7.3.3	Parton Shower Uncertainty . . . . .	69
<b>8</b>	<b>Results of the Cross Section Measurement</b>	<b>70</b>
8.1	Comparison with Theoretical Predictions . . . . .	75
<b>9</b>	<b>Combination of Electron and Muon Cross Section Measurements</b>	<b>78</b>
9.1	Combination Procedure . . . . .	78
9.1.1	Linear Averaging . . . . .	78
9.1.2	Iterative Procedure of Minimisation . . . . .	86
9.2	Combination Results . . . . .	86
9.2.1	Combined Cross Section Results Compared to Theoretical Predictions	96
<b>10</b>	<b>Combined ATLAS <math>Z/\gamma^* \rightarrow ll</math> Cross Section vs. <math>m_{ll}</math></b>	<b>100</b>
<b>11</b>	<b>Summary</b>	<b>103</b>
<b>A</b>	<b>Covariance of correlated systematic uncertainty sources</b>	<b>104</b>
<b>B</b>	<b>Combination of Double Differential Cross Sections</b>	<b>110</b>
B.1	Combined Double Differential Cross Section Results Compared to Theoretical Predictions . . . . .	114
<b>C</b>	<b>Phase Space Definitions</b>	<b>117</b>
<b>D</b>	<b>References</b>	<b>120</b>
	<b>Acknowledgements</b>	<b>127</b>

## List of Tables

5.1	The luminosity per data period collected in 2011 by the ATLAS detector at beam energies of 3.5TeV. Period C is not shown as the beam energy for this period was 1.38TeV. Periods shown in <i>italics</i> were not used in this analysis. .	34
5.2	Monte Carlo samples and generators used in this analysis to simulate the $Z \rightarrow ee$ decay process. The quoted cross sections are used to normalise estimates of expected number of events. . . . .	35
5.3	An overview of the period-dependent di-electron triggers used in this analysis.	38
5.4	A cut-flow showing the number of events passing each cut sequentially for data and Monte Carlo. $\epsilon_{rel}$ is the efficiency relative to the previous cut in the sequence and $\epsilon_{abs}$ is the efficiency relative to the total number of events before any analysis cuts are applied. . . . .	42
5.5	A cut-flow showing the number of events passing each cut sequentially for data and Monte Carlo. $\epsilon_{rel}$ is the efficiency relative to the previous cut in the sequence and $\epsilon_{abs}$ is the efficiency relative to the total number of events before any analysis cuts are applied. Here the trigger cut is placed last to compare the efficiencies of offline and online cuts. . . . .	42
5.6	Background processes with their associated cross sections and uncertainties. The quoted cross sections are used to normalise estimates of expected number of events. . . . .	53
5.7	The left edge of the normalisation range in each mass bin, and the factor calculated to normalise the tail of the isolation distribution. . . . .	56
5.8	The left edge of the normalisation region, $L$ , number of events in the tail of the data distribution, $n$ , fractional percentage of signal ( $\frac{s}{n}$ ) and background ( $\frac{s}{n}$ ) events in measurement bin $66 < m_Z[GeV] < 76$ for iteration $i$ of the scan of the normalisation region. The number of events in the tail of the template selection, $t$ , as well as the fractional percentage of signal ( $\frac{s}{t}$ ) and background ( $\frac{s}{t}$ ) events is also shown. . . . .	59
5.9	The left edge of the normalisation region, $L$ , number of events in the tail of the data distribution, $n$ , fractional percentage of signal ( $\frac{s}{n}$ ) and background ( $\frac{s}{n}$ ) events in measurement bin $76 < m_Z[GeV] < 91$ for iteration $i$ of the scan of the normalisation region. The number of events in the tail of the template selection, $t$ , as well as the fractional percentage of signal ( $\frac{s}{t}$ ) and background ( $\frac{s}{t}$ ) events is also shown. . . . .	59

5.10	The left edge of the normalisation region, $L$ , number of events in the tail of the data distribution, $n$ , fractional percentage of signal ( $\frac{s}{n}$ ) and background ( $\frac{b}{n}$ ) events in measurement bin $91 < m_Z[\text{GeV}] < 106$ for iteration $i$ of the scan of the normalisation region. The number of events in the tail of the template selection, $t$ , as well as the fractional percentage of signal ( $\frac{s}{t}$ ) and background ( $\frac{b}{t}$ ) events is also shown. . . . .	60
5.11	The left edge of the normalisation region, $L$ , number of events in the tail of the data distribution, $n$ , fractional percentage of signal ( $\frac{s}{n}$ ) and background ( $\frac{b}{n}$ ) events in measurement bin $106 < m_Z[\text{GeV}] < 116$ for iteration $i$ of the scan of the normalisation region. The number of events in the tail of the template selection, $t$ , as well as the fractional percentage of signal ( $\frac{s}{t}$ ) and background ( $\frac{b}{t}$ ) events is also shown. . . . .	60
6.1	Complete list of experimental measurements considered in the $Z \rightarrow ee$ and $Z \rightarrow \mu\mu$ channels. . . . .	63
8.1	Fiducial $Z \rightarrow ee$ cross section as a function of di-electron invariant mass. Statistical, systematic, and luminosity uncertainties are shown as percentages of cross section. . . . .	71
8.2	Systematic uncertainties as a percentage of the $Z \rightarrow ee$ cross section as a function of di-electron invariant mass. . . . .	74
8.3	$E_Z$ factors and associated uncertainties in bins of invariant mass. . . . .	75
8.4	Extrapolated differential cross section for the $Z \rightarrow ee$ process $d\sigma/dm$ measured for and $P_{t,\ell} > 20$ GeV. $\delta_{\text{stat}}$ , $\delta_{\text{unc}}$ , $\delta_{\text{corr}}$ and $\delta_{\text{tot}}$ represent statistical, uncorrelated systematic, correlated systematic and total uncertainties. . . . .	76
9.1	Summary of the correlations for the uncertainties. Each number represents a nuisance parameter. Cells with a shared nuisance parameter are treated as correlated, whereas cells containing $u$ are treated as uncorrelated. $uN$ represents an uncertainty which is uncorrelated bin-to-bin, but correlated across cells with the same $N$ . Uncertainties in red consist of multiple nuisance parameters. . .	79
9.2	Combined differential cross section for the $Z \rightarrow \ell\ell$ process $d\sigma/dm$ measured for $66 < m_Z < 116$ GeV and $P_{t,\ell} > 20$ GeV. $\delta_{\text{stat}}$ , $\delta_{\text{unc}}$ , $\delta_{\text{corr}}$ and $\delta_{\text{tot}}$ represent statistical, uncorrelated systematic, correlated systematic and total uncertainties. . . . .	88
9.3	Combined differential cross section for the $Z \rightarrow \ell\ell$ process $d\sigma/d y $ measured for $46 < M_{\ell\ell} < 66$ GeV and $P_{t,\ell} > 20$ GeV. $\delta_{\text{stat}}$ , $\delta_{\text{unc}}$ , $\delta_{\text{corr}}$ and $\delta_{\text{tot}}$ represent statistical, uncorrelated systematic, correlated systematic and total uncertainties. . . . .	93
9.4	Combined differential cross section for the $Z \rightarrow \ell\ell$ process $d\sigma/d y $ measured for $66 < M_{\ell\ell} < 116$ GeV and $P_{t,\ell} > 20$ GeV. $\delta_{\text{stat}}$ , $\delta_{\text{unc}}$ , $\delta_{\text{corr}}$ and $\delta_{\text{tot}}$ represent statistical, uncorrelated systematic, correlated systematic and total uncertainties. . . . .	93

9.5	Combined differential cross section for the $Z \rightarrow \ell\ell$ process $d\sigma/d y $ measured for $116 < M_{\ell\ell} < 150$ GeV and $P_{t,\ell} > 20$ GeV. $\delta_{\text{stat}}$ , $\delta_{\text{unc}}$ , $\delta_{\text{corr}}$ and $\delta_{\text{tot}}$ represent statistical, uncorrelated systematic, correlated systematic and total uncertainties.	94
9.6	Combined differential cross section for the $W^- \rightarrow \ell^- \bar{\nu}$ $d\sigma/d \eta $ measured for $p_{t,\ell} > 20$ GeV, $P_{t,\nu} > 25$ GeV and $M_t > 40$ GeV. $\delta_{\text{stat}}$ , $\delta_{\text{unc}}$ , $\delta_{\text{corr}}$ and $\delta_{\text{tot}}$ represent statistical, uncorrelated systematic, correlated systematic and total uncertainties.	94
9.7	Combined differential cross section for the $W^+ \rightarrow \ell^+ \nu$ $d\sigma/d \eta $ measured for $p_{t,\ell} > 20$ GeV, $P_{t,\nu} > 25$ GeV and $M_t > 40$ GeV. $\delta_{\text{stat}}$ , $\delta_{\text{unc}}$ , $\delta_{\text{corr}}$ and $\delta_{\text{tot}}$ represent statistical, uncorrelated systematic, correlated systematic and total uncertainties.	95
10.1	$A_Z$ factors and associated uncertainties in bins of invariant mass.	101
C.1	Complete list of experimental measurements considered in the $W \rightarrow e\nu$ and $W \rightarrow \mu\nu$ channels.	118
C.2	Complete list of combined measurements considered for all the $W \rightarrow \ell\nu$ and $Z \rightarrow \ell\ell$ channels.	119

## List of Figures

2.1	Neutral (charged) current deep inelastic scattering processes. $X$ represents a hadronic final state. . . . .	3
2.2	The proton structure function $F_2(x, Q^2)$ measured in scattering of electrons and positrons on protons (H1+ZEUS), and electrons (SLAC) and muons (BCDMS, E665, NMC) on a fixed target. Scaling can be seen in the independence of $F_2(x, Q^2)$ on $Q^2$ , however at extreme values of $x$ , scaling violations are observed.	5
2.3	Experimental evidence for the Callan-Gross relation. Plot from [8] using data from [9]. . . . .	6
2.4	The coupling $\alpha_s$ of the strong interaction as a function of the energy scale [12].	8
2.5	Parton distributions from HERAPDF1.0 at $Q^2 = 10\text{GeV}^2$ (left), and $Q^2 = 10000\text{GeV}^2$ (right). The solid line shows the central value with experimental, model, and parametrisation uncertainties shown as coloured bands. The $Q^2$ evolution of the PDF is clear in the difference between the left and right plots.	9
2.6	The Drell-Yan process: quark-antiquark annihilation from two incoming hadrons forms an intermediate vector boson which decays into a dilepton final state. .	10
2.7	NC Drell-Yan cross section as a function of dilepton invariant mass integrated over boson rapidity. The $Z$ resonance (dashed red line) dominates the cross section distribution. . . . .	12
2.8	The phase space coverage in $x, Q^2$ for DIS experiments at HERA and other fixed target experiments, as well as in $M, y$ for Drell-Yan processes at the Tevatron and LHC at $\sqrt{s} = 7$ TeV. . . . .	13
2.9	Average over measurements of the hadronic $Z$ cross sections by the four experiments, as a function of centre-of-mass energy. The solid line is from model-independent fits to the data while the dashed line includes corrections for QED effects [18]. . . . .	14
2.10	The dielectron invariant mass as measured by the ATLAS experiment using data collected in 2010 with an integrated luminosity of $36\text{ pb}^{-1}$ . The QCD background shape is taken from a control sample and normalised to the result of the QCD background fit. The distribution is from central electrons, i.e. those with absolute pseudorapidity $ \eta  < 2.47$ . . . . .	15
2.11	Differential $d\sigma/d y_Z $ cross section measurement for $Z \rightarrow \ell\ell$ compared to NNLO theory predictions from different PDF sets using data collected in 2010 with an integrated luminosity of $36\text{ pb}^{-1}$ . This plot exhibits the discriminating power of measured Drell-Yan data on PDFs. . . . .	16
2.12	The Drell-Yan invariant mass spectrum as measured by the CMS Collaboration using data taken from $pp$ collisions at the LHC in 2011 . . . . .	17

3.1	The CERN accelerator complex. . . . .	19
4.1	A schematic cut-away drawing of the ATLAS detector showing its different sub-components. [39] . . . . .	22
4.2	Image of the ATLAS inner detector [41]. . . . .	24
4.3	The ATLAS Calorimeter system [44]. The location of each calorimeter in relation to the beam pipe can be seen. The EMCAL lies closest to the beam pipe as EM showers are typically shorter in length than hadronic showers. . . . .	27
4.4	The layout of an EMB module in the ATLAS EMCAL. The accordion structure, geometry, and layout of the three sampling layers can be seen. . . . .	28
4.5	Cut-away view of the ATLAS muon system [47] . . . . .	30
4.6	The three levels of the ATLAS trigger system. The event rate at each level is also shown, illustrating the impact of each level's selection on the number of stored events. . . . .	31
5.1	Invariant mass distribution in data and MC after the full event selection. . . . .	43
5.2	Electron energy scale calibration factors as a function of $\eta$ . . . . .	45
5.3	$Z \rightarrow ee \eta$ distributions and ratio for data (black points) and MC (black histogram) for the standard calibration (left) and after applying extra calibration corrections in finer bins (right). . . . .	47
5.4	Left: Scale corrections (black points) in $\eta$ bins of the scale factor obtained by comparing the $Z \rightarrow ee$ peak position as reconstructed in data and MC. The dashed lines show the binning of the official energy scale calibration for comparison. Right: Validation of calibration procedure by computing extra scale corrections (black points) on top of the official energy scale calibration. . . . .	48
5.5	Average interactions per bunch crossing before (left) and after (right) pileup reweighting. . . . .	49
5.6	$Z$ boson $p_T$ before (left) and after (right) $p_T$ reweighting. . . . .	50
5.7	Weights applied to the simulation to correct the $z$ position of the reconstructed primary vertex. . . . .	51
5.8	$z$ position of primary vertex before (left) and after (right) vertex $z$ reweighting. . . . .	51
5.9	The line shape is shown before reweighting (left) and after reweighting (right). . . . .	52
5.10	$E_{T\text{Cone30}}/E_T$ in data and signal MC, illustrating the 0.4 GeV shift in the MC distribution to match the data. . . . .	55

5.11	Plots showing the $E_T\text{Cone30}/E_T$ distribution for data, MC, and background samples in each measurement mass bin. Top left: $66 < m_Z < 76$ GeV, top right: $76 < m_Z < 91$ GeV, bottom left: $91 < m_Z < 106$ GeV, bottom right: $106 < m_Z < 116$ GeV. The distribution for the multi-jet template selection is shown after normalisation. The ratio of data to MC with and without electroweak, $t\bar{t}$ , and multi-jet contributions is shown. The range of the normalisation is indicated by the dashed red lines. . . . .	56
5.12	Plots showing the number of multi-jet events for each iteration of the scan of the isolation variable normalisation region. The mean is shown as a solid line and the minimum and maximum are indicated by dashed lines. Top left: $66 < m_Z < 76$ GeV, top right: $76 < m_Z < 91$ GeV, bottom left: $91 < m_Z < 106$ GeV, bottom right: $106 < m_Z < 116$ GeV. . . . .	58
6.1	Purity (left) and stability (right) measured in bins of di-electron invariant mass.	65
6.2	Deviation in percent with respect to bin-by-bin unfolding of the Bayesian-unfolded distribution for ten iterations (left) and the statistical uncertainty for different unfolding options (right). . . . .	65
8.1	Measured $Z \rightarrow ee$ differential cross section as a function of di-electron invariant mass. . . . .	72
8.2	Systematic uncertainties as a percentage of the differential $Z \rightarrow ee$ cross section measurement. . . . .	73
8.3	$E_Z$ factors in bins of invariant mass used to extrapolate the experimental measurement to a different phase space for comparison with theoretical predictions.	76
8.4	Extrapolated fiducial $Z \rightarrow ee$ cross section as a function of di-electron invariant mass compared to NNLO QCD predictions with NLO EW corrections based on various NNLO PDFs. . . . .	77
9.1	Bin-to-bin correlations across all measurements for the systematic uncertainties from the forward electron ID scale factor (top), and the electron ID scale factor (bottom). . . . .	80
9.2	Bin-to-bin correlations across all measurements for the systematic uncertainties from the electron isolation scale factor (top), and the electron reconstruction scale factor (bottom). . . . .	81
9.3	Bin-to-bin correlations across all measurements for the systematic uncertainties from the single electron trigger scale factor (top), and the di-electron trigger scale factor (bottom). . . . .	82
9.4	Bin-to-bin correlations across all measurements for the systematic uncertainties from the statistical components of the muon isolation scale factor (top), and the muon reconstruction scale factor (bottom). . . . .	83

9.5	Bin-to-bin correlations across all measurements for the systematic uncertainties from the statistical components of the muon trigger scale factor. . . . .	84
9.6	Differential $d\sigma/dm_Z$ cross section in the region $66 < m_{\ell\ell} < 116\text{GeV}$ measured using data collected in 2011. Also shown are the individual channel measurements in each bin with uncorrelated uncertainties and the pull from each point. . . . .	88
9.7	Combined $d\sigma/d y_Z $ cross section in the region $66 < m_{\ell\ell} < 116\text{GeV}$ measured using data collected in 2011 (top) and 2010 (bottom). Also shown for the 2011 measurement are the individual channel measurements in each bin with uncorrelated uncertainties and the pull from each point. . . . .	89
9.8	Combined $d\sigma/d y_Z $ cross section in the regions $46 < m_{\ell\ell} < 66\text{GeV}$ (top) and $116 < m_{\ell\ell} < 150\text{GeV}$ (bottom) measured using data collected in 2011. Also shown are the individual channel measurements in each bin with uncorrelated uncertainties and the pull from each point. . . . .	90
9.9	Combined differential $d\sigma/d \eta_\ell  W^-$ cross section measured in 2011 (top) and 2010 (bottom). Also shown for the 2011 measurement are the individual channel measurements in each bin with uncorrelated uncertainties and the pull from each point. . . . .	91
9.10	Combined differential $d\sigma/d \eta_\ell  W^+$ cross section measured in 2011 (top) and 2010 (bottom). Also shown for the 2011 measurement are the individual channel measurements in each bin with uncorrelated uncertainties and the pull from each point. . . . .	92
9.11	Combined $Z \rightarrow \ell\ell$ cross section as a function of di-electron invariant mass in the region $66 < m_Z < 116\text{ GeV}$ compared to NNLO QCD predictions with NLO EW corrections based on various NNLO PDFs. . . . .	97
9.12	Combined $Z \rightarrow \ell\ell$ cross section as a function of $Z$ boson rapidity in the region $66 < m_Z < 116\text{ GeV}$ compared to NNLO QCD predictions with NLO EW corrections based on various NNLO PDFs. . . . .	97
9.13	Combined $Z \rightarrow \ell\ell$ cross section as a function of $Z$ boson rapidity in the region $46 < m_Z < 66\text{ GeV}$ compared to NNLO QCD predictions with NLO EW corrections based on various NNLO PDFs. . . . .	98
9.14	Combined $Z \rightarrow \ell\ell$ cross section as a function of $Z$ boson rapidity in the region $116 < m_Z < 150\text{ GeV}$ compared to NNLO QCD predictions with NLO EW corrections based on various NNLO PDFs. . . . .	98
9.15	Combined $W^-$ (left) and $W^+$ (right) cross sections as a function of lepton pseudo-rapidity compared to NNLO QCD predictions with NLO EW corrections based on various NNLO PDFs. . . . .	99

10.1	Differential cross section as a function of, $m_{\ell\ell}$ for the neutral current process, $Z/\gamma^* \rightarrow \ell\ell$ . The line shape measurement is displayed as red triangles. . . . .	100
10.2	$A_Z$ factors in bins of invariant mass used to extrapolate the experimental measurement to a different phase space for comparison with theoretical predictions. . . . .	101
A.1	Bin-to-bin covariance across all measurements for the systematic uncertainties from the forward electron ID scale factor (top), and the electron ID scale factor (bottom). . . . .	105
A.2	Bin-to-bin covariance across all measurements for the systematic uncertainties from the electron isolation scale factor (top), and the electron reconstruction scale factor (bottom). . . . .	106
A.3	Bin-to-bin covariance across all measurements for the systematic uncertainties from the single electron trigger scale factor (top), and the statistical component of the di-electron trigger scale factor (bottom). . . . .	107
A.4	Bin-to-bin covariance across all measurements for the systematic uncertainties from the statistical components of the muon isolation scale factor (top), and the muon reconstruction scale factor (bottom). . . . .	108
A.5	Bin-to-bin covariance across all measurements for the systematic uncertainties from the statistical components of the muon trigger scale factor. . . . .	109
B.1	Combination double-differential $d\sigma/d \eta_l  dp_{T,\ell}$ cross section measurements for $W^+$ (left) and $W^-$ (right). Also shown are the measurements in each bin with uncorrelated uncertainties. . . . .	111
B.2	Combination double-differential $d\sigma/d \eta_l  dp_{T,\ell}$ cross section measurements for $W^+$ (left) and $W^-$ (right). . . . .	112
B.3	Combined differential $d\sigma/d y_Z $ cross section measurements when combined with $d\sigma/d \eta_l  dp_{T,\ell}$ (left) and their comparison to the measurements combined with $d\sigma/d \eta_\ell $ (right). . . . .	113
B.4	Combination double-differential $d\sigma/d \eta_l  dp_{T,\ell}$ cross section measurements for $W^+$ (left) and $W^-$ (right). Also shown are the measurements in each bin with uncorrelated uncertainties. . . . .	115
B.5	Combination double-differential $d\sigma/d \eta_l  dp_{T,\ell}$ cross section measurements for $W^+$ (left) and $W^-$ (right). . . . .	116

# 1 Overview

This thesis presents a measurement of the Neutral Current Drell-Yan cross section from  $Z \rightarrow ee$  decays using data collected in 2011 with the ATLAS detector at the LHC. The layout of the thesis is as follows:

**Chapter 2** gives a brief theoretical introduction to the parton model, QCD theory, parton distribution functions and their determination, and  $Z$  boson production in  $pp$  collisions. An introduction is given to some of the tools used to produce theoretical calculations used to evaluate and compare the measured  $Z \rightarrow ee$  cross section. The motivation for the analysis presented in the thesis is outlined in this chapter.

**Chapters 3 and 4** describe the LHC and ATLAS detector respectively. Particular emphasis is given to the sub-components used to measure and identify electrons.

**Chapter 5** describes the measurement of the cross section, starting with an overview of the data collected in 2011 with the ATLAS detector and the Monte Carlo samples used to simulate the signal process. The procedure for the cross section calculation is outlined, with a step-by-step description of the process to reconstruct and select  $Z \rightarrow ee$  events in ATLAS. Efficiency corrections as well as various kinematic corrections applied to the simulation are explained and validated. The process of estimating the background processes is presented in this chapter, including a data-driven method for estimating the QCD background.

**Chapter 6** describes the unfolding of the measured distributions to obtain the cross section, as well as introducing the phase space of the fiducial measurement, while validating the binning of the measurement, and motivating the choice of unfolding technique.

**Chapter 7** explains the treatment of the systematic uncertainties on the measurement, describing the process of propagating those uncertainties to the final result, as well as outlining the sources of uncertainty themselves.

**Chapter 8** presents the results of the cross section measurement, and analyses the magnitudes of the systematic uncertainties on the final result. The data are compared to theoretical predictions from different PDF sets.

**Chapter 9** describes the process of combining electron and muon  $W^\pm$  and  $Z/\gamma^*$  cross section measurements through linear averaging. An overview of the treatment of systematic uncertainties and their correlations during the combination is given, before the results of the combination are presented. The combined cross section measurements are compared to theoretical predictions and past measurements.

**Chapter 10** shows the total  $Z/\gamma^* \rightarrow \ell\ell$  cross section as a function of invariant mass in the range  $0 < m_Z < 1500$  GeV, combining data from low and high mass Drell-Yan measurements in ATLAS.

## 2 Theoretical Introduction

In a proton-proton collision at energies where the squared momentum transfer in the collision exceeds the rest mass of the proton, the interacting particles can be described in terms of the parton model [1]. The parton model was developed to explain observed phenomena in Deep Inelastic Scattering (DIS) of electrons on nucleons [2]. The data suggested a substructure to the targets (protons and neutrons) in the collisions. These observations and implications are described in Sec. 2.1.2. The constituents of the individual nucleons came to be known as partons, which were eventually recognised as quarks and gluons. When hadrons collide, a number of processes can take place, governed by the constituents of the interacting hadrons. One such process is the Drell-Yan process [3] which is discussed in Sec. 2.4.

### 2.1 Introduction to the Parton Model

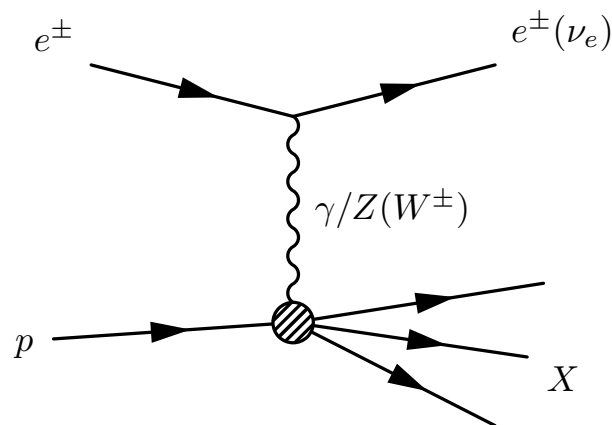


**Figure 2.1:** Neutral (charged) current deep inelastic scattering processes.  $X$  represents a hadronic final state.

#### 2.1.1 Structure Functions and Scaling

Deep Inelastic Scattering of leptons on nucleons can be represented diagrammatically as in Fig. 2.1. The neutral current (NC) process  $ep \rightarrow eX$  and the charged current (CC) process  $e(\nu)p \rightarrow \nu(e)X$  are shown, where  $X$  represents a hadronic final state. The cross section can be written very generally as  $d\sigma \approx L_{\mu\nu}W^{\mu\nu}$ , where  $L_{\mu\nu}$  is the leptonic tensor and  $W^{\mu\nu}$  is the hadronic tensor. In this representation, the propagator probes the structure of the proton, and as the lepton sector is unchanged in the interaction, the hadronic tensor is a parametrisation of the shaded vertex in Fig. 2.1 and can be used for a mathematical interpretation of the current at that vertex as a function of the momentum transfer from the incoming lepton to the target,

$q$ , and the momentum of the incoming hadron,  $p$  [4].

$$W^{\mu\nu} = W_1(-g^{\mu\nu} + \frac{q^\mu q^\nu}{q^2}) + W_2(P^\mu - \frac{P \cdot q}{q^2} q^\mu)(P^\nu - \frac{P \cdot q}{q^2} q^\nu) \quad (2.1)$$

where  $W_{1,2}$  are Lorentz scalar structure functions of the proton, which are functions of the variables  $Q^2$ , which is the squared momentum transfer carried by the the propagator, and

$$x = \frac{Q^2}{2P \cdot q} \quad (2.2)$$

often called the Bjorken scaling variable, or Bjorken  $x$ . This variable is dimensionless which implies an independence of the structure functions on  $Q^2$ . This behaviour is called scaling and was experimentally confirmed in DIS experiments at SLAC [5]. The structure functions  $W_{1,2}(x, Q^2)$  are often represented in terms of dimensionless equivalents:  $F_{1,2}(x, Q^2)$ , where  $F_1 = W_1$  and  $F_2 = P \cdot q W_2$ . There have been a number of experiments studying DIS processes and in particular the proton structure function  $F_2$ . The results of many measurements of  $F_2$  as a function of  $Q^2$  from different experiments is shown in Fig. 2.2 [6]. The plot shows results at different values of fixed  $x$ . Scaling can be seen in the relative independence of  $F_2(x, Q^2)$  on  $Q^2$ , however at extreme values of  $x$ , scaling violations are observed. These are in fact predicted and explained by the theory of strong interactions between partons, quantum chromo-dynamics.

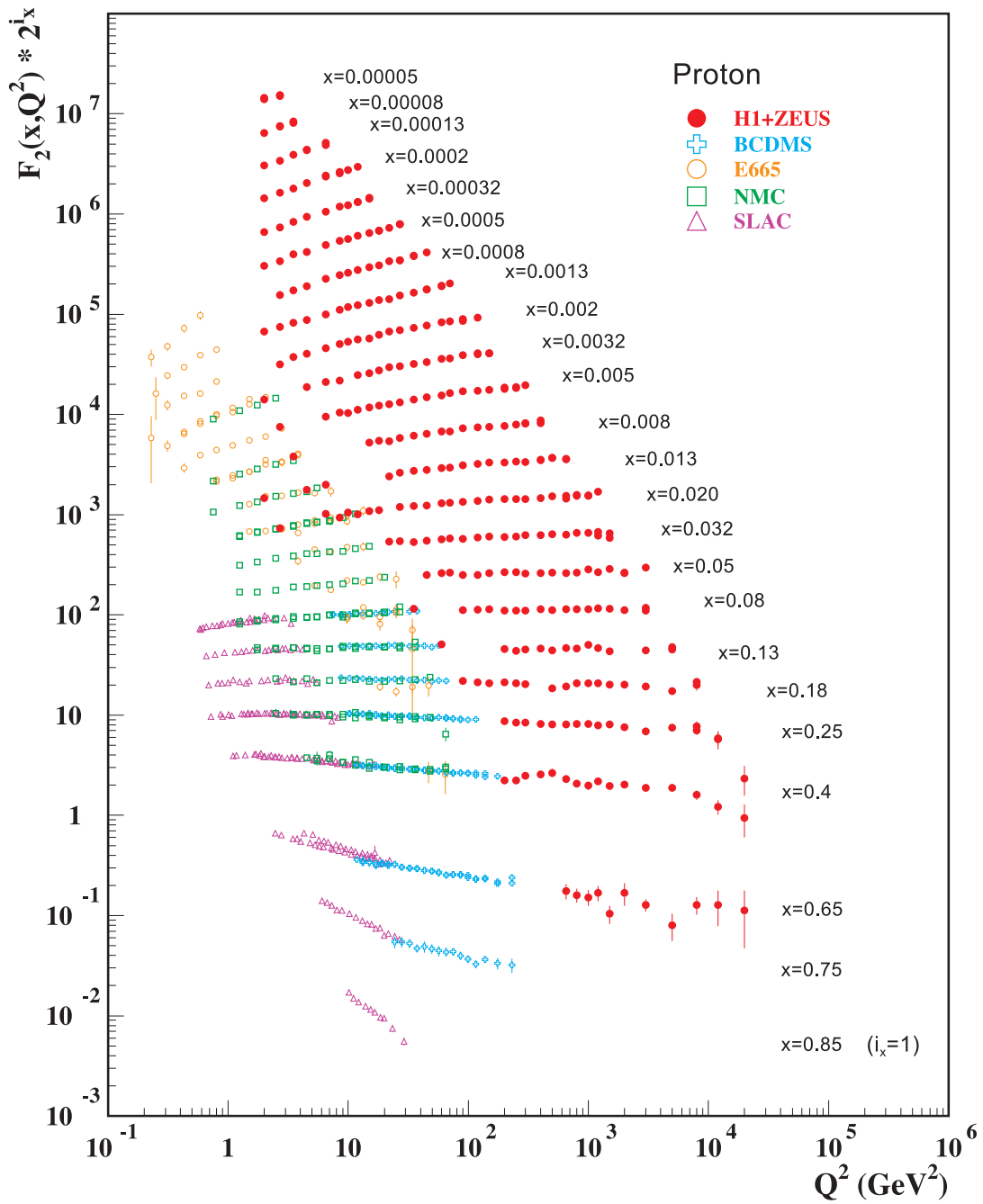


**Figure 2.2:** The proton structure function  $F_2(x, Q^2)$  measured in scattering of electrons and positrons on protons (H1+ZEUS), and electrons (SLAC) and muons (BCDMS, E665, NMC) on a fixed target. Scaling can be seen in the independence of  $F_2(x, Q^2)$  on  $Q^2$ , however at extreme values of  $x$ , scaling violations are observed.

### 2.1.2 The Parton Model

Bjorken scaling implies that the exchange particle is scattering off a point-like constituent of the proton. Almost concurrently with the observation of scaling at SLAC, Feynman was developing the idea that there were such constituents of hadrons. These theoretical developments, along with the experimental data led to the formation of the Parton Model, so called after Feynman's name for the hadron constituents. As mentioned in Sec. 2.1.1, results in studies into the behaviour of structure functions provided evidence for scaling. Further evidence for the parton model comes from other studies into the relationship between structure functions. In 1969 Callan and Gross [7] proposed the relation:

$$F_2(x) = 2xF_1(x) \quad (2.3)$$

which holds for spin- $\frac{1}{2}$  partons. This behaviour has also been observed and is shown in Fig. 2.3. The scaling behaviour of the proton structure function is evidence of point like constituents in the proton, and the Callan-Gross relation indicates that those constituents are spin- $\frac{1}{2}$  quarks. This is the foundation of the parton model.

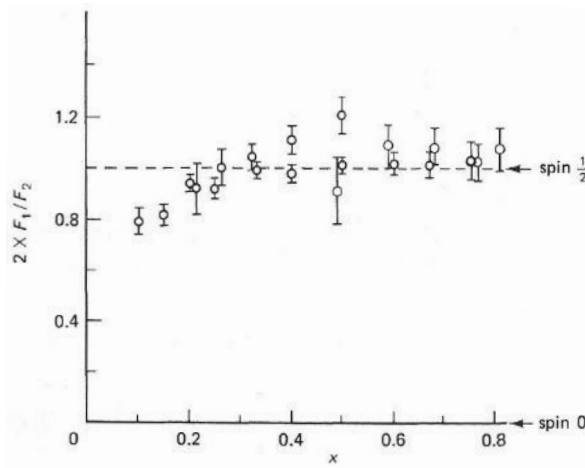


**Figure 2.3:** Experimental evidence for the Callan-Gross relation. Plot from [8] using data from [9].

## 2.2 Quantum Chromo-Dynamics

Strong interactions in the Standard Model (SM) are described by the theory of Quantum Chromo-Dynamics (QCD) [10]. The theory is so named because of an inherent property of the force it describes: colour charge, which is a quantum number carried by partons. The force between particles which exhibit colour charge is mediated by gluons, which are partons themselves. The

consequential self-interaction of the gluons defines QCD as a non-Abelian theory, and is theorised to explain why quarks are not observed in isolation. This gluon-gluon interaction results in an effective amplification of the force between quarks, and so the strength of the force does not decrease as the distance between them increases. As a consequence, the energy required to separate quarks on an observable scale is above the quark-antiquark pair production energy. This is called confinement, and can be phrased as the requirement that an observed state must have zero colour charge. Similarly it explains why fractional charge, which is a property of quarks, is not observed.

Another property of QCD is asymptotic freedom. This describes the phenomenon that with increasing energy and momentum, the running coupling constant for the strong interaction,  $\alpha_s$ , decreases. At energy scales large enough to probe inside the proton, the strength of the coupling becomes vanishingly small, and the constituent partons are effectively 'free'. The strength of the coupling as a function of the energy scale of the interaction,  $Q^2$ , can be seen in Fig. 2.4

In the high- $Q^2$  regime, perturbation theory can be applied to study QCD. However, due to the same behaviour of  $\alpha_s$  which causes confinement at low- $Q^2$ , perturbative QCD can't be used at all scales. The coupling constant is too large and this leads to significant corrections even at low orders.

Any cross section calculation at hadron colliders relies on factorisation theorem, which states that the cross section for a process is the convolution of the parton-level cross section calculable from perturbative theoretical models, and Parton Distribution Functions (PDFs), the shapes of which can be determined by fitting experimental observables to data.

This can be expressed mathematically as:

$$\sigma_{p \rightarrow X} = \sum_{i,j} \int dx_1 dx_2 f_i^p(x_1, \mu_F) f_j^p(x_2, \mu_F) \times \hat{\sigma}_{ij \rightarrow X}(x_1, x_2, s, \alpha_s(\mu_R)) \quad (2.4)$$

where  $f_{i,j}^{p,p}$  are the PDF for the protons  $i$  and  $j$ , and  $\hat{\sigma}_{ij \rightarrow X}$  is the parton cross section for incoming partons with momenta  $p_1 = x_1 P_1$  and  $p_2 = x_2 P_2$  [11].

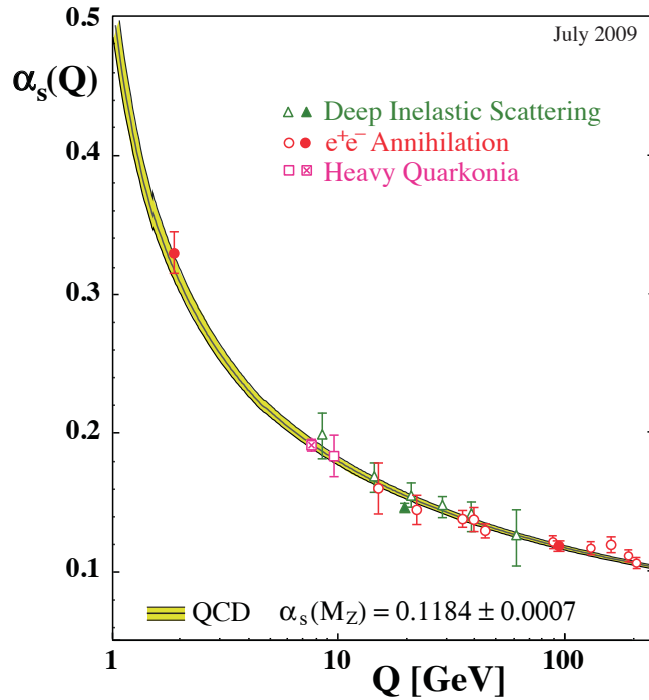


**Figure 2.4:** The coupling  $\alpha_s$  of the strong interaction as a function of the energy scale [12].

## 2.3 Parton Distribution Functions

The quarks which determine the quantum numbers of the hadron are called valence quarks. A proton has three valence quarks: two up quarks and a down quark, often designated *uud*. Interactions between the partons result in production of additional partons, both in the form of gluons and pair-produced quark-antiquark pairs. The proton can therefore be considered to consist not just of the valence quarks, but also what is called a 'sea' of partons. As explained in Sec. 2.2, the distributions of the constituent partons within a hadron can't be calculated perturbatively, and PDFs must be extracted from experiments.

### 2.3.1 PDF Determination

The probability of finding a parton  $i$  in a proton is given by the parton density function  $f_i(x, Q^2)$  where  $x$  is the fraction of the proton momentum carried by the parton, and  $Q^2$  is the squared momentum transfer, or the energy scale, of the hard interaction [13]. PDFs can be considered as a set of individual parton density functions. The distribution of these parton density functions provide a window into the structure of the proton. PDFs are typically developed by parameterisation, whereby the shape of the PDF is studied as a function of  $x$  at low- $Q^2$  and then evolved in  $Q^2$  using the DGLAP<sup>1</sup> formalism [14–16]. These distributions are then fit to a

<sup>1</sup>Dokshitzer-Gribov-Lipatov-Altarelli-Parisi

large number of cross section data points from various experiments.

An example of some distributions determined from data from DIS experiments at HERA, DESY can be seen in Fig. 2.5. The figure shows the fractional distribution  $xf$  of quarks and gluons as a function of the longitudinal momentum fraction  $x$  of the parton for different values of  $Q^2$ . At low- $x$ , the parton can be considered to be composed of mostly sea quarks ( $xS$ ) and gluons  $xg$ . These distributions are scaled down by a factor of 20 in the plot. At higher  $x$  values (around 0.2), the valence quarks dominate the distributions with the contribution from up quarks ( $xu_v$ ) approximately double the contribution from down quarks ( $xd_v$ ) as expected.

The evolution of the PDF can be seen by comparing the shape of the two plots at  $Q^2 = 10\text{GeV}^2$ , and  $Q^2 = 10000\text{GeV}^2$ .

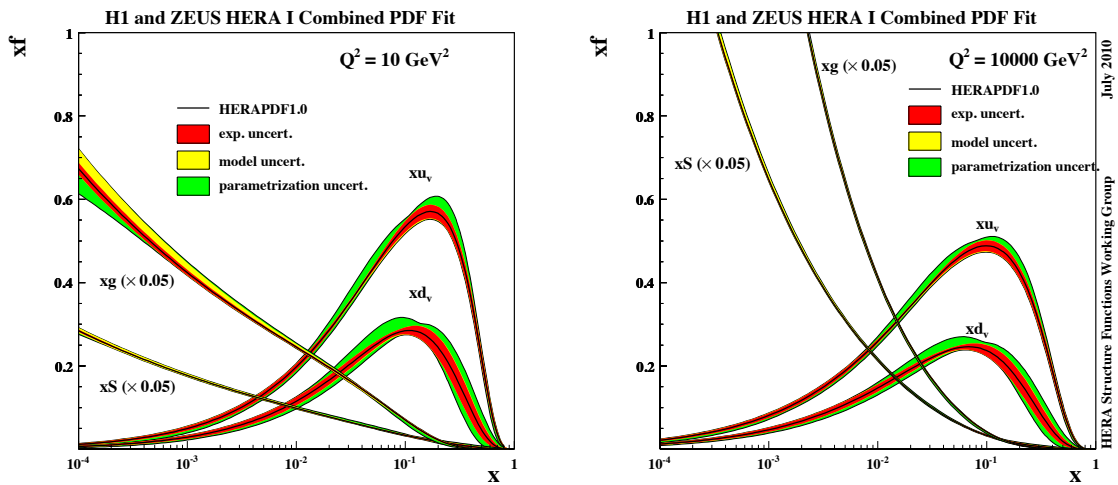


**Figure 2.5:** Parton distributions from HERAPDF1.0 at  $Q^2 = 10\text{ GeV}^2$  (left), and  $Q^2 = 10000\text{ GeV}^2$  (right). The solid line shows the central value with experimental, model, and parametrisation uncertainties shown as coloured bands. The  $Q^2$  evolution of the PDF is clear in the difference between the left and right plots.

## 2.4 The Drell-Yan Process

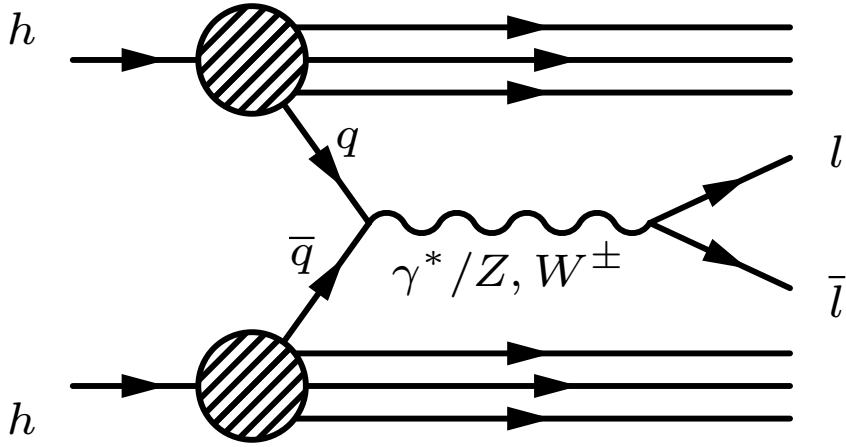


**Figure 2.6:** The Drell-Yan process: quark-antiquark annihilation from two incoming hadrons forms an intermediate vector boson which decays into a dilepton final state.

A quark from one hadron can annihilate with an antiquark from another hadron and produce a vector boson. The boson then decays into a dilepton final state. This  $q\bar{q} \rightarrow \ell^+\ell^-X$  reaction defines the Drell-Yan process. The Feynman diagram for the Drell-Yan process is shown in Fig. 2.6. The squared momentum transfer in the interaction is given by:

$$Q^2 = (x_1 p_1 + x_2 p_2)^2 \quad (2.5)$$

where  $p_{1,2}$  is the momentum of each of the incoming protons 1 and 2 respectively, and  $x_{1,2}$  is the fraction of the proton momentum carried by the partons. For a hadron-hadron collision, the total energy squared is  $s = (p_1 + p_2)^2$ , giving from Eq. 2.5:  $Q^2 \approx x_1 x_2 s$ .

The cross section for dilepton production from quark-antiquark annihilation at leading order can be written as:

$$\sigma = \frac{4\pi\alpha^2}{3Q^2} \frac{1}{N} e_q^2 \quad (2.6)$$

where  $e_q$  is the quark charge. The factor  $\frac{1}{N} = \frac{1}{3}$  arises from the fact that only in the case where the colour charge of the quark matches the colour charge of the antiquark can annihilation into a colour singlet final state take place. Multiplying this expression by the parton density functions for the two partons gives (summing over quark flavours):

$$\frac{d^2\sigma}{dx_1 dx_2} = \frac{4\pi\alpha^2}{9Q^2} \sum_q e_q^2 [x_1 x_2 (q(x_1, Q^2) \bar{q}(x_2, Q^2) + q(x_2, Q^2) \bar{q}(x_1, Q^2))] \quad (2.7)$$

This can be written more generally as the leading order (LO) double differential Drell-Yan cross section [17]:

$$\frac{d^2\sigma}{dMdy} = \frac{4\pi\alpha^2(M)}{9} \cdot 2M \cdot P(M) \cdot \Phi(x_1, x_2, M^2) \quad (2.8)$$

where  $P(M)$  is the propagator term,  $\Phi$  is the parton distribution term,  $M$  is the dilepton invariant mass (equivalent to  $Q$  at LO), and  $y$  is the boson rapidity:

$$y = \frac{1}{2} \ln \frac{E + p_z}{E - p_z} = \frac{1}{2} \ln \frac{x_1}{x_2} \quad (2.9)$$

The cross section for the NC process is the sum of contributions from photon and  $Z$  exchange, as well as a contribution from interference between them. The propagator and parton distribution terms for photon exchange are given by:

$$P_\gamma(M) = \frac{1}{M^4}, \quad \Phi_\gamma = \sum_q e_q^2 F_{q\bar{q}} \quad (2.10)$$

$$F_{q\bar{q}} = x_1 x_2 [q(x_1, M^2) \bar{q}(x_2, M^2) + q(x_2, M^2) \bar{q}(x_1, M^2)] \quad (2.11)$$

Introducing vector and axial couplings:

$$v_f = I_3^f - e_f \sin^2 \Theta, \quad a_f = I_3^f \quad [f = e, q] \quad (2.12)$$

allows the definition of  $P$  and  $\Phi$  for  $Z$  exchange:

$$P_Z = \frac{\kappa_Z^2}{(M^2 - M_Z^2)^2 + (\Gamma_Z M_Z)^2}, \quad \Phi_Z = \sum_q (v_q^2 + a_q^2) F_{q\bar{q}} \quad (2.13)$$

$$\kappa_Z = \frac{1}{4 \sin^2 \theta \cos^2 \theta}, \quad \cos \theta = \frac{M_W}{M_Z} \quad (2.14)$$

Finally the terms for the  $\gamma Z$  interference contribution are:

$$P_{\gamma Z} = \frac{\kappa_Z v_e (M^2 - M_Z^2)^2}{M^2 [(M^2 - M_Z^2)^2 + (\Gamma_Z M_Z)^2]}, \quad \Phi_{\gamma Z} = \sum_q 2e_q v_q F_{q\bar{q}} \quad (2.15)$$

The distribution of the different contributions to the differential cross section as a function of mass (integrated over  $y$ ) is shown in Fig. 2.7. At low- $M$ , the photon contribution dominates, but its influence decreases with increasing mass as expected from the  $M^{-4}$  term in Eq. 2.10. The  $Z$  resonance at  $M \approx 90$  GeV dominates the distribution. The  $\gamma Z$  interference contribution changes sign at  $M = M_Z$  but is shown in absolute.

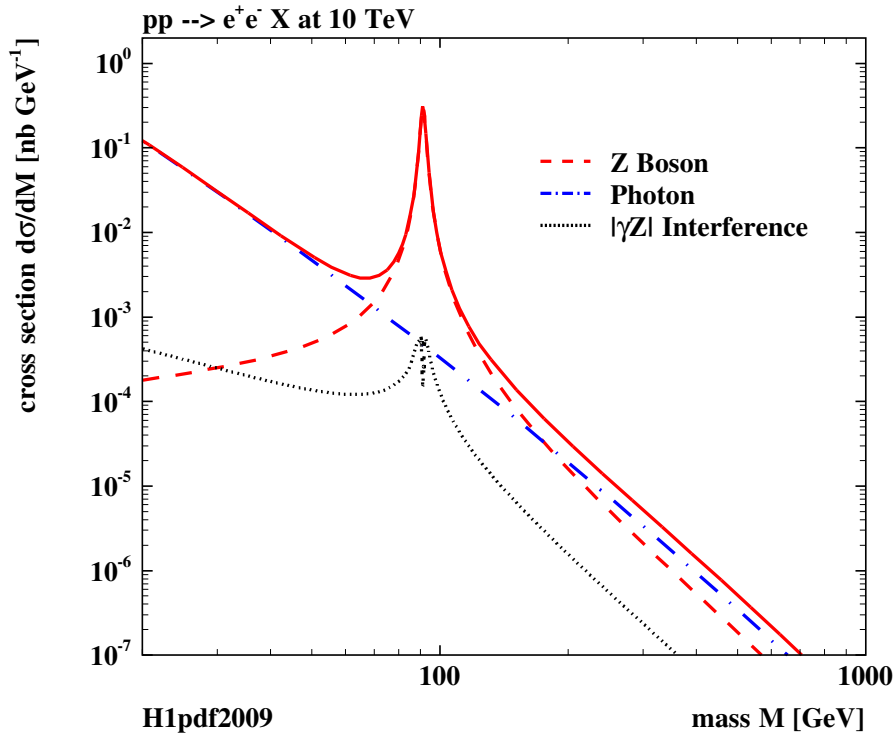


**Figure 2.7:** NC Drell-Yan cross section as a function of dilepton invariant mass integrated over boson rapidity. The  $Z$  resonance (dashed red line) dominates the cross section distribution.

The Drell-Yan process can be used as a way to probe QCD and determine PDFs. The rapidity distribution of the boson or dilepton pair is related to the longitudinal parton momentum fraction,  $x$  and so this can be used to examine the PDFs directly as explained in Sec. 2.3. In addition, the invariant mass distribution of the dilepton pair in the Neutral Current (NC) process can be used to measure the scale  $Q^2$  of the interaction at leading order as shown in Eq. 2.5. A plot showing the phase space coverage of a number of experiments and processes can be seen in Fig. 2.8.

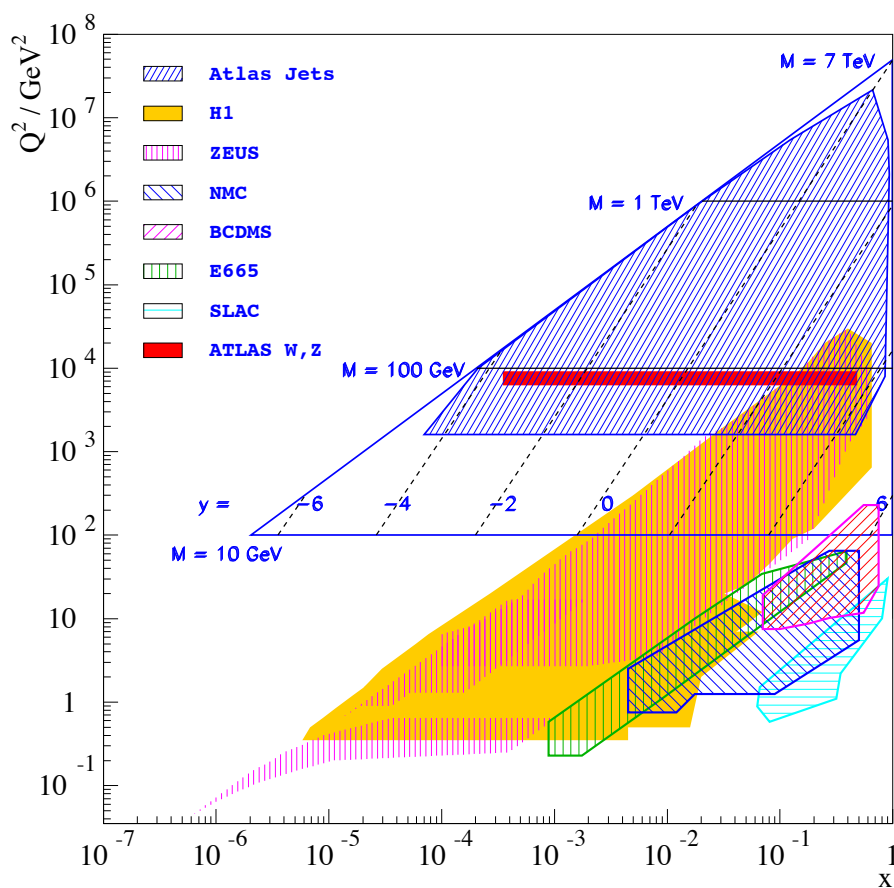


**Figure 2.8:** The phase space coverage in  $x, Q^2$  for DIS experiments at HERA and other fixed target experiments, as well as in  $M, y$  for Drell-Yan processes at the Tevatron and LHC at  $\sqrt{s} = 7 \text{ TeV}$ .

### 2.4.1 Z Boson Measurements

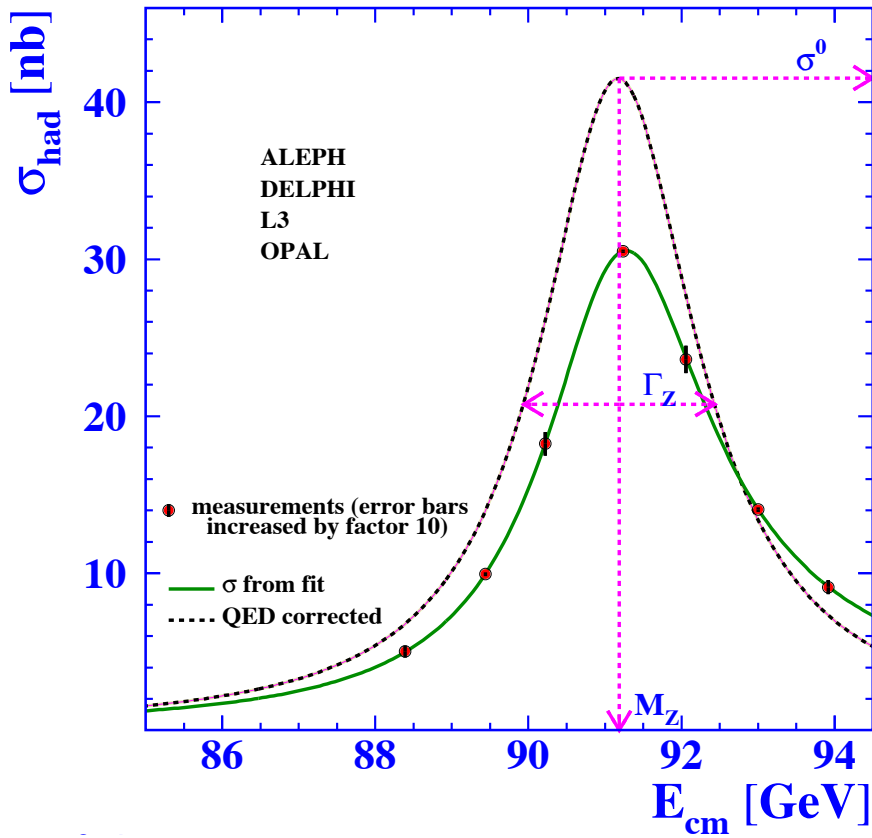


**Figure 2.9:** Average over measurements of the hadronic  $Z$  cross sections by the four experiments, as a function of centre-of-mass energy. The solid line is from model-independent fits to the data while the dashed line includes corrections for QED effects [18].

The properties of the  $Z$  boson were measured to good precision with the LEP  $e^+e^-$  collider at CERN which operated from 1989 – 2000. The four experiments, ALEPH, DELPHI, L3, and OPAL produced results that were combined giving a measurement of the  $Z$  boson mass as  $m_Z = 91.1875 \pm 0.0021$  GeV and the width as  $\Gamma = 2.4952 \pm 0.0023$  GeV assuming lepton universality [18]. A plot showing a fit to the combined data is shown in Fig. 2.9.

Further detailed measurements have been conducted in subsequent experiments, including recent results from the LHC. A measurement of the inclusive  $Z/\gamma^*$  cross sections in  $e$  and  $\mu$  decay channels was made by the ATLAS Collaboration in proton-proton collisions at  $\sqrt{s} = 7$  TeV and the dielectron mass spectrum from this measurement can be seen in Fig. 2.10 [19]. This data was collected in 2010 with an integrated luminosity of  $36 \text{ pb}^{-1}$ .

The combined  $Z \rightarrow ee$  and  $Z \rightarrow \mu\mu$  measured cross section as a function of  $|y_Z|$  is compared to predictions from various PDFs in Fig. 2.11. The discriminating power on PDFs of the measured Drell-Yan cross section is seen in this figure.

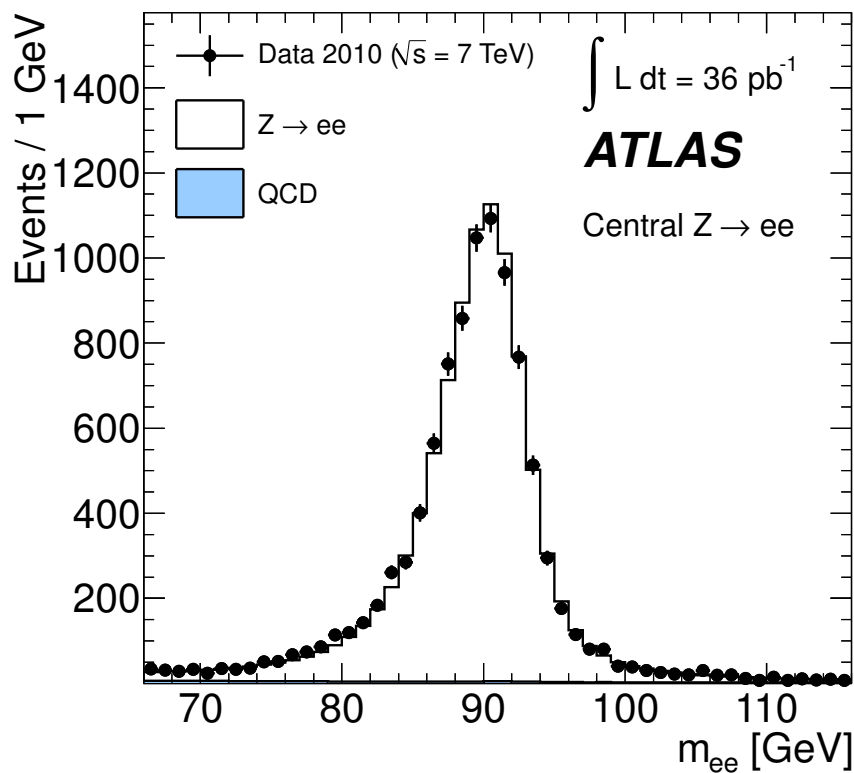


**Figure 2.10:** The dielectron invariant mass as measured by the ATLAS experiment using data collected in 2010 with an integrated luminosity of  $36 \text{ pb}^{-1}$ . The QCD background shape is taken from a control sample and normalised to the result of the QCD background fit. The distribution is from central electrons, i.e. those with absolute pseudorapidity  $|\eta| < 2.47$ .

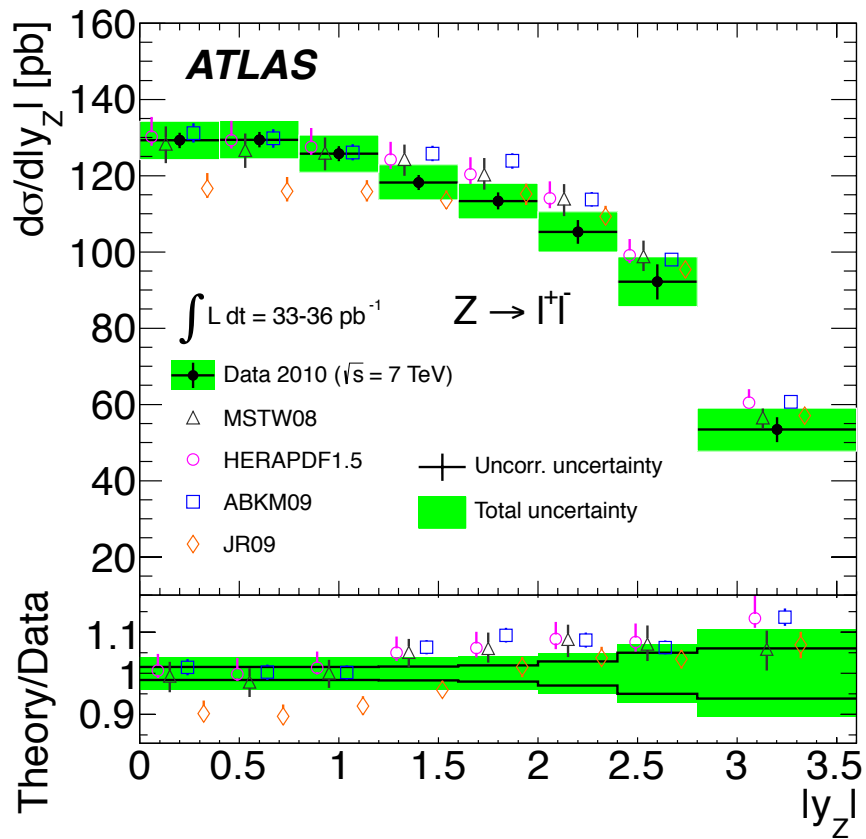


**Figure 2.11:** Differential  $d\sigma/d|y_Z|$  cross section measurement for  $Z \rightarrow \ell\ell$  compared to NNLO theory predictions from different PDF sets using data collected in 2010 with an integrated luminosity of  $36 \text{ pb}^{-1}$ . This plot exhibits the discriminating power of measured Drell-Yan data on PDFs.

A distribution showing the Drell-Yan invariant mass spectrum taken from  $4.5 \text{ fb}^{-1}$  of data collected in 2011 by the CMS Collaboration is shown in Fig. 2.12 [20]. The data are compared to NNLO predictions and show good agreement.

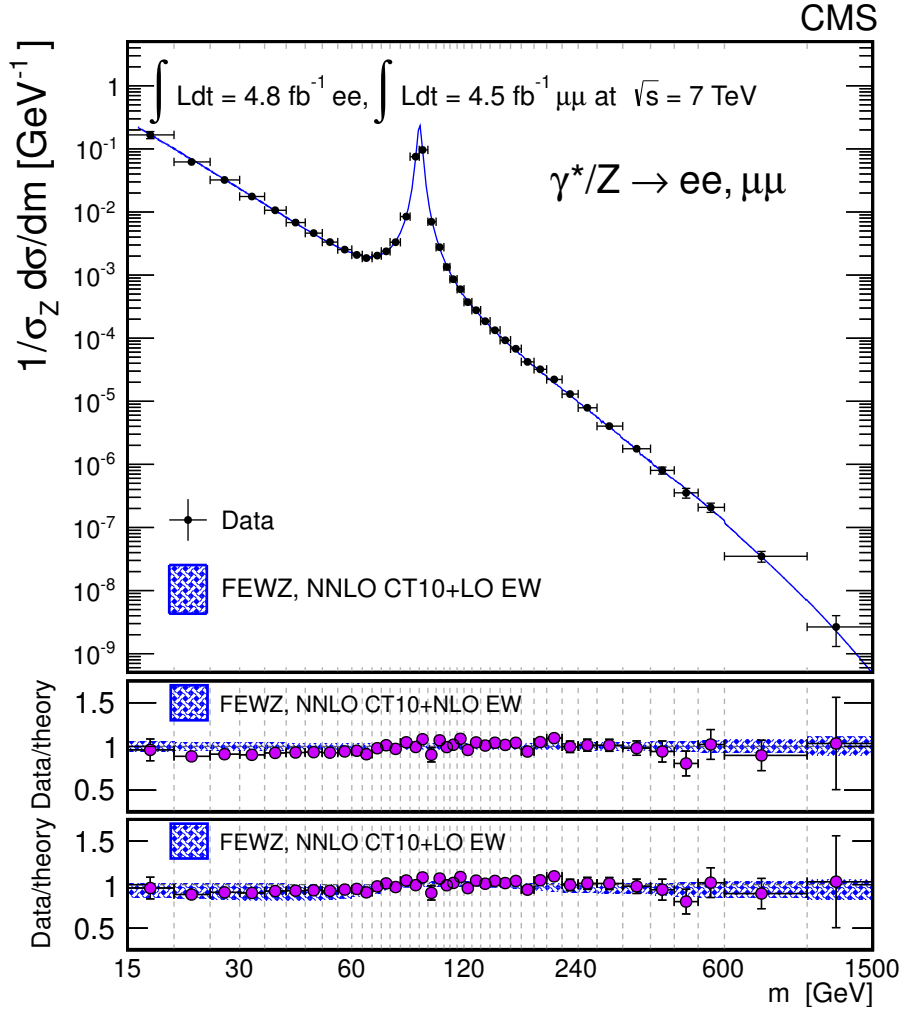


**Figure 2.12:** The Drell-Yan invariant mass spectrum as measured by the CMS Collaboration using data taken from  $pp$  collisions at the LHC in 2011

## 2.5 Theoretical Predictions and Monte Carlo Generators

Theoretical QCD cross section predictions can be calculated using tools such as *FEWZ* (Fully Exclusive W and Z Production) [21]. *FEWZ* can simulate lepton pair production through Drell-Yan processes at hadron colliders at NNLO. *FEWZ* can be configured to produce differential cross section calculations within experimental acceptance cuts. Additional NLO electroweak corrections can also be applied.

Monte Carlo (MC) simulation is an important tool in physics analysis. Theoretical pre-

dictions for physics processes can be made and used to simulate collisions accounting for the detector geometry and performance.

The basic requirements for an MC generator to be used to simulate processes at the LHC are that it should describe the hard scattering process, parton shower (PS), hadronisation, the underlying event from secondary interactions, as well the structure of the colliding hadrons (PDFs). The hard scattering process is propagated as a *Matrix Element* (ME).

Perturbation theory is used to calculate the ME to a certain order, thereby fixing the number of outgoing partons. Additional partons are described by the PS, which is a probabilistic evolution of parton splitting in time.

It's possible for the PS to simulate a parton emission that was also simulated in the ME, and so to avoid double counting, matching between the ME and PS should be performed.

There are a number of generators available to perform these simulations and an overview of those used in this analysis is given below.

PYTHIA [22] is a multipurpose event generator which can be used to describe hadronic and leptonic collisions, as well as hadron-lepton collisions. It provides simulation of hard and soft interactions, parton distributions, parton showering, as well as simulation of multiple interactions. The hard scattering is described to an LO approximation.

HERWIG [23] is also used to simulate hadronic final states from hadronic, leptonic, and hadron-lepton collisions. Similarly to Pythia, it describes the hard scattering process to an LO approximation.

POWHEG [24–27] is a generator used to generate the hardest emission first at NLO. POWHEG can then be interfaced to a shower generator for combined simulation of the hard and soft processes. This can be done whilst maintaining the NLO accuracy of the hard emission and the leading log accuracy of the shower.

MC@NLO [28] is used to generate parton showers as well as computing hard subprocesses by performing full NLO QCD corrections.

Each of these generators uses a generic interface as established by the *Les Houches accord* in 2001 [29]. This makes it straightforward to combine the ME and PS from different generators.

### 3 The Large Hadron Collider

The Large Hadron Collider (LHC) at CERN is currently the most powerful particle accelerator in the world. The accelerator ring lies in a  $\sim 27$  km tunnel 45–170 m below ground at the Franco-Swiss border near Geneva [30]. The LHC is served by a pre-existing accelerator complex which progressively increases the energy of the protons at each stage, starting from containers of hydrogen gas.

#### 3.1 The LHC Accelerator Complex

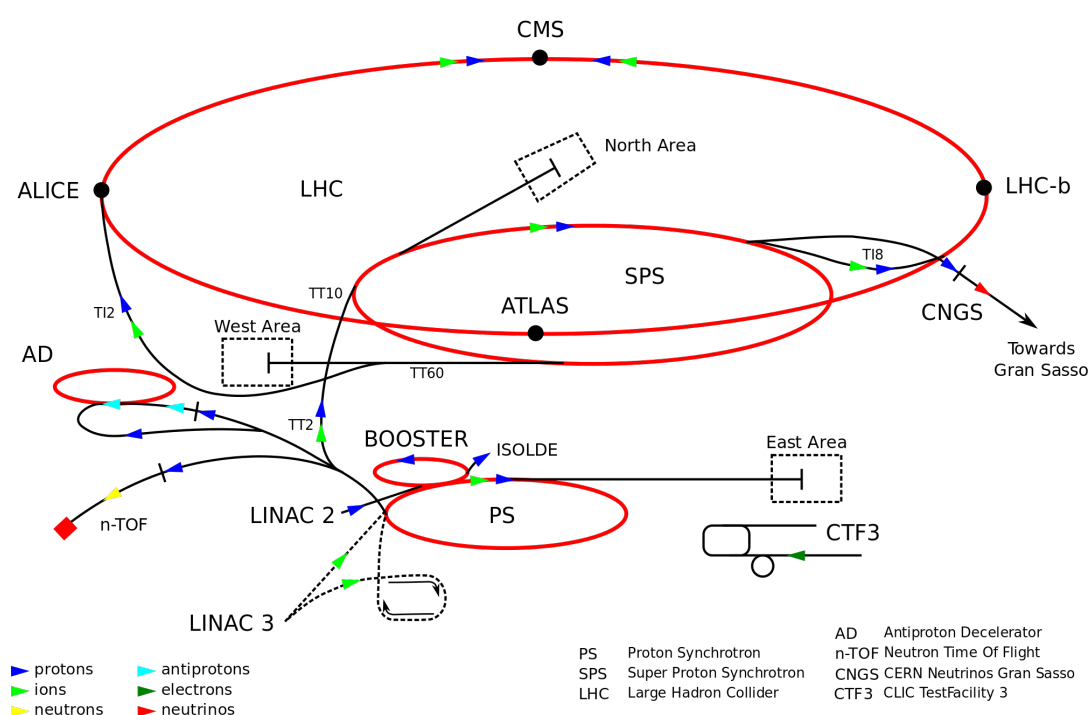


**Figure 3.1:** The CERN accelerator complex.

First, the hydrogen atoms are stripped of their electrons using an electric field, yielding protons. These are then passed to the only linear accelerator in the chain, LINAC2 which accelerates the protons up to 50 MeV, at which point they are injected into the Proton Synchrotron Booster (PSB) which pushes them to 1.4 GeV. The final links in the chain before injection into the LHC are the Proton Synchrotron (PS), and Super Proton Synchrotron (SPS), accelerating the protons to 25 and 450 GeV respectively. They are then accelerated in the LHC itself up to 3.5 TeV (design energy of up to 7 TeV) at which point the proton beams are circulated in opposite directions in different beam pipes in the accelerator ring while simultaneously being prepared for collisions at the four main interaction points corresponding to the four main experiments at

the LHC: ATLAS [31], CMS [32] [33], LHCb [34], and ALICE [35]. The layout of the CERN accelerator complex can be seen in Fig. 3.1 [36]. Many of the accelerators are used for other purposes aside from LHC physics.

### 3.2 Beam Preparation

The trajectory of the beams around the LHC is controlled by dipole magnets which bend the beam through the eight arced sections and eight straight sections of the tunnel.

An important step before injection to the LHC is bunch splitting, which is performed mostly in the PS and SPS. The particles are accelerated using a radio-frequency (RF) technique where they undergo oscillations in time and energy. A beam of particles can be split into bunches by boosting periodic harmonics of the RF [37]. The LHC has a nominal bunch pattern of 39 groups of 72 bunches with a bunch spacing of 25 ns — a total of 2808 bunches with  $10^{11}$  protons per bunch. The spacing between groups is variable to accommodate the injection and extraction magnet rise times.

In preparation for collisions, the beams are focused transversely using quadrupole magnets. A focusing in one transverse plane results in defocusing in the perpendicular plane, so the focusing plane is alternated from one quadrupole to the next. These magnets are alternately distributed with the bending dipoles along the beam line. All of the magnets are superconducting and need to be cooled to 1.9 K to maintain their superconductivity.

### 3.3 Luminosity

The number of events for a certain process is related to the cross section by the formula  $N = \sigma \int \mathcal{L} dt$  so it is important to optimise the beam properties to maximise luminosity. The luminosity delivered is given by [38]:

$$\mathcal{L} = \frac{n_b f_r n_1 n_2}{2\pi \Sigma_x \Sigma_y} \quad (3.1)$$

where  $n_b$  is the number of bunches per beam,  $f_r$  is the revolution frequency of the LHC ring,  $n_{1,2}$  are the numbers of protons in colliding bunches 1 and 2, and  $\Sigma_{x,y}$  are the horizontal and vertical beam profile widths. From this formula it can be seen how important beam focusing is, as a reduction in the transverse width of the beams results in an increase in the instantaneous luminosity.

The ATLAS and CMS (Compact Muon Solenoid) experiments are the two largest at the LHC, and the detectors are multipurpose, designed to cover a wide range of physics goals at high energies. Despite their similar experimental aims, the two experiments are significantly different in their design, which is important for simultaneous validation of physical observations. LHCb is a specialised detector designed for research into the physics of  $b$ -quark

---

interactions, which involves many precision measurements. ALICE (**A Large Ion Collider Experiment**) is designed to study heavy-ion collisions which also take place at the LHC. The wide physics program at the LHC calls for a maximisation of process cross sections, so luminosity, and therefore beam preparation, is an important part of the LHC operation.

## 4 The ATLAS Detector

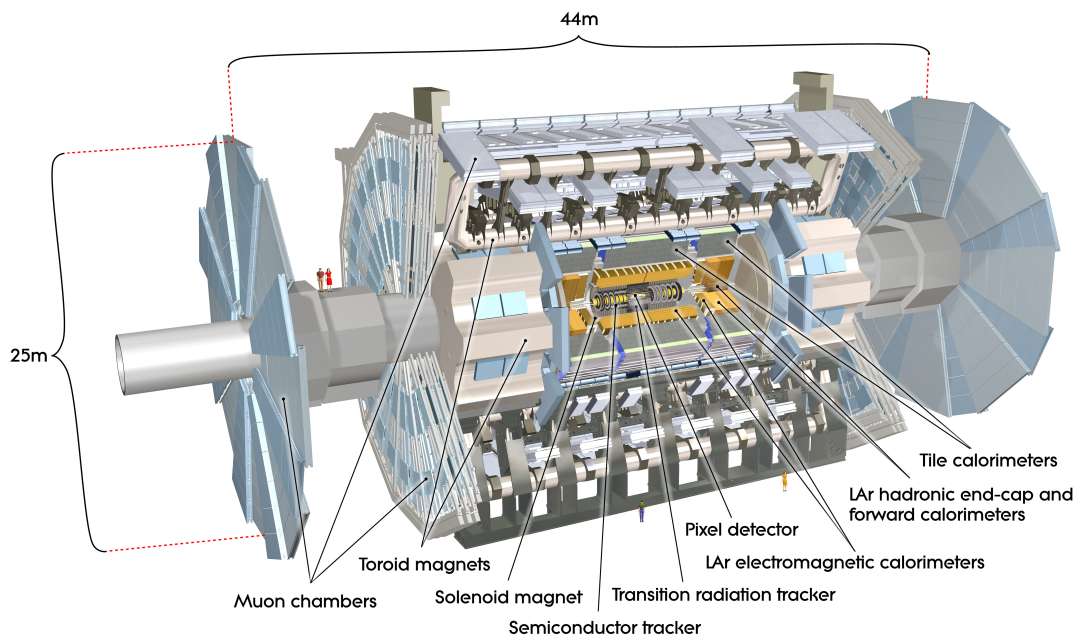


**Figure 4.1:** A schematic cut-away drawing of the ATLAS detector showing its different sub-components. [39]

The LHC is a machine designed to extend the energy frontier in high energy physics. The collisions resulting from such high energies yield complex systems in harsh environments that have previously never been probed. Sophisticated tools and techniques must be developed to observe these events and develop an understanding of the processes that produced them. Such sophistication necessitates complexity, and so to describe the world of the very small, machines of unprecedented size and scope are required. ATLAS is one such machine, and along with CMS is one of two general purpose detectors at the LHC. The detector is designed to exploit the physics potential of the LHC throughout its operation.

In addition to precision measurements of Standard Model (SM) processes, it also has the capability for searches of new signatures both within and beyond the SM. One such search, and an early success for ATLAS and the LHC yielded the discovery of the Higgs boson, as announced in July 2012.

Many searches and precision measurements rely on the exploitation of conservation of transverse momentum. For example ATLAS does not detect neutrinos directly, but by measuring the amount of missing transverse energy in an interaction. The only way to keep track of missing energy is by measuring the energy of all the detectable particles produced in an event.

An energy imbalance, where the net transverse energy is not equal to zero, implies that some of the energy in the interaction is being carried by a particle that was not detected. Therefore it is important to hermetically cover the area around the interaction point.

ATLAS can be considered as a number of sub-detectors with each component suited to a particular set of measurements or type of detection. The sub-detectors can be further classified into systems. In particular it is useful to consider three such classifications:

- The Inner Detector (ID)
- The Calorimetry System
- The Muon System

The layout of these systems and their sub-detectors can be seen in the schematic drawing of the ATLAS detector in Fig. 4.1. The functions and technical aspects of each system are described below.

## 4.1 The Magnet System

ATLAS relies on, and indeed is named for, its magnets. A charged particle moving through a magnetic field will have a curved trajectory, and the curvature can be used to measure the momentum of the particle. There are two regimes of magnetisation in ATLAS, defined by two magnet systems. The first is the solenoid system which surrounds the ID and provides its detectors with a magnetic field, and the second is the toroid system which lies partly within the muon system, but surrounds the calorimeters, and gives ATLAS its name. Both systems are superconducting and are cooled to around 4.5 K. The solenoid produces an axial field along the  $z$ -axis of the detector which is between 2 T and 1.8 T near the centre of the ID,  $0 \leq z \leq 1.7$  m, but falls to 0.8 T at the ends of the ID,  $z = 3$  m [40]. This non-uniformity is a consequence of the solenoid being shorter in  $z$  than the ID system. The toroidal system induces field lines perpendicular to those of the solenoid, with a peak strength of 3.9 T in the barrel and 4.1 T in the end-caps.

## 4.2 The Inner Detector

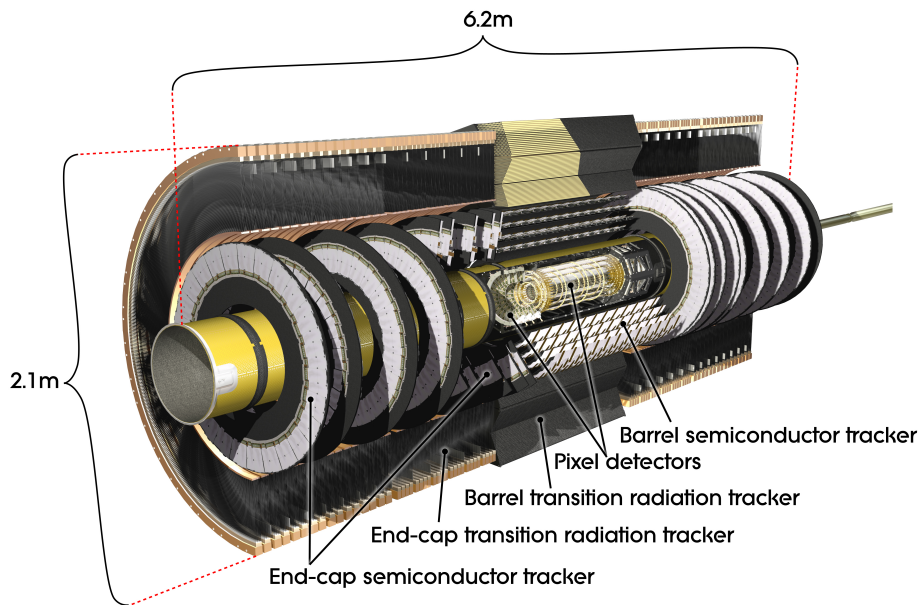


**Figure 4.2:** Image of the ATLAS inner detector [41].

The vast numbers of protons in each bunch coupled with the strive to maximise luminosity (see Secs. 3.2 and 3.3) presents an interesting problem for the detectors called pileup. The pileup effect describes the fact that it is possible for simultaneous multiple interactions to occur when the bunches in the proton beams collide. Many particles are produced as a result of these collisions and leave myriad signals in the detector systems. High resolution detection is necessary to identify the primary vertex, or initial interaction point, of an event. Secondary vertices are also important in identifying many interesting physics processes, while reconstructing the trajectories of charged particles provides useful identifying information about them. Tracking and vertex reconstruction is the job of the ID. Three sub-components, individual detectors in their own right, make up the ATLAS ID. In order of increasing distance from the beam pipe, they are:

- The Pixel Detector
- The Semiconductor Tracker (SCT)
- The Transition Radiation Tracker (TRT)

### 4.2.1 The Pixel Detector

The Pixel Detector consists of three barrel layers, and three disk layers at each end of the barrel region. It, and the other ID components cover a pseudo-rapidity range of  $|\eta| < 2.5$ . It provides high precision three-dimensional vertexing of charged tracks with a longitudinal spatial resolution of  $\sigma(z) < 1$  mm [42]. Material is kept to a minimum to reduce the number of secondary interactions as well as multiple scattering. Its secondary vertexing capabilities allow for identification of short lived particles such as  $b$ -quarks and  $\tau$ -leptons.

Detection takes place by the charge deposition in a charge-depleted layer of silicon resulting from ionisation of a charged particle traversing the pixel. There are approximately 80 million pixels (read-out channels), 67 million across the three barrel layers and 13 million in the end-caps. Each pixel detects a signal over its ionisation threshold and the charge distribution over adjacent pixels identifies the hit position.

### 4.2.2 The Semiconductor Tracker

The Semiconductor Tracker (SCT) also uses silicon but in semiconducting strips instead of pixels. A charged particle passing through the silicon creates electron hole pairs through ionisation.

The SCT is constructed as a barrel and two end-cap sections. The barrel consists of 2112 individual silicon strip modules in four cylindrical layers, and each end-cap consists of 988 modules laid out over nine disks. The shape of the modules within the end-cap is optimised based on its distance from the interaction point.

There are 61 million total read-out channels across the  $61m^2$  of the SCT.

### 4.2.3 The Transition Radiation Tracker

The Transition Radiation Tracker (TRT) consists of cylindrical straws each filled with a gas mixture of Xenon (70%), CO<sub>2</sub> (27%), and Oxygen (3%) [43]. There is a wire anode in the centre, and the surface of the straw acts as a cathode. The gas is ionised by passing charged particles and the ionised charge clusters drift to the anode. The time taken for this drift is measured and converted to distance which gives the drift radius. This is used to determine the track of the particle through the straws.

This is not the only job of the TRT – as its name suggests it also uses transition radiation to distinguish particles. This is achieved through the production of a rapidly varying dielectric constant from radiator material between the straws. This causes emission of x-ray photons (transition radiation photons). Electrons and minimum-ionising particles, e.g. pions, can be distinguished by the different energies of their transition radiation depositions.

The TRT achieves the double work of tracking and particle identification by using two

thresholds. Tracking is performed when freed electrons from a low ionisation threshold drift towards the wire, while transition radiation detection uses a threshold about twenty times larger.

### 4.3 The Calorimeter System

The ATLAS calorimeter system measures the energies of particles. This is useful in particle identification, providing useful information for the identification of electrons, photons, jets, and by inference, missing transverse energy.

A barrel and two end-cap components provide coverage in  $|\eta| < 3.2$ , and the forward calorimeter covers  $3.1 < |\eta| < 4.9$ . The system covers  $\phi$  around the beam pipe in full.

Calorimetry is performed by sampling, whereby the energy of a particle traversing the calorimeter is absorbed. The interaction of the particle with the calorimeter material produces a shower of secondary particles. The size and shape of this particle shower is governed by the initial particle or jet of particles that caused it, making it useful in identifying and selecting physics objects.

There are two types of particle shower: electromagnetic (EM), and hadronic. Concordantly the calorimetry system comprises of two parts, each designed to measure one type of particle shower. These are the electromagnetic calorimeter (EMCAL), and the hadronic calorimeter (HCAL).

The profile of an EM shower is very different to a hadronic one, and this is exploited in the design of the calorimetry system. Typically, EM showers are shorter in length than hadronic showers, and for this reason the EMCAL is situated closer to the beam pipe than the HCAL. The unique features of each shower type are described below.

The majority of the material in both calorimeters consists of energy-absorbing material, which causes the showering, and sampling material, which measures the deposit.

The calorimetry system is shown in Fig. 4.3.

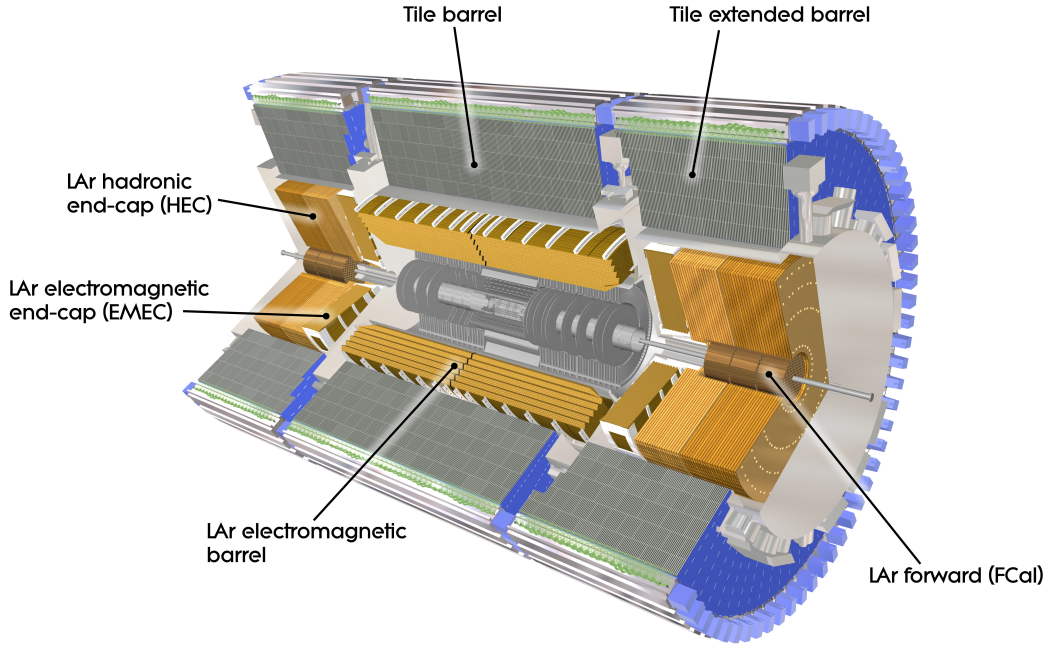


**Figure 4.3:** The ATLAS Calorimeter system [44]. The location of each calorimeter in relation to the beam pipe can be seen. The EMCAL lies closest to the beam pipe as EM showers are typically shorter in length than hadronic showers.

### 4.3.1 The EM Calorimeter

Photons interact with the absorber and then primarily undergo pair-production of an electron and positron. The interaction of electrons and positrons with the absorber leads to the emission of photons by the process of bremsstrahlung.

The showering continues until the energy of the photons is below the pair-production threshold, and processes other than bremsstrahlung begin to dominate the energy loss of electrons. The depth at which this happens depends on the material and is measured in terms of radiation length,  $X_0$ , which is the distance at which an electron loses all except  $1/e$  of its energy, and  $7/9$  of a photon's mean free path for pair-production.

The barrel EMCAL consists of lead encased in stainless steel as the absorbing material, and liquid argon (LAr) as the sampling material.

The structure is arranged in an accordion geometry to provide full coverage in  $\phi$ . The calorimeter is constructed in the shape of two barrel calorimeters (EMB) covering  $-1.475 < \eta < 0$  and  $0 < \eta < 1.475$ , and two discs at the outer end of each barrel, called end-caps (EMEC), covering  $3.2 < \eta < -1.375$  and  $1.375 < \eta < 3.2$ .

The depth of the calorimetry system is at least  $24X_0$  from the interaction point to the end

of the active material [45].

The EMCAL consists of three sampling layers of varying  $\Delta\eta \times \Delta\phi$  granularity at different  $\eta$  ranges. The first sampling has a resolution of between  $0.003 \times 0.1$  and  $0.006 \times 0.1$  in the central region ( $|\eta| < 2.5$ ), and  $0.1 \times 0.1$  in  $2.5 < |\eta| < 3.2$ . The resolution of second sampling is  $0.025 \times 0.025$  in the central region, and  $0.1 \times 0.1$  in  $2.5 < |\eta| < 3.2$ . The resolution of the third sampling is fixed at  $0.050 \times 0.025$  and this layer only extends up to  $|\eta| < 2.5$ .

The second sampling is the main sampling layer and collects most of the energy of the EM shower. In addition to the three sampling layers, there is a presampler (PS) in front of the the first layer. This is used to correct for energy loss upstream of the EMCAL through the particles interacting with other material in the detector. The PS is a thin layer of liquid argon and has a resolution of  $0.025 \times 0.1$  in  $\Delta\eta \times \Delta\phi$ . It covers  $|\eta| < 1.8$ .

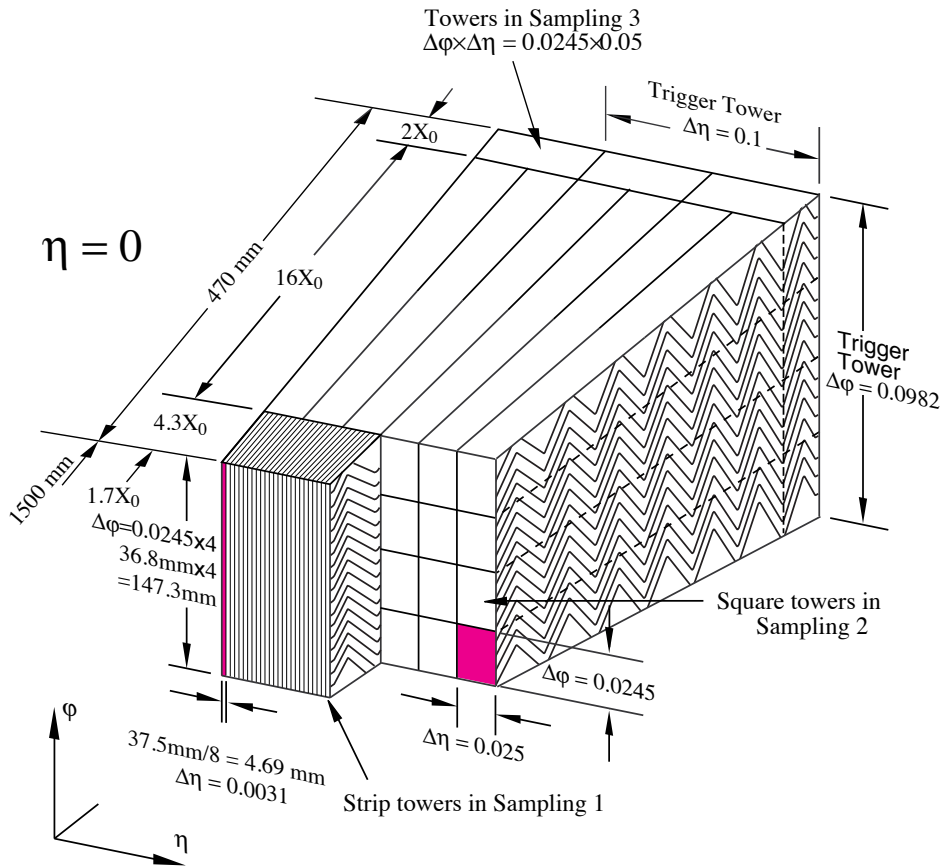


**Figure 4.4:** The layout of an EMB module in the ATLAS EMCAL. The accordion structure, geometry, and layout of the three sampling layers can be seen.

### 4.3.2 The Hadronic Calorimeter

The primary task of the HCAL is to reconstruct jets from quarks and gluons and measure their energy. A significant distinction between hadronic and EM showers is their depth; the hadronic interaction length is larger than the radiation length  $X_0$ , so hadronic showers take longer to cascade than EM showers.

The HCAL consists of two distinct subsystems: the tile calorimeter, and the LAr calorimeters. The tile system is constructed in the shape of barrels, one central barrel covering  $|\eta| < 1$ , and two extended barrels covering  $0.8 < |\eta| < 1.7$  either side of the interaction point. These can be seen in Fig. 4.3. The absorber in the tile calorimeter is steel and the active sampling material is scintillating plastic [46].

The hadronic LAr calorimeters consist of two end-caps (HEC) covering  $1.5 < |\eta| < 3.2$  and the forward calorimeter (FCAL), covering  $3.1 < |\eta| < 4.9$ . The absorber in the HEC is copper.

The FCAL's location exposes it to very high levels of radiation, and must be dense to prevent energy passing through unabsorbed. It is split into three modules, the first of which, FCAL1, uses copper as the absorber. The other two, FCAL2 and FCAL3 both use tungsten. Containment of all the energy in the particle shower is necessary to provide an accurate measurement of missing transverse energy.

FCAL1 is well-suited to measure EM showers, while FCAL2 and FCAL3 are optimised for hadronic measurements.

## 4.4 The Muon System

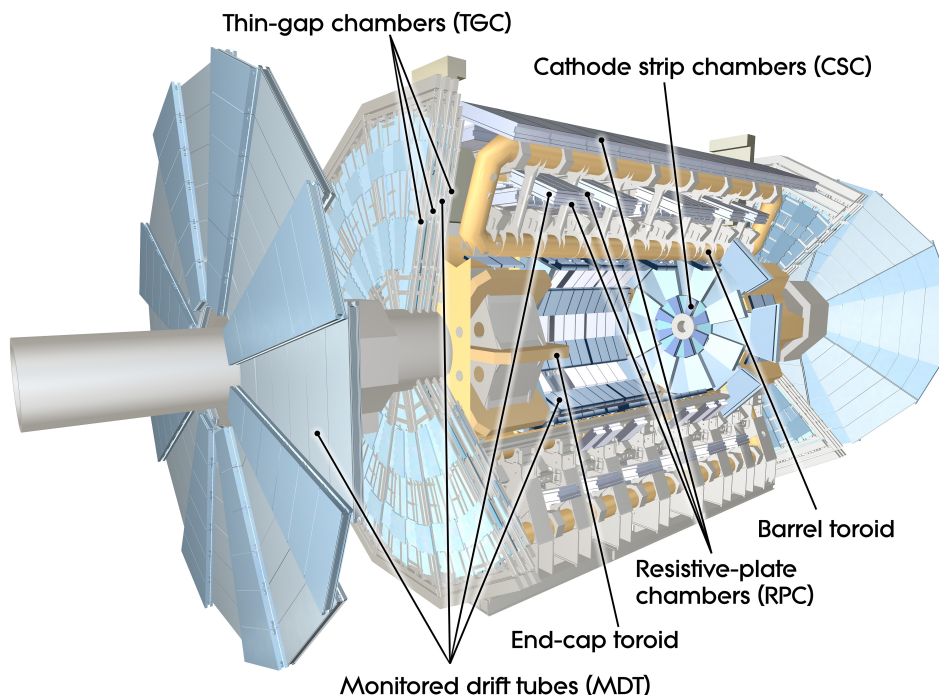


**Figure 4.5:** Cut-away view of the ATLAS muon system [47]

The ATLAS muon system is designed to serve as both a muon spectrometer and a trigger to select events with high energy muons. The spectrometry system is designed to measure 1TeV muons with a momentum resolution of 10%.

A large barrel toroid and two end-cap toroids produce a bending magnetic field. *Monitored Drift Tube* (MDT) chambers are used for precise track measurements in  $|\eta| < 2.4$ . In the forward region close to the interaction point, the rate is too high for MDTs and so *Cathode Strip Chambers* (CSCs) are used. *Resistive Plate Chambers* RPCs are used for triggering in the barrel region, while *Thin Gap Chambers* (TGCs) are used in the end-caps. The layout can be seen in Fig. 4.5.

## 4.5 The Trigger System

At design luminosity, the LHC has an interaction rate of around 1 GHz. There are about 23 interactions in each bunch crossing, which corresponds to a bunch-crossing rate of 40 MHz. The average storage size of a single event is 1 MB [48]. From a computer processing and storage point of view, it is impractical to store each event and so decisions must be made online to reduce this rate without discarding interesting events. This is the goal of the ATLAS

trigger system. The rate reduction is performed in three stages, *Level 1* (L1), *Level 2* (L2), and the *event filter* (EF). The L2 trigger and EF together form the *High-Level Trigger* (HLT). Figure 4.6 shows the procedural layout of the trigger system. The ATLAS trigger system covers the central region of the detector,  $|\eta| < 2.5$ .

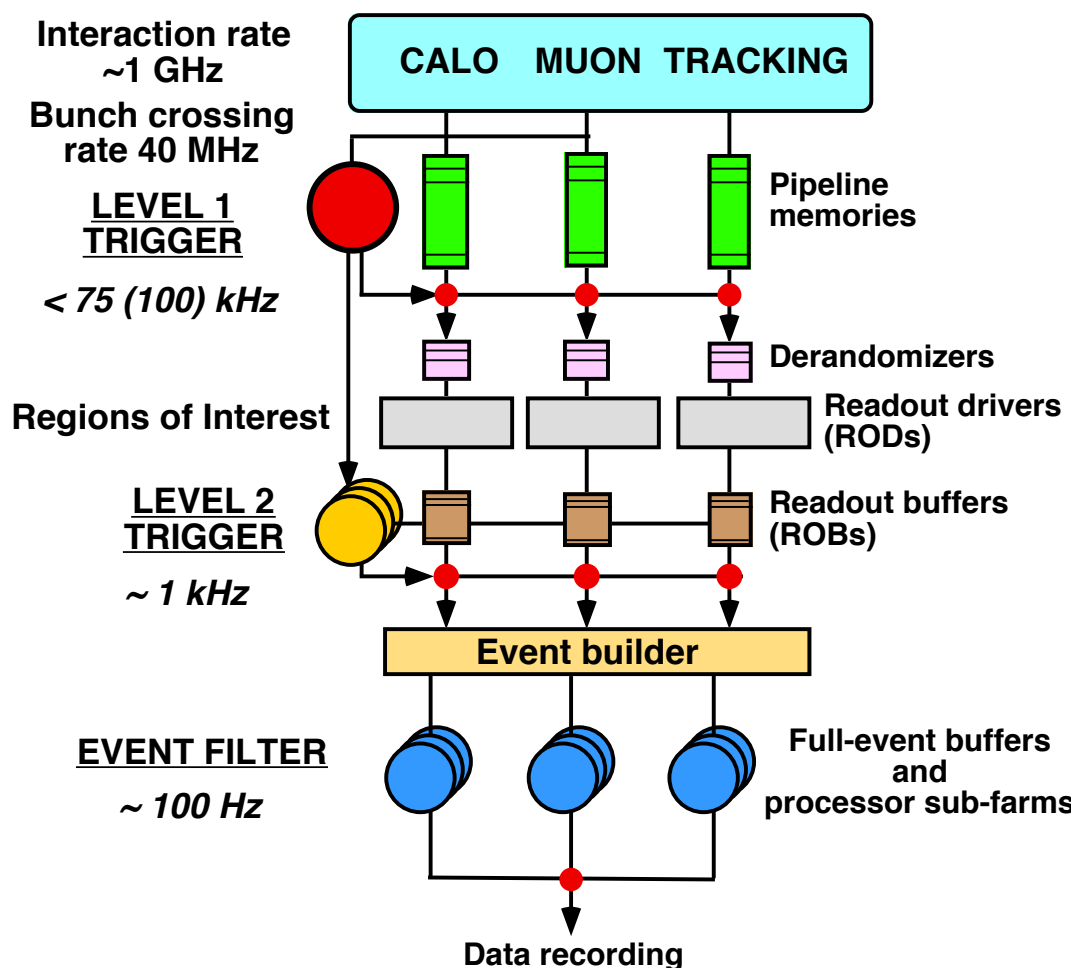


**Figure 4.6:** The three levels of the ATLAS trigger system. The event rate at each level is also shown, illustrating the impact of each level's selection on the number of stored events.

The L1 trigger uses the multiplicity of physics objects above various  $p_T$  thresholds in the relevant subcomponents in ATLAS to perform its decisions. This is done using simple algorithms applied at a hardware level for speed, and the overall decision time is  $\sim 2 \mu\text{s}$  including transmission of the signal from the detector to the read-out electronics. The event rate is reduced to 75 kHz after the L1 trigger processing.

Another important job of the L1 trigger is defining regions of interest (ROIs) to seed the L2 trigger. An ROI contains as the position in  $\eta$  and  $\phi$  of the object, as well as the  $p_T$  threshold range.

The L2 trigger takes the information from an ROI and examines it with finer granularity in a window around the seed coordinates. L2 selection is software-based and reduces the event rate down to the order of 1 kHz with an average processing time per event of 40 ms. An event passing the L2 requirements is taken to the event builder (EB) which collates the information from the readout buffers (ROBs) to into the full event. The event is passed from there to the EF.

The EF uses the full granularity information available to classify and store events. The selection is performed by applying offline algorithms to reconstruct measured quantities and build the object while also applying offline corrections. This analysis is performed on the order of a few seconds, and reduces the event rate to  $\sim 100$  Hz.

## 5 Measurement of the $Z \rightarrow ee$ Inclusive Cross Section

The measurement of the  $Z \rightarrow ee$  inclusive differential cross section as a function of mass is described in this chapter.

An overview of the data collected and Monte Carlo samples used is presented in sections 5.1 and 5.2.

The methodology of the measurement is introduced in Sec. 5.3, followed in Sec. 5.4 by a description of how electrons are reconstructed and identified in ATLAS, which informs the criteria required of the data collected and Monte Carlo simulated to select  $Z \rightarrow ee$  events. The selection is detailed in Sec. 5.4.5.

The impact of electron identification on the cross section measurement is discussed in Sec. 5.5 with a consideration of the effect of correcting for differences between data and simulated events.

Estimation of the background contribution to the final selected sample and associated uncertainties is performed in Sec. 5.7.

### 5.1 Data Sample

The ATLAS detector collected a total of  $5.34 \text{ fb}^{-1}$  of proton collision data in the 2011 data taking period at beam energies of 3.5 TeV. The conditions of the detector as well as parameters of the LHC beam varied throughout this period. The data collected by ATLAS is therefore split into *data periods* where each period represents fairly stable conditions. There are small variations within periods, such as a change in the number of colliding bunches between runs. A list of periods and the data luminosity collected in each period is shown in Tab. 5.1.

This analysis considers periods D–M. Period A is neglected as it consisted of trigger commissioning and both the solenoid and toroid magnets (see Sec. 4.1) were switched off. Period B is neglected as the toroid was off for part of this period. Period C was not considered as the beam energy was 1.38 TeV.

Each run is separated into sub-units called luminosity blocks (LBs). An LB in the 2011 run is about 60 seconds of data collection [38]. Separation of the data into discrete blocks of this size allows for high granularity examination of the conditions of the data.

LBs are defined by a set of parameters called data quality (DQ) flags. These flags are an indicator of the status of each sub-detector, or the algorithm applied to reconstruct e.g. a muon.

The state of these flags is used to select or reject LBs using Good Run Lists (GRLs). Each GRL is produced by requiring the DQ flags for a particular set of data to be in a certain state. A GRL is a list of LBs which pass this criteria. Different analyses might have different requirements and so each GRL is tailored to that particular analysis.

The GRL used in this analysis is:

Period	Runs	Luminosity [ $\text{pb}^{-1}$ ]
<i>A</i>	<i>177531 – 177965</i>	<i>8.7</i>
<i>B</i>	<i>177986 – 178109</i>	<i>18</i>
D	179710 – 180481	182
E	180614 – 180776	52
F	182013 – 182519	156
G	182726 – 183462	566
H	183544 – 184169	283
I	185353 – 186493	406
J	186516 – 186755	237
K	186873 – 187815	676
L	188902 – 190343	1599
M	190503 – 191933	1160

**Table 5.1:** The luminosity per data period collected in 2011 by the ATLAS detector at beam energies of 3.5 TeV. Period C is not shown as the beam energy for this period was 1.38 TeV. Periods shown in *italics* were not used in this analysis.

`data11_7TeV.periodAllYear_DetStatus-v36-pro10_CoolRunQuery-00-04-08_WZjets_allchannels_DtoM.xml`

which was produced by the ATLAS W,Z physics group to be used for muon and electron analyses.

The integrated luminosity of the 2011 data after application of this GRL is  $4.58 \text{ fb}^{-1}$  with a systematic uncertainty of 1.8% [49].

## 5.2 Monte Carlo Samples

MC samples were used in this analysis to tune the data, extrapolate the measurement to various fiducial volumes, simulate background processes, and evaluate systematic uncertainties.

A list of the samples used and the generators used to produce them is presented in Tab. 5.2. A description of the different generators was given in Sec. 2.5.

The cross sections have associated uncertainties of the order of 3% from the choice of PDF, of the order of 4% for the correction from NLO to NNLO, as well as from factorisation and renormalisation. The total uncertainty is taken to be 5%.

The *alternate  $Z \rightarrow ee$  samples* listed are used to estimate the systematic uncertainty from the choice of ME and PS.

Process	Generator	$\sigma \cdot \text{BR} \cdot \epsilon_{filter}$ [nb]	$N_{evt}$ [ $10^6$ ]
Main $Z \rightarrow ee$ samples			
$Z \rightarrow ee$ ( $m_{\ell\ell} > 53.8$ GeV)	POWHEG PYTHIA6	1.006 (5%)	20
$Z \rightarrow ee$ ( $38 < m_{\ell\ell} < 53.8$ GeV)	POWHEG PYTHIA6	0.0878 (5%)	3
Alternate $Z \rightarrow ee$ samples			
$Z \rightarrow ee$ ( $m_{\ell\ell} > 53.8$ GeV)	POWHEG HERWIG	1.006 (5%)	10
$Z \rightarrow ee$ ( $38 < m_{\ell\ell} < 53.8$ GeV)	POWHEG HERWIG	0.0878 (5%)	3
$Z \rightarrow ee$ ( $53.8 < m_{\ell\ell} < 75$ GeV)	POWHEG HERWIG	0.04713 (5%)	3
$Z \rightarrow ee$ ( $m_{\ell\ell} > 105$ GeV)	POWHEG HERWIG	0.02464 (5%)	1.5
$Z \rightarrow ee$ ( $m_{\ell\ell} > 60$ GeV)	MC@ NLO	0.990 (5%)	5&5
$Z \rightarrow ee$ ( $40 < m_{\ell\ell} < 75$ GeV)	MC@ NLO	0.1151 (5%)	2.5
$Z \rightarrow ee$ ( $m_{\ell\ell} > 105$ GeV)	MC@ NLO	0.02418 (5%)	0.5

**Table 5.2:** Monte Carlo samples and generators used in this analysis to simulate the  $Z \rightarrow ee$  decay process. The quoted cross sections are used to normalise estimates of expected number of events.

### 5.3 Cross-Section Measurement Definition

$$\sigma \times BR = \frac{N - B}{C \cdot E \cdot A \cdot L_{int} \cdot \Gamma} \quad (5.1)$$

where

- $N$  is the number of selected  $Z \rightarrow ee$  events collected in data,
- $B$  is the estimated number of background events,
- $L_{int}$  is the total integrated luminosity of the collected data,
- $\Gamma$  is the bin width for differential measurements,
- $C$ ,  $E$ , and  $A$  are corrections calculated from MC.  $C$  is a correction factor to unfold the measurement to the *true experimental fiducial volume*.  $E$  and  $A$  are factors to extrapolate the measurement to the *common fiducial volume* and the *total cross section* respectively. These phase spaces and the correction factors are defined below. They are calculated using MC.

The  $C$  factor corrects for losses from the experimental selection and extrapolation to the fiducial phase space.

$$C = \frac{N_{MC, reco}}{N_{MC, gen, expfidu}} \quad (5.2)$$

where

- $N_{MC, reco}$  is the sum of MC event weights after reconstruction and event selection,
- $N_{MC, gen, expfidu}$  is the sum of MC event weights generated after fiducial cuts.

The  $E$  factor enters for the combination of different measurements. It extrapolates from the experimental fiducial region reached by  $C$ , to the common fiducial region.

$$E = \frac{N_{MC, gen, expfidu}}{N_{MC, gen, comfidu}} \quad (5.3)$$

where

- $N_{MC, gen, comfidu}$  is the sum of MC event weights generated after *common* (between the combined measurements) fiducial cuts.

The  $A$  factor extrapolates to the *total cross section*.

$$A = \frac{N_{MC, gen, comfidu}}{N_{MC, gen, mass}} \quad (5.4)$$

where

- $N_{\text{MC,gen,mass}}$  is the sum of MC event weights generated without any selection cuts, except for the cut on the di-lepton mass  $m_{\ell\ell}$  for  $Z/\gamma^* \rightarrow \ell\ell$  channels.

## 5.4 Event Reconstruction and Selection

Reconstruction of an event in the ATLAS detector is a sophisticated procedure involving selected subcomponents, tools, and algorithms designed to identify certain objects or processes. The key to reconstructing  $Z \rightarrow ee$  events is the identification of electrons.

### 5.4.1 Reconstruction of Electrons in ATLAS

The first stage in reconstructing an electron in ATLAS is requiring an object to pass an electron trigger. The cluster and track of the candidate electron must then be reconstructed and pass certain requirements referred to as 'electron identification'. These stages are described in the subsequent sections.

### 5.4.2 Electron Trigger

This analysis uses period-dependent di-electron triggers with a minimum  $p_T$  requirement of 12 GeV. The period dependence is a consequence of the increase in luminosity in later periods. The primary difference is an adjustment of the trigger threshold to restrict the L1 accept rate at higher instantaneous luminosities [50]. The triggers used in each period can be seen in Tab. 5.3.

Period	Di-Electron Trigger
D–J	2e12_medium
K	2e12T_medium
L–M	2e12Tvh_medium

**Table 5.3:** An overview of the period-dependent di-electron triggers used in this analysis.

Other adjustments include a veto on the hadronic energy deposited in the hadronic calorimeter, signified by the letters  $vh$  in the trigger name when accompanied by the threshold adjustment. Additional threshold adjustment was accomplished by tightening the L1 requirement without raising the HLT (see Sec. 4.5) threshold. This is indicated by the letter  $T$  in the trigger name. The triggers also implement a selection based on variables calculated from the properties of the EM showers and tracking of an event. Different requirements on these variables define various levels of background rejection. This is called *electron identification* and is described in Sec. 5.4.4. The triggers in this analysis all apply the *medium* requirement.

### 5.4.3 Electron Reconstruction

Reconstruction of electrons is performed using the EM calorimeter, which measures clusters of energy deposition, and the inner detector which reconstructs the tracks of charged particles

as described in Sec. 4.2.

The process involves a sliding window algorithm which searches for clusters with a total  $E_T$  greater than 2.5 GeV. The window is  $3 \times 5$  cells of the middle layer of the calorimeter. Found clusters are matched to reconstructed tracks from the inner detector if they lie within  $\Delta\eta \leq 0.05$ . An electron is reconstructed if at least one such match is performed.

It's possible for many tracks to be matched a single cluster, and in this case those tracks with a silicon hit take preference with the final candidate being chosen as the track closest to the seed cluster in  $\eta$ - $\phi$  space, i.e. the track with the lowest value of  $\Delta R = \sqrt{\Delta\eta^2 + \Delta\phi^2}$  relative to the seed cluster.

Information from the electromagnetic barrel (EMB) and endcaps (EMEC) of the calorimeter are then used to construct the final cluster, with the energy being calculated from the measured deposit in the cluster, as well as the estimated deposit in the material in front of the calorimeter, the estimated deposit outside of the cluster (lateral leakage), and the estimated deposit beyond the calorimeter (longitudinal leakage).

The final cluster is used to construct the four-momentum of the reconstructed electron, along with information from the track matched to the seed cluster. The track at the vertex defines the  $\eta$  and  $\phi$  directions of the reconstructed electron.

The above criteria are combined into algorithms depending upon which of the criteria the reconstructed object fulfills. These algorithms are assigned an *author* value, which distinguishes the different selections [51].

- **author = 1** is an algorithm based on clusterisation and is seeded by a cluster reconstructed in the EM calorimeter.
- **author = 2** is an algorithm based on tracking and is seeded by a track in the inner detector.
- **author = 3** is an algorithm which combines *authors* 1 and 2.

To avoid overlap between the two differently-seeded algorithms, clusterisation and tracking, an electron candidate which is assigned *author*=1 can not have been found with the track-based algorithm. Similarly an electron candidate which is assigned *author*=2 can not have been found with the cluster-based algorithm.

#### 5.4.4 Electron Identification

Identification of electrons is a cut-based process whereby a candidate is identified as an electron only if it passes certain criteria based on its calorimeter and track properties. These properties are used to distinguish between signal electrons, (which can be either isolated or non-isolated), background electrons, and fake electrons. The cuts can each be applied independently but are also combined into sets used as a standard reference in ATLAS. All of the ID cuts are

optimised in  $\eta$  and  $p_T$  bins of the cluster. In increasing order of background rejection, these sets are: *Loose*, *Medium*, and *Tight* [52].

The *Loose* set of cuts uses limited information from the calorimeters to perform a simple electron identification with relatively low background rejection, but high ID efficiency. The cuts are applied to the hadronic leakage and to variables of the shower shape in just the middle layer of the calorimeter (see Sec. 4.3.1).

The *Medium* set has the same cuts as the *Loose* set, but also adds cuts in the first layer of the calorimeter as well as requirements on some track variables. This level particularly effective at rejecting background events from the di-photon decay of a pion,  $\pi^0 \rightarrow \gamma\gamma$ , which has two distinct maxima in the first layer. In addition, the cuts on the track parameters as well as a on the distance in  $\eta$  between the track and the cluster increase jet rejection with respect to the *Loose* cuts by a factor of 3-4. The ID efficiency is reduced by  $\sim 10\%$ .

The *Tight* selection contains all the cuts included in the *Medium* set, as well as further requirements on the track-cluster matching, hits in the TRT, and cuts on the vertex information. The vertex requirement ensures that electrons from photon conversions are rejected. All of the particle-ID tools available for electrons are used in the *Tight* selection.

#### 5.4.5 $Z \rightarrow ee$ Event Selection

The trigger, reconstruction, and electron identification stages described in Sec. 5.4.1 are supplemented by additional requirements to select  $Z \rightarrow ee$  signal events while rejecting as many background events as possible. This analysis covers events in the central region of the detector,  $|\eta| < 2.5$ , thereby allowing for both electrons to pass the same trigger requirement.

The full selection is detailed below.

- Primary vertex with at least 3 tracks
- Event triggers the di-lepton trigger
- No more than two electrons each satisfying the following:
  - Author 1 or 3 (see Sec. 5.4.3)
  - IsEM Tight++ (see Sec. 5.4.4)
  - $p_T > 20$  GeV
  - $|\eta| < 2.47$ , excluding  $1.37 < |\eta| < 1.52$
- Di-electron invariant mass  $66 < m_{ee} < 116$

An additional cut is placed on the electron  $\eta$ , excluding the region  $1.60 < |\eta| < 1.70$  due to an efficiency loss in this range (see Sec. 5.5.4).

There were also some problems in the LAr calorimeter during data taking in 2011, meaning additional cuts were applied to reject adversely affected events. In particular, this meant rejecting events where a *noise burst* was observed in the calorimeter, as well as those which failed *object quality (OQ)* criteria. The main effect of the OQ cut was to remove events from runs where there were dead *front end boards (FEBs)* in the calorimeter.

The effect of each cut in the event selection can be studied using cut-flows, which show the number of events passing each cut in sequential order. This order can be arbitrarily selected in order to check the impact of certain cuts. Two such cut-flows are shown in Tables 5.4 and 5.5.

The online trigger cut should have very little inefficiency if placed at the end of the cut flow, signalling the ideal case of having tighter offline cuts. This is seen in Tab. 5.5 where the di-electron trigger has an efficiency of  $\sim 97\%$  for both data and MC after all offline cuts. The remaining  $\sim 3\%$  could be due isolation used in the trigger.

The invariant mass distribution after the full event selection in data, signal MC, and estimated background is shown in Fig. 5.1.

Cut	Data			MC		
	Events	$\epsilon_{rel}$ [%]	$\epsilon_{abs}$ [%]	Events	$\epsilon_{rel}$ [%]	$\epsilon_{abs}$ [%]
No Cuts	85309339	100.00	100.00	5008991	100.00	100.00
Prim. Vtx. with $\geq 3$ tracks	85269058	99.95	99.95	4975700	99.34	99.34
LAr noise bursts	85013877	99.70	99.65	4975700	100.00	99.34
Di-Electron Trigger	2980135	3.51	3.49	2424549	48.73	48.40
$ \eta_e  < 2.47$	2980135	100.00	3.49	2424549	100.00	48.40
excl. $1.37 <  \eta_e  < 1.52$	2582406	86.65	3.03	2186201	90.17	43.65
excl. $1.6 <  \eta_e  < 1.7$	2381091	92.20	2.79	2026880	92.71	40.46
Author	2380930	99.99	2.79	2026741	99.99	40.46
$p_T > 20$ GeV	1783662	74.91	2.09	1810010	89.31	36.14
OQ Cut	1762855	98.83	2.07	1788924	98.84	35.71
IsEM Tight++	993525	56.36	1.16	1156332	64.64	23.09

**Table 5.4:** A cut-flow showing the number of events passing each cut sequentially for data and Monte Carlo.  $\epsilon_{rel}$  is the efficiency relative to the previous cut in the sequence and  $\epsilon_{abs}$  is the efficiency relative to the total number of events before any analysis cuts are applied.

Cut	Data			MC		
	Events	$\epsilon_{rel}$ [%]	$\epsilon_{abs}$ [%]	Events	$\epsilon_{rel}$ [%]	$\epsilon_{abs}$ [%]
No Cuts	85309339	100.00	100.00	5008991	100.00	100.00
Prim. Vtx. with $\geq 3$ tracks	85269058	99.95	99.95	4975700	99.34	99.34
LAr noise bursts	85013877	99.70	99.65	4975700	100.00	99.34
$ \eta_e  < 2.47$	67801784	79.75	79.48	3306515	66.45	66.01
excl. $1.37 <  \eta_e  < 1.52$	58143952	85.76	68.16	2949192	89.19	58.88
excl. $1.6 <  \eta_e  < 1.7$	53601940	92.19	62.83	2718411	92.17	54.27
Author	52584223	98.10	61.64	2654134	97.64	52.99
$p_T > 20$ GeV	30443257	57.89	35.69	2154358	81.17	43.01
OQ Cut	30024713	98.63	35.20	2128280	98.79	42.49
IsEM Tight++	1021029	3.40	1.20	1181809	55.53	23.59
Di-Electron Trigger	993525	97.31	1.16	1156332	97.84	23.09

**Table 5.5:** A cut-flow showing the number of events passing each cut sequentially for data and Monte Carlo.  $\epsilon_{rel}$  is the efficiency relative to the previous cut in the sequence and  $\epsilon_{abs}$  is the efficiency relative to the total number of events before any analysis cuts are applied. Here the trigger cut is placed last to compare the efficiencies of offline and online cuts.

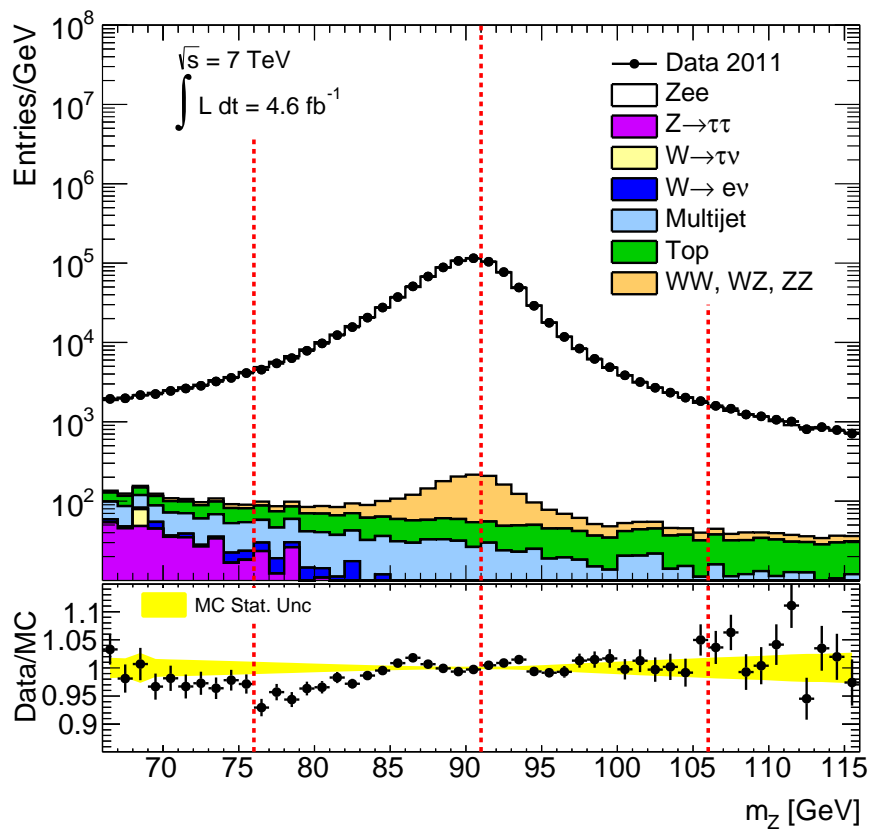


**Figure 5.1:** Invariant mass distribution in data and MC after the full event selection.

## 5.5 Electron Performance and Corrections

Monte Carlo simulation plays a fundamental role in the cross section measurement, in particular for the determination of reconstruction and selection efficiencies. Differences between the data and simulation need to be understood and accounted for. This is done by calculating and applying scale factors (SFs) to correct discrepancies. Each of these corrections introduce an associated systematic uncertainty that needs to be understood and propagated to the cross section measurement. Each stage of electron identification and reconstruction as described in Sec. 5.4 has an associated SF.

### 5.5.1 Scale Factors

The efficiency of reconstructing, triggering, and identifying an electron in ATLAS is central to the calculation of the associated SFs. The efficiency can be measured in data and also calculated in simulation, and to calculate SFs, both need to be performed.

The reconstruction efficiency,  $\epsilon_{reco}$ , is associated to the algorithm used to perform the reconstruction. It is the probability of reconstructing an electron with an electromagnetic calorimeter cluster deposit as an electron using the reconstruction algorithm.

The trigger efficiency,  $\epsilon_{trig}$ , is defined as the number of electrons selected that satisfy the trigger requirements divided by the total number of selected electrons. The efficiency is measured using the tag-and-probe method over  $Z \rightarrow ee$  events for both data and simulation. Efficiencies for the di-electron triggers are calculated as the product of efficiencies for each single electron.

The ID efficiency,  $\epsilon_{ID}$ , is the probability that a reconstructed electron satisfies one of the identification criteria described in Sec. 5.4.4.

The SF used to correct the simulation to the data is defined as:

$$SF_{reco,trig,ID} = \frac{\epsilon_{reco,trig,ID}^{data}}{\epsilon_{reco,trig,ID}^{MC}} \quad (5.5)$$

Each of the SFs is calculated in 2D bins of  $p_T$  and  $\eta$ , and has an associated systematic and statistical uncertainty component.

### 5.5.2 Electron Energy Scale and EM Calorimeter Calibration

The electron energy scale in data is corrected to that of Monte Carlo by calibration.

This calibration is necessary to precisely reconstruct the full energy of a detected electron. The  $Z \rightarrow ee$  process is used as it is well simulated and was measured at LEP with high precision. This makes it a good standard candle and a precise measurement is useful in many searches, such as  $H \rightarrow \gamma\gamma$ .

The *in-situ* calibration described here is part of a three-step process to fully calibrate the EM calorimeter [52].

- An electronic calibration is applied to convert the raw signal from each cell in the calorimeter into a deposited energy.
- An MC-based calibration is performed to correct for energy loss due to absorption in the passive material of the calorimeter as well as leakage outside the cluster.
- The *in-situ* calibration uses measured  $Z \rightarrow ee$  decays to intercalibrate the different calorimeter regions and determine the energy scale.

The mass of the di-electron system is:

$$m_{ee} = \sqrt{2E_1E_2(1 - \cos(\theta_{12}))} \quad (5.6)$$

where  $E_1$  and  $E_2$  are the energies of the electrons and  $\theta_{12}$  is the opening angle between them. These energies are measured after the MC-based calibration described above.

Official calibration factors are provided by the *e/gamma* combined performance group in ATLAS. The factors are calculated in bins ( $i$ ) of  $\eta$ , using the electron energy measured in data and Monte Carlo:

$$E_{data} = E_{MC}(1 + \alpha_i) \quad (5.7)$$

where  $\alpha$  is the energy scale correction applied to data to restore agreement with MC.

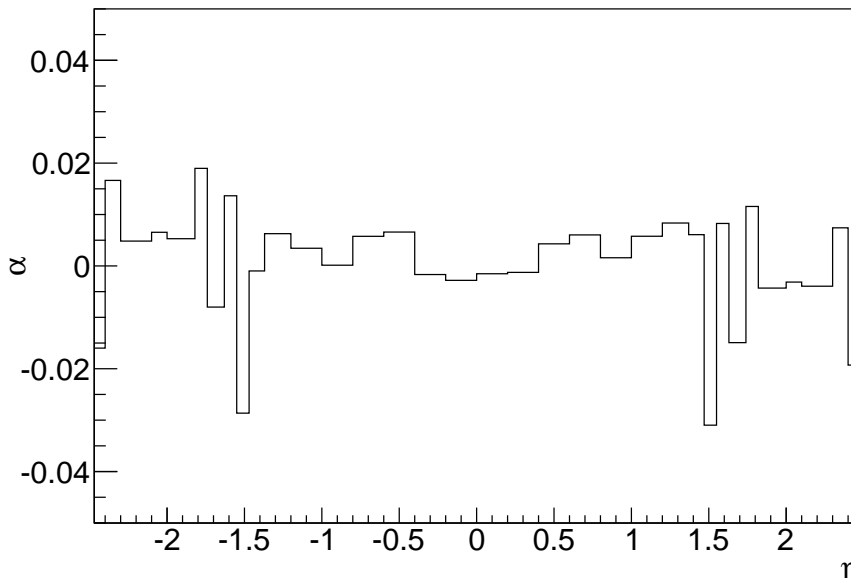


**Figure 5.2:** Electron energy scale calibration factors as a function of  $\eta$ .

Assuming the opening angle is known and neglecting second order terms, the effect on the di-electron mass is:

$$m_{ee}^{data} \simeq m_{ee}^{mc} \left( 1 + \frac{\alpha_{e1} + \alpha_{e2}}{2} \right) \quad (5.8)$$

### 5.5.3 Electron Energy Resolution

The energy resolution is corrected in MC to match the measured resolution in data. The resolution in the electromagnetic calorimeter is parametrised as [52]:

$$\frac{\sigma_E}{E} = \frac{a}{\sqrt{E}} \oplus \frac{b}{E} \oplus c \quad (5.9)$$

where  $a$  is called the *sampling term*,  $b$  is called the *noise term*, and  $c$  is called the *constant term*. Each of these parameters is  $\eta$ -dependent.

The noise description, is derived from calibration runs collecting real data. As can be seen from Eq. 5.9, the resolution at low energies (around the mass of the  $J/\psi$ ) is dominated by the first contribution – that from the sampling term  $a$ . The measured dielectron mass distribution from  $J/\psi \rightarrow e^+e^-$  decays is compared with MC simulation and found to be in good agreement [52]. Therefore the sampling term is assumed to be well described by simulation, and an effective constant term can be derived. This leads to a resolution correction of:

$$\sigma_{corr} = \sigma_{MC} \oplus c_{data} \times E \quad (5.10)$$

### 5.5.4 Energy scale studies to improve electron $\eta$ distribution

The distribution of the electron  $\eta$  in data and Monte Carlo shows a discrepancy that is particularly significant around  $|\eta| = 1.65 - 1.70$ . This discrepancy can be seen in Fig. 5.3, left, from the  $\eta$  distribution as seen in the  $Z \rightarrow ee$  analysis. It was seen in other studies, that the feature may be due to an effective efficiency loss of up to 30% in this narrow  $\eta$  strip [53].

Here a study was performed to see whether changing the energy scale in the binning of the scale factors would improve this distribution and the results are presented below.

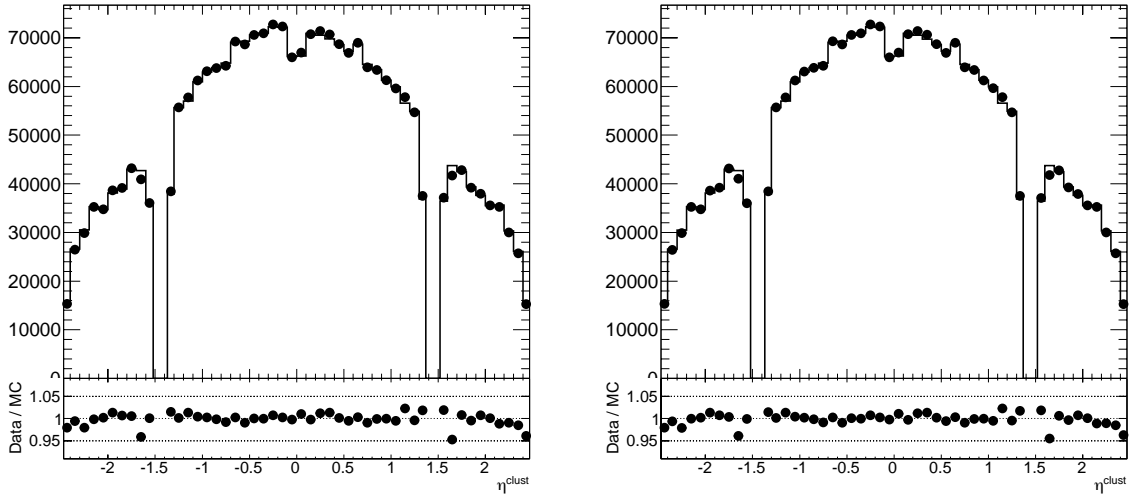


**Figure 5.3:**  $Z \rightarrow ee \eta$  distributions and ratio for data (black points) and MC (black histogram) for the standard calibration (left) and after applying extra calibration corrections in finer bins (right).

Comparing the measured electron energy from data with the true electron energy from MC makes it possible to calculate scale corrections to effectively provide an additional calibration of the electrons on top of the official energy scale calibration. The effect of applying these scale corrections to the data on the  $\eta$  distribution can then be investigated. The corrections are calculated in an  $\eta$  binning which matches that of the scale factors which are applied to MC. The calculation is shown in equation 5.11.

$$\alpha = \frac{E_{\text{clust.}}^{\text{meas.}}}{E_{\text{clust.}}^{\text{true}}} - 1 \quad (5.11)$$

These corrections are shown as a function of  $\eta$  in Fig. 5.4 left, with the binning of the official energy scale calibration overlaid as dashed lines for comparison. The  $\eta$  distribution after applying these scale corrections is shown in Fig. 5.3 right.

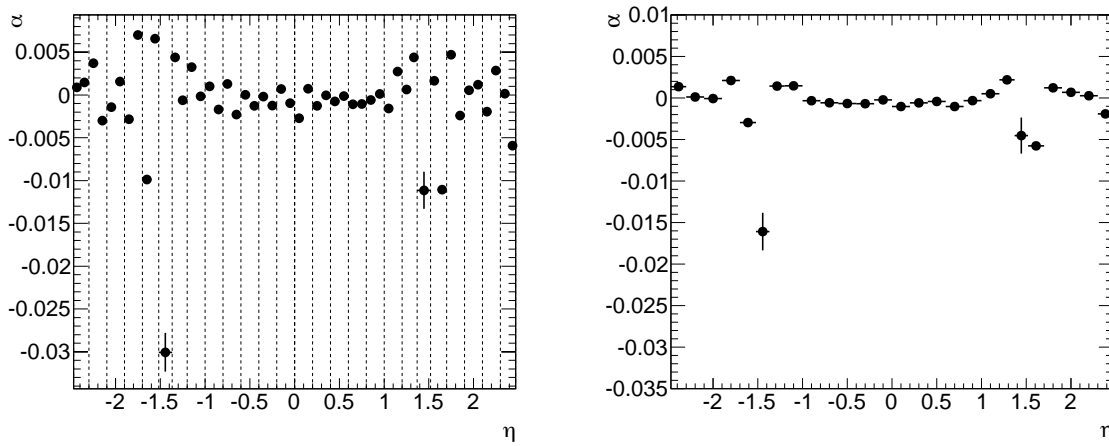


**Figure 5.4:** Left: Scale corrections (black points) in  $\eta$  bins of the scale factor obtained by comparing the  $Z \rightarrow ee$  peak position as reconstructed in data and MC. The dashed lines show the binning of the official energy scale calibration for comparison. Right: Validation of calibration procedure by computing extra scale corrections (black points) on top of the official energy scale calibration.

It is clear from Fig. 5.3 right, that the effect of applying these scale corrections has an almost insignificant effect on the  $\eta$  distribution. It can be concluded that an energy scale change is therefore not sufficient to fix this discrepancy.

To validate the method, the study was repeated with the same binning as the official energy scale calibration. As the data are therefore already corrected in this binning, any additional calibration factors should be very small, which is the case to  $\Delta\alpha \lesssim 0.002$ , as shown in Fig. 5.4 right.

For now the measure taken is to exclude the region  $1.60 < |\eta| < 1.70$  from all electron measurements and compensate by theory extrapolations for that.

## 5.6 MC Corrections

The simulated events in MC provide a good general description of the data collected but there are deviations which can be studied and corrected for. These are listed below.

### 5.6.1 Pileup Reweighting

The pileup effect describes the phenomenon of multiple interactions occurring in a collision. It is well simulated in MC but there remain differences between the simulation and collected data. These differences are corrected for by reweighting the MC using the number of average interactions per bunch crossing,  $\langle\mu\rangle$ .

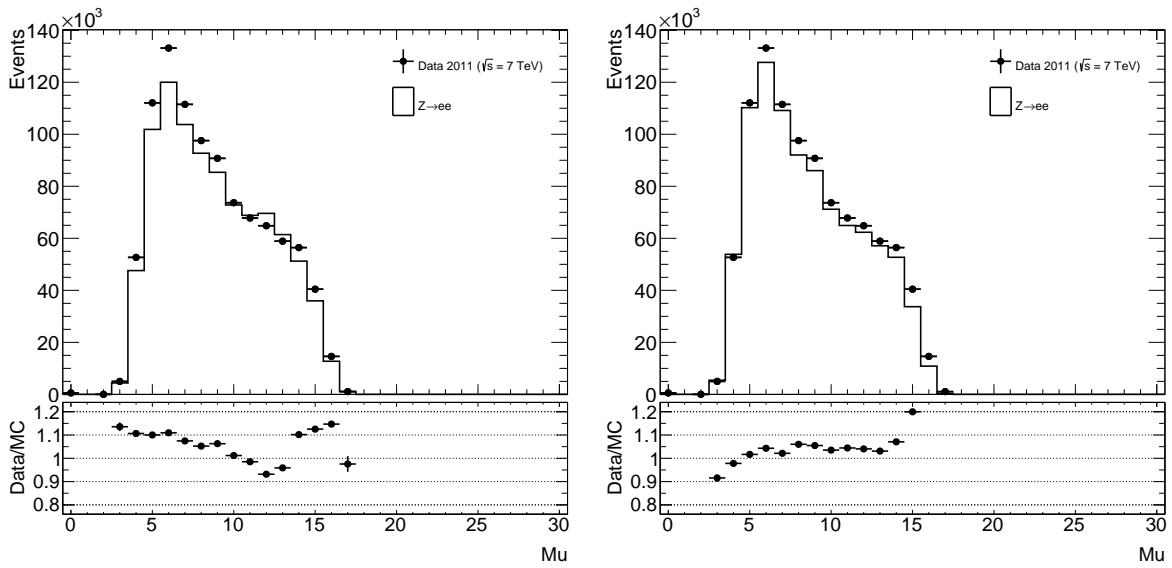


**Figure 5.5:** Average interactions per bunch crossing before (left) and after (right) pileup reweighting.

### 5.6.2 $Z$ Boson $p_T$ Reweighting

The boson  $p_T$  spectrum observed in data is not compatible with that produced in simulation. A separate analysis into the  $Z/\gamma^*p_T$  [54] studied the behaviour of the  $Z\phi^*$  quantity in several MC simulations. The  $\phi^*$  of the  $Z$  boson is highly correlated to its  $p_T$ . It was observed that the best description of this variable w.r.t. the data is produced by SHERPA and POWHEG PYTHIA8.

The boson  $p_T$  is therefore reweighted to POWHEG PYTHIA8 by default, and to SHERPA as a systematic variation.

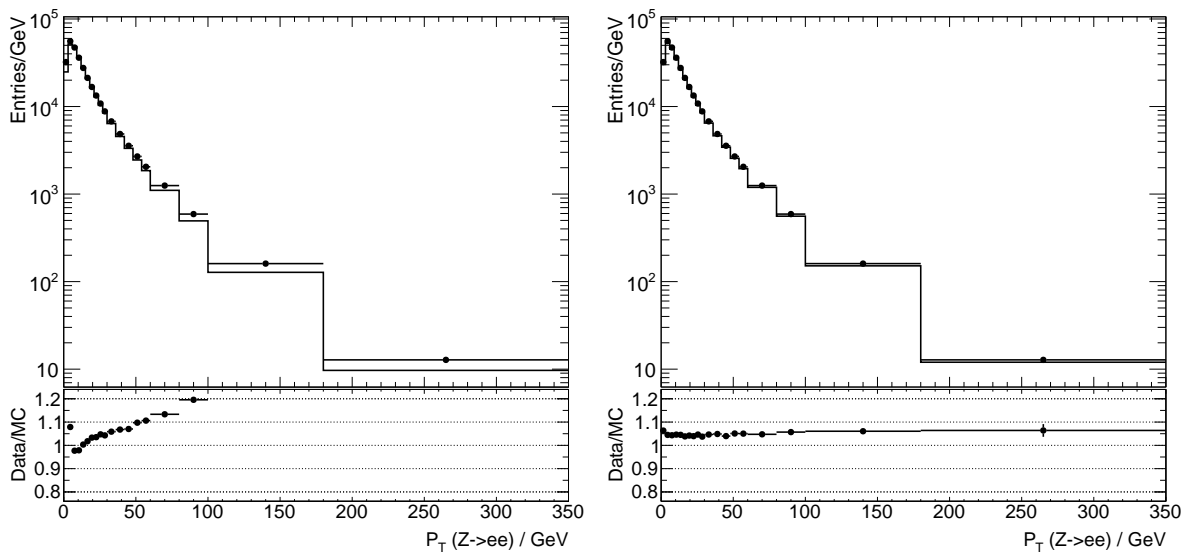


**Figure 5.6:**  $Z$  boson  $p_T$  before (left) and after (right)  $p_T$  reweighting.

### 5.6.3 Primary Vertex $z$ Reweighting

The shape of the luminous region, or *beam spot* in the detector is modelled differently in different MC samples. These can be *narrow* or *wide*, referring to the standard deviation of the Gaussian distribution of the  $z$  coordinate of the reconstructed primary vertex. The *wide beam spot* corresponds to  $\sigma_Z = 90\text{mm}$  and the *narrow beam spot* corresponds to  $\sigma_Z = 75\text{mm}$ . The distribution in data is much narrower than either, with  $\sigma_Z \approx 56\text{mm}$ .

It was found [55] that electron efficiencies were lower by several percent in the tails of this distribution and so a reweighting is applied to the simulation.

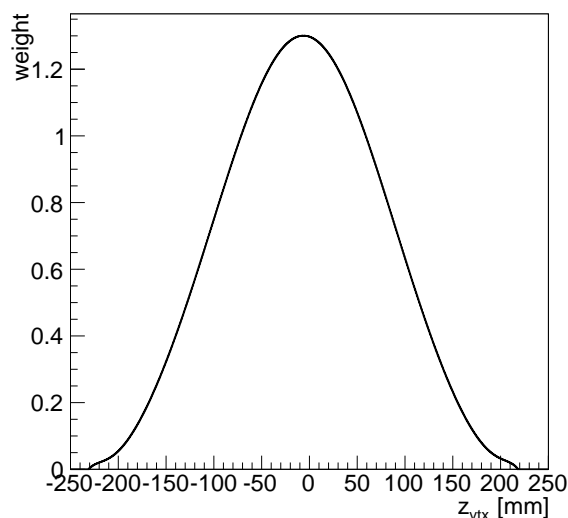


**Figure 5.7:** Weights applied to the simulation to correct the  $z$  position of the reconstructed primary vertex.

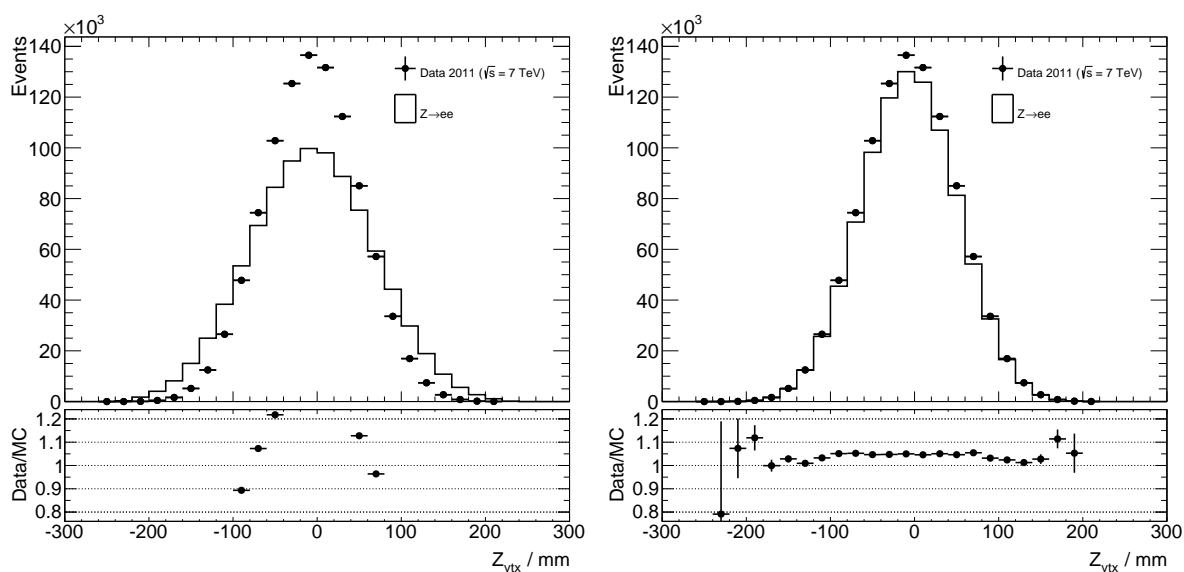


**Figure 5.8:**  $z$  position of primary vertex before (left) and after (right) vertex  $z$  reweighting.

#### 5.6.4 Z Lineshape Reweighting

The various MC generators described in Sec. 2.5 differ in the exact values of certain parameters used to produce the simulation. These parameters include the mass of the  $Z$  boson,  $m_Z$ , as well as its width,  $\Gamma_Z$ . The coupling constants also vary between the generators.

All MC samples are subsequently reweighted to an *Improved Born Approximation*.

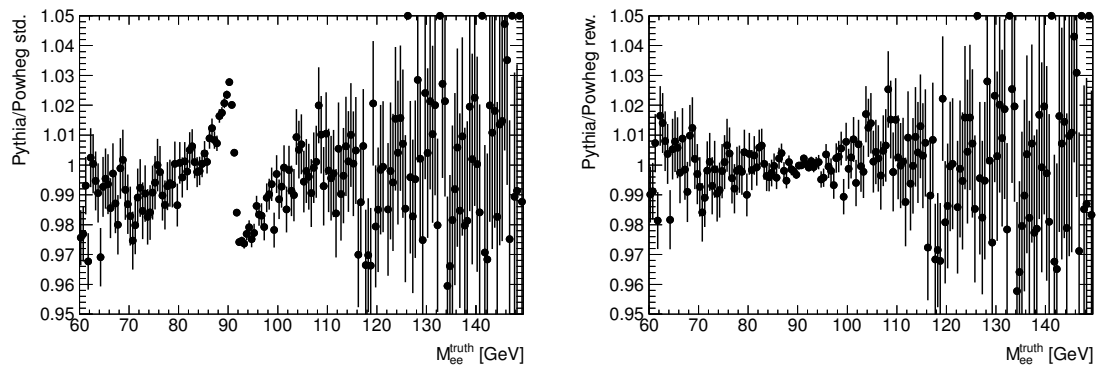


**Figure 5.9:** The line shape is shown before reweighting (left) and after reweighting (right).

## 5.7 Background Estimation

After the event selection described in Sec. 5.4.5 the background contribution to the  $Z \rightarrow ee$  sample is of the order of 0.3%. Individual background contributions from different processes are estimated using a combination of Monte Carlo simulation and data-driven techniques.

QCD processes contribute to the background primarily as jets faking electrons that pass the kinematic signal selection, but there are also contributions from semi-leptonic heavy-flavour decays, Dalitz decays, and photon conversion.

### 5.7.1 $t\bar{t}$ and Electroweak Backgrounds

Background contributions from  $t\bar{t}$  and electroweak (EW) processes are estimated by Monte Carlo simulation. The simulated processes are:

- $W \rightarrow e\nu$
- $W \rightarrow \tau\nu$
- $Z \rightarrow \tau\tau$
- $t\bar{t}$
- WW
- WZ
- ZZ

The  $W \rightarrow \ell\nu$  and  $Z \rightarrow \ell\ell$  samples are normalised to the NNLO cross sections computed using the FEWZ program [21]. The associated uncertainties are of the order of 5% as discussed in Sec. 5.2.

The  $t\bar{t}$  cross section is taken from Refs. [56–58], and calculated for a top quark mass of  $m_t = 172.5$  GeV, with an asymmetric uncertainty on the cross section of (+7, −10)%.

The WW, WZ, and ZZ diboson samples are all normalised with an uncertainty of 7%.

Process	$\sigma \cdot \text{BR} \cdot \epsilon_{filter}$ [nb]	Generator
$W \rightarrow e\nu$	10.460 (5%)	PYTHIA6
$W \rightarrow \tau\nu$	10.460 (5%)	PYTHIA6
$Z/\gamma^* \rightarrow \tau\tau$ ( $m_{\tau\tau} > 60$ GeV)	0.990 (5%)	PYTHIA6
$t\bar{t}$	$0.165^{(+7\%)}_{(-10\%)} \cdot 0.555$	MC@ NLO
WW	$44.9 \cdot 0.389 \cdot 10^{-3}$ (7%)	HERWIG
WZ	$18.5 \cdot 0.310 \cdot 10^{-3}$ (7%)	HERWIG
ZZ	$6.02 \cdot 0.212 \cdot 10^{-3}$ (7%)	HERWIG

**Table 5.6:** Background processes with their associated cross sections and uncertainties. The quoted cross sections are used to normalise estimates of expected number of events.

### 5.7.2 Multi-jet Background Estimation

Due to the large theoretical uncertainties and high statistics needed, it is impractical to estimate the multi-jet background from simulation. Instead, a data-driven method is used. This is performed using a template selection, whereby a selection is applied to produce a background-enhanced sample of events in data, subtracting any signal contributions, and then normalising the enhanced selection to the signal selection.

The template is defined in the same kinematic region as the signal selection as this defines the phase space where fake electrons are present as background. The background-enhanced sample is selected by reversing some electron ID criteria.

The normalisation of the template relies on the assumption that jets misidentified as electrons aren't very isolated, in contrast to signal electrons which are. The tail of the isolation distribution in the signal selection is therefore assumed to be background-dominated, and so the template selection is scaled such that the number of events in its tail is equal to the number of events in the tail of the signal selection after subtraction of events from the signal and background MC samples.

### 5.7.3 Estimation Method

A study was performed to determine an appropriate template selection [59]. Both electrons are required to pass the *loose* electron ID requirement, but fail one of the *medium* criteria. Events are selected that pass a di-photon trigger,  $EF\_2g20\_loose$ , which requires two photon candidates with  $p_T > 20$  GeV, and additionally applies the *loose* ID selection.

The isolation distribution used to normalise the template is  $E_T\text{Cone30}/E_T$ . The simulation of this distribution in MC models the shape of the data well, but with a shift of approximately 0.4 GeV as shown in Fig. 5.10. The MC distribution used in the normalisation of the multi-jet background estimation is therefore shifted to match the data.

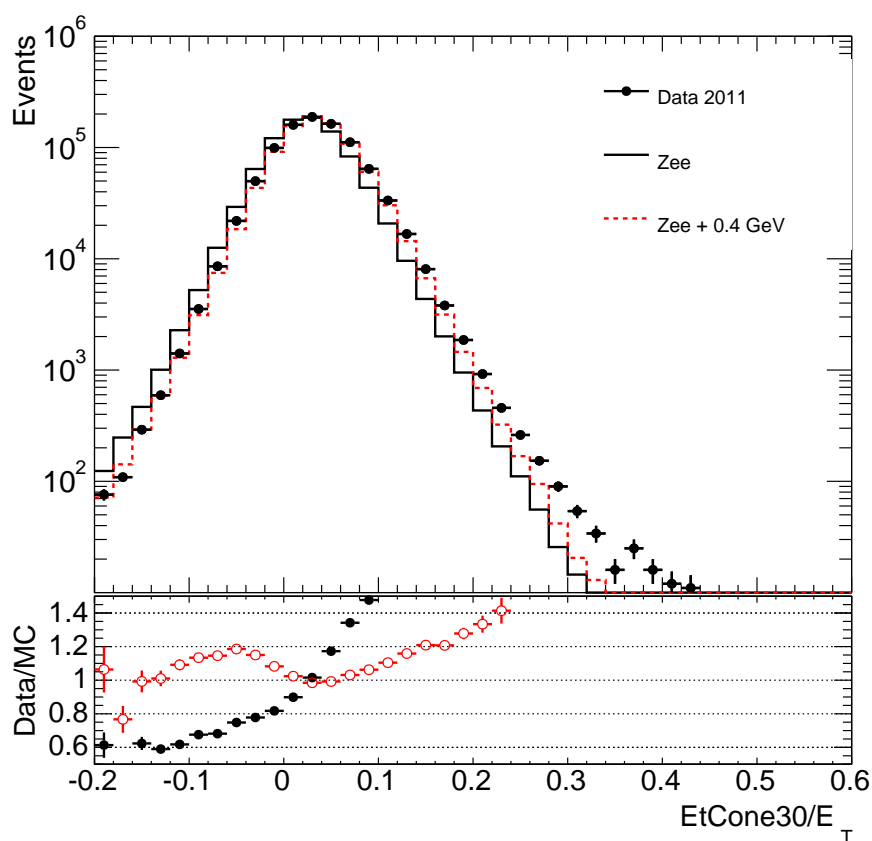


**Figure 5.10:**  $E_{T\text{Cone30}}/E_T$  in data and signal MC, illustrating the 0.4 GeV shift in the MC distribution to match the data.

The normalisation range is chosen such that the left edge is at the point where the total number of events in data from that point to the end of the distribution is at least twice the number of events in the same region in MC. The right edge of the range is set at 0.6.

The left edge of the normalisation range in each mass bin is shown in table Tab. 5.7 along with the factor calculated to normalise the tail of the isolation distribution in the template selection to the tail of the isolation distribution in the signal selection.

$M_Z$ [ GeV ]	$E_T\text{Cone30}/E_T$	Normalisation Factor
66 – 76	0.28	0.0038
76 – 91	0.36	0.0027
91 – 106	0.32	0.0023
106 – 116	0.20	0.0026

**Table 5.7:** The left edge of the normalisation range in each mass bin, and the factor calculated to normalise the tail of the isolation distribution.

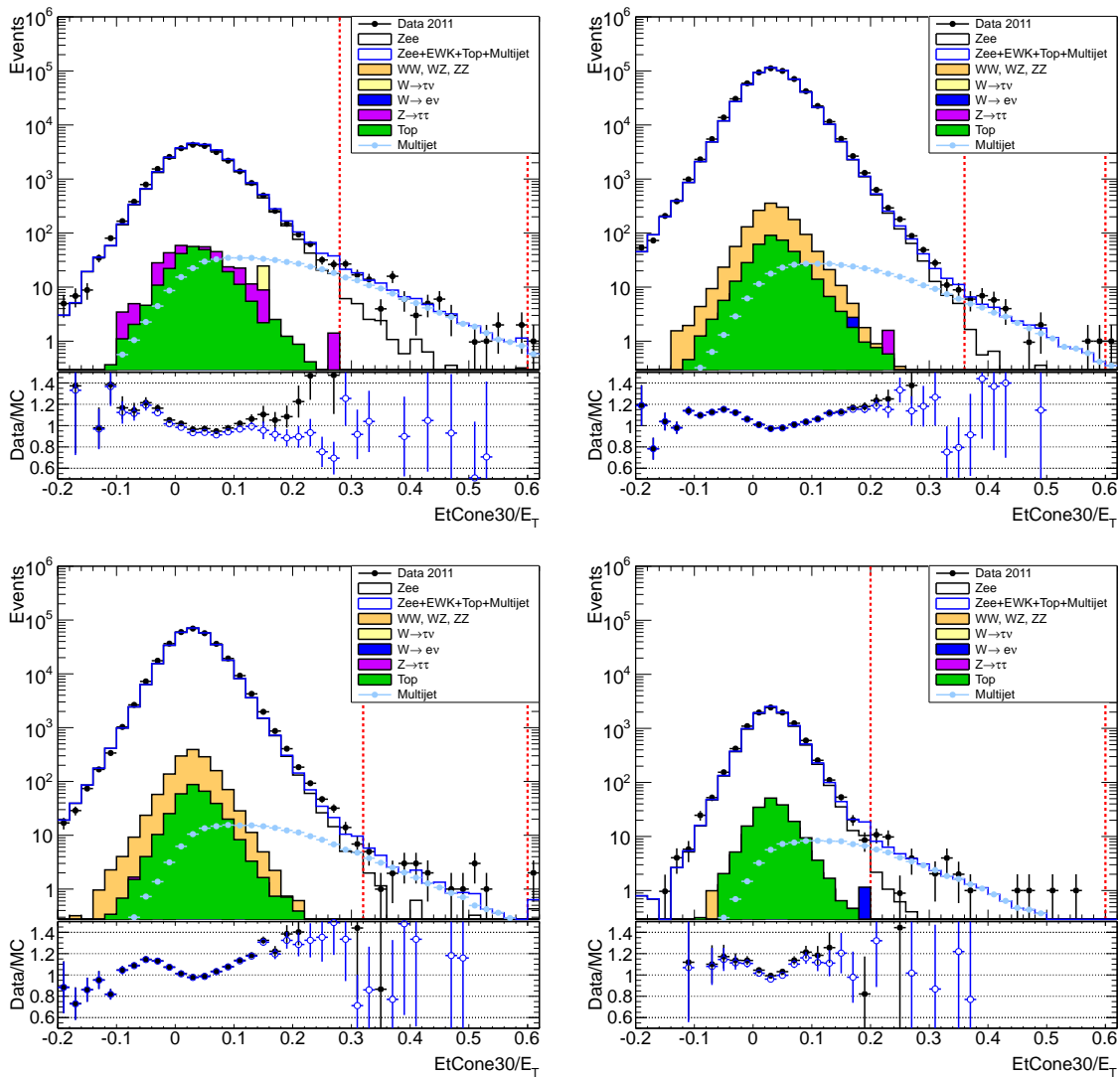


**Figure 5.11:** Plots showing the  $E_T\text{Cone30}/E_T$  distribution for data, MC, and background samples in each measurement mass bin. Top left:  $66 < m_Z < 76$  GeV, top right:  $76 < m_Z < 91$  GeV, bottom left:  $91 < m_Z < 106$  GeV, bottom right:  $106 < m_Z < 116$  GeV. The distribution for the multi-jet template selection is shown after normalisation. The ratio of data to MC with and without electroweak,  $t\bar{t}$ , and multi-jet contributions is shown. The range of the normalisation is indicated by the dashed red lines.

#### 5.7.4 Systematic Uncertainty from the Multi-jet Background Estimation

Use of a template selection for the multi-jet background estimation introduces a potential bias as a result of the template choice. In addition, the choice of region of the isolation distribution used to normalise the template introduces an uncertainty.

The systematic uncertainty from this is estimated by repeating the normalisation procedure  $i = 10$  times, varying the range of the tail used to perform the normalisation. The range is separated into two halves, and the left edge is shifted in increments in the left half. The right edge of the range remains fixed. For iteration  $i$ , left edge  $L$ , and right edge  $R$ :

$$L_i = L + \frac{R - L}{20} \cdot i \quad (5.12)$$

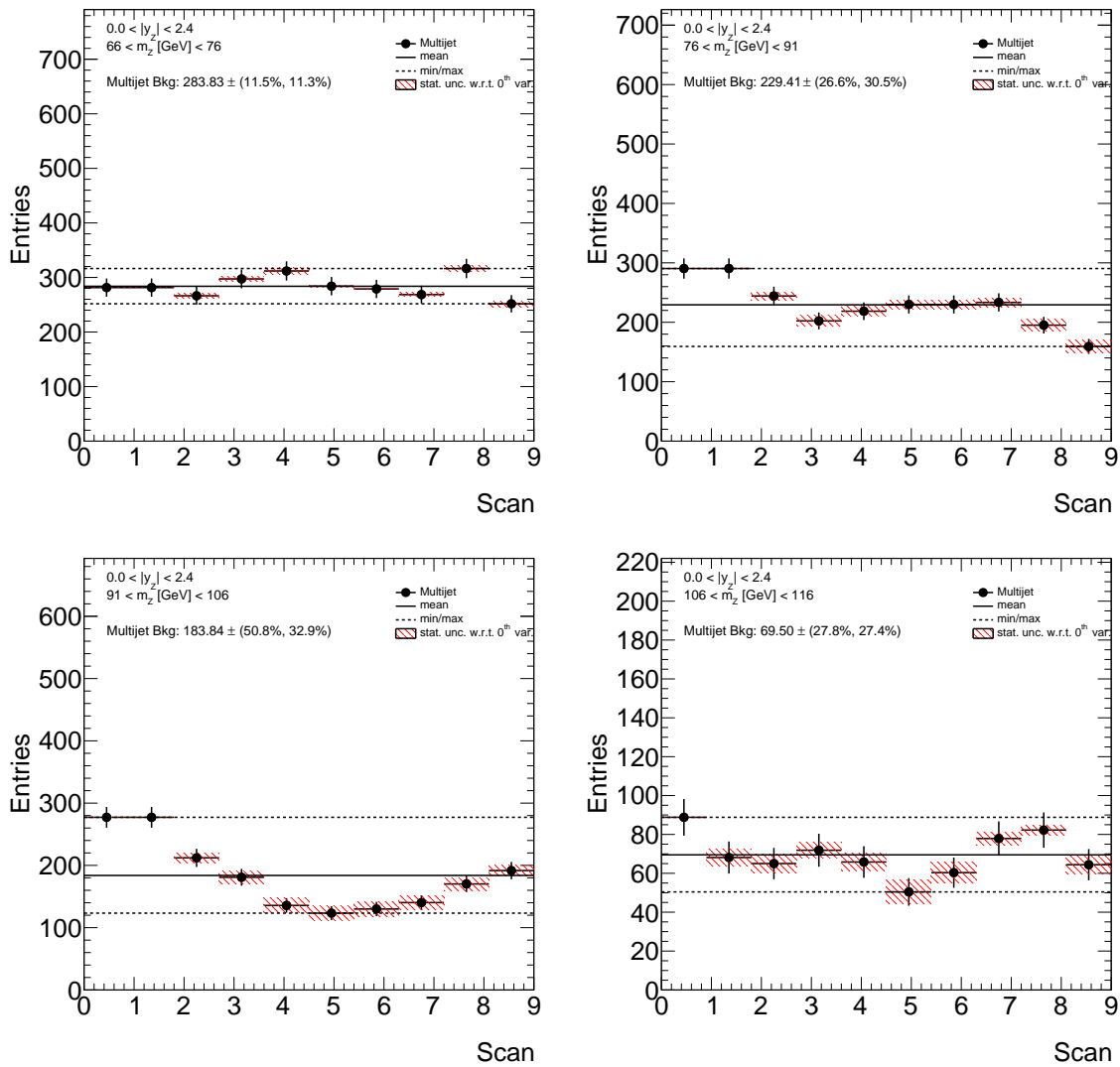


**Figure 5.12:** Plots showing the number of multi-jet events for each iteration of the scan of the isolation variable normalisation region. The mean is shown as a solid line and the minimum and maximum are indicated by dashed lines. Top left:  $66 < m_Z < 76$  GeV, top right:  $76 < m_Z < 91$  GeV, bottom left:  $91 < m_Z < 106$  GeV, bottom right:  $106 < m_Z < 116$  GeV.

i	L	n	$\frac{s}{n}$ %	$\frac{b}{n}$ %	t	$\frac{s}{t}$ %	$\frac{b}{t}$ %
0	0.22	231	44	0.85	3061	3.30	0.06
1	0.24	231	44	0.85	3061	3.30	0.06
2	0.26	168	37	0.8	2661	2.31	0.05
3	0.28	136	27	0.84	2225	1.65	0.05
4	0.3	108	19	0.79	1869	1.10	0.05
5	0.32	81	17	0.82	1582	0.86	0.04
6	0.34	64	14	0.79	1320	0.67	0.04
7	0.36	50	12	0.82	1098	0.53	0.04
8	0.38	46	7.9	0.64	895	0.41	0.03
9	0.4	30	8.3	0.86	729	0.34	0.04

**Table 5.8:** The left edge of the normalisation region,  $L$ , number of events in the tail of the data distribution,  $n$ , fractional percentage of signal ( $\frac{s}{n}$ ) and background ( $\frac{b}{n}$ ) events in measurement bin  $66 < m_Z[GeV] < 76$  for iteration  $i$  of the scan of the normalisation region. The number of events in the tail of the template selection,  $t$ , as well as the fractional percentage of signal ( $\frac{s}{t}$ ) and background ( $\frac{b}{t}$ ) events is also shown.

i	L	n	$\frac{s}{n}$ %	$\frac{b}{n}$ %	t	$\frac{s}{t}$ %	$\frac{b}{t}$ %
0	0.28	126	45	0.62	1629	3.45	0.05
1	0.3	126	45	0.62	1629	3.45	0.05
2	0.31	77	36	0.84	1367	2.02	0.05
3	0.33	49	32	1.1	1114	1.40	0.05
4	0.35	38	21	1.1	931	0.85	0.04
5	0.36	29	13	1.1	746	0.49	0.04
6	0.38	29	13	1.1	746	0.49	0.04
7	0.4	23	11	1.3	592	0.43	0.05
8	0.41	16	13	1.2	481	0.44	0.04
9	0.43	10	12	0.83	375	0.32	0.02

**Table 5.9:** The left edge of the normalisation region,  $L$ , number of events in the tail of the data distribution,  $n$ , fractional percentage of signal ( $\frac{s}{n}$ ) and background ( $\frac{b}{n}$ ) events in measurement bin  $76 < m_Z[GeV] < 91$  for iteration  $i$  of the scan of the normalisation region. The number of events in the tail of the template selection,  $t$ , as well as the fractional percentage of signal ( $\frac{s}{t}$ ) and background ( $\frac{b}{t}$ ) events is also shown.

i	L	n	$\frac{s}{n}$ %	$\frac{b}{n}$ %	t	$\frac{s}{t}$ %	$\frac{b}{t}$ %
0	0.22	217	49	0.49	1604	6.70	0.07
1	0.24	217	49	0.49	1604	6.70	0.07
2	0.26	124	43	0.5	1356	3.92	0.05
3	0.28	77	36	0.63	1112	2.47	0.04
4	0.3	45	31	0.71	931	1.49	0.03
5	0.32	31	24	1	768	0.98	0.04
6	0.34	24	16	0.37	631	0.62	0.01
7	0.36	19	8.5	0.46	505	0.32	0.02
8	0.38	18	4.1	0.35	414	0.18	0.02
9	0.4	16	4.6	0.064	326	0.23	0.00

**Table 5.10:** The left edge of the normalisation region,  $L$ , number of events in the tail of the data distribution,  $n$ , fractional percentage of signal ( $\frac{s}{n}$ ) and background ( $\frac{b}{n}$ ) events in measurement bin  $91 < m_Z[GeV] < 106$  for iteration  $i$  of the scan of the normalisation region. The number of events in the tail of the template selection,  $t$ , as well as the fractional percentage of signal ( $\frac{s}{t}$ ) and background ( $\frac{b}{t}$ ) events is also shown.

i	L	n	$\frac{s}{n}$ %	$\frac{b}{n}$ %	t	$\frac{s}{t}$ %	$\frac{b}{t}$ %
0	0.14	124	49	1.7	1301	4.62	0.16
1	0.16	70	39	2	1142	2.37	0.12
2	0.19	49	28	1.6	997	1.36	0.08
3	0.21	39	13	1.9	863	0.59	0.08
4	0.23	28	7.1	1.6	727	0.27	0.06
5	0.26	18	8.7	0.87	604	0.26	0.03
6	0.28	13	0	0.26	402	0.00	0.01
7	0.3	13	0	-0.25	313	0.00	-0.01
8	0.33	11	0	0.083	250	0.00	0.00
9	0.35	7	0	0.13	203	0.00	0.00

**Table 5.11:** The left edge of the normalisation region,  $L$ , number of events in the tail of the data distribution,  $n$ , fractional percentage of signal ( $\frac{s}{n}$ ) and background ( $\frac{b}{n}$ ) events in measurement bin  $106 < m_Z[GeV] < 116$  for iteration  $i$  of the scan of the normalisation region. The number of events in the tail of the template selection,  $t$ , as well as the fractional percentage of signal ( $\frac{s}{t}$ ) and background ( $\frac{b}{t}$ ) events is also shown.

## 6 Unfolding

Technical limitations prevent perfectly measured distributions from being obtained, and so the measured distributions must be corrected to obtain an estimation of the true underlying distribution. This is called *unfolding* and requires detailed simulations and a precise knowledge of the detector and its limitations.

The method chosen to perform the unfolding is informed by how well the simulation describes the data, as well as how many events migrate from one measurement bin to another. Migrations are measured by the purity and stability of the choice of measurement binning. This is described below in Sec. 6.2. The two unfolding methods used in ATLAS are *bin-by-bin* and iterative *Bayesian* unfolding [60].

Bin-by-bin unfolding consists of using simulation to calculate a correction factor in each bin that is then applied to the data.

For bin  $i$ :

$$C_i = \frac{T_i}{R_i} \quad (6.1)$$

where

- $T_i$  is the number of generated events in bin  $i$  with no event selection applied
- $R_i$  is the number of reconstructed MC events in bin  $i$  after event selection
- $C_i$  is the correction factor to be applied to the data

such that the unfolded value,  $U_i = Data_i \cdot C_i$  is obtained. The unfolded spectrum  $U$  should then closely describe the truth spectrum  $T$  that would be measured in a perfect detector.

This method ignores correlations between bins and suffers from limitations imposed by finite MC statistics as well as the accuracy of the simulation. This also relies on a very precise description of the detector in simulation. These factors are propagated as systematic uncertainties when performing bin-by-bin unfolding.

Bayesian unfolding relies on inferences made to link observed measurable quantities to true physical values using probability theory. The procedure can be reduced to quantifying causes and effects, where a cause  $C$  corresponds to the true quantity and an effect  $E$  corresponds to a smeared, measured value. The probability  $P(E_j|C_i)$  that an effect is produced by a cause can be estimated assuming some knowledge of the smearing from resolution, migration, and efficiency usually obtained using Monte Carlo. To perform the unfolding, the probability  $P(C_i|E_j)$  that a cause is responsible for an observed effect can be estimated using Bayes' theorem [61].

$$P(C_i|E_j) = \frac{P(E_j|C_i) \cdot P_0(C_i)}{\sum_{l=1}^{n_c} P(E_j|C_l) \cdot P_0(C_l)} \quad (6.2)$$

$$\hat{n}(C_i) = \frac{1}{\epsilon_i} \sum_{j=1}^{n_E} n(E_j) \cdot P(C_i|E_j) \quad \epsilon_i \neq 0, \quad (6.3)$$

where  $\hat{n}(C_i)$  is the expected number of events in cause bin  $i$ ,  $n(E_j)$  is the number of events in the effect bin  $j$ ,  $P_0(C_i)$  the initial probabilities, and  $\epsilon_i$  is the efficiency with which cause  $i$  has an effect.

## 6.1 Fiducial Measurement

The nominal measurement in this analysis is of the differential  $d\sigma/dm_{\ell\ell}$   $Z \rightarrow ee$  cross section in four bins of the di-lepton invariant mass:  $m_{\ell\ell} = 66 - 76 - 91 - 106 - 116$  GeV. This measurement is combined with the measurement of the  $Z \rightarrow \mu\mu$  cross section in the same mass bins. In addition, the following measured cross sections are combined:

- $W \rightarrow e\nu$  and  $W \rightarrow \mu\nu$ 
  - $d\sigma/d|\eta_e|$
  - $d\sigma/d|\eta_\mu| dp_{T,e}$
- $Z \rightarrow ee$  and  $Z \rightarrow \mu\mu$ 
  - $d\sigma/d|y_{\ell\ell}|$
  - $d\sigma/d|y_{\ell\ell}|dm_{\ell\ell}$

To perform the combination, each measurement must be extrapolated to a common fiducial volume. The experimental phase space for the  $Z \rightarrow \ell\ell$  measurements is described in Tab.6.1. The  $W \rightarrow \ell\nu$  experimental phase space as well as the common fiducial regions used for the combination of the different data sets is described in Tabs C.1– C.2.

Central $Z \rightarrow ee$ Experimental Phase Space									
Integrated	<ul style="list-style-type: none"> <li>• Both <math>p_{T,\ell} &gt; 20</math> GeV</li> <li>• Both <math> \eta  &lt; 2.47</math> excluding <math>1.37 &lt;  \eta  &lt; 1.52</math></li> <li>• Additionally excluding <math>1.6 &lt;  \eta  &lt; 1.7</math></li> <li>• 1 + 4 mass bins: <ul style="list-style-type: none"> <li>– <math>m_{\ell\ell} = 66 - 116</math> GeV</li> <li>– <math>m_{\ell\ell} = 66 - 76 - 91 - 106 - 116</math> GeV</li> </ul> </li> </ul>								
Differential	<ul style="list-style-type: none"> <li>• Both <math>p_{T,\ell} &gt; 20</math> GeV</li> <li>• Both <math> \eta  &lt; 2.47</math> excluding <math>1.37 &lt;  \eta  &lt; 1.52</math></li> <li>• Additionally excluding <math>1.6 &lt;  \eta  &lt; 1.7</math></li> <li>• <math>d\sigma/d y_{\ell\ell} dm_{\ell\ell}</math>: <table border="1"> <thead> <tr> <th><math>m_{\ell\ell}</math> [ GeV ]</th> <th><math> y_{\ell\ell} </math></th> </tr> </thead> <tbody> <tr> <td>46–66</td> <td>0, 0.4, 0.8, 1.2, 1.6, 2.0, 2.4</td> </tr> <tr> <td>66–116</td> <td>0, 0.2, 0.4, 0.6, 0.8, 1.0, 1.2, 1.4, 1.6, 1.8, 2.0, 2.2, 2.4</td> </tr> <tr> <td>116–150</td> <td>0, 0.4, 0.8, 1.2, 1.6, 2.0, 2.4</td> </tr> </tbody> </table> </li> </ul>	$m_{\ell\ell}$ [ GeV ]	$ y_{\ell\ell} $	46–66	0, 0.4, 0.8, 1.2, 1.6, 2.0, 2.4	66–116	0, 0.2, 0.4, 0.6, 0.8, 1.0, 1.2, 1.4, 1.6, 1.8, 2.0, 2.2, 2.4	116–150	0, 0.4, 0.8, 1.2, 1.6, 2.0, 2.4
$m_{\ell\ell}$ [ GeV ]	$ y_{\ell\ell} $								
46–66	0, 0.4, 0.8, 1.2, 1.6, 2.0, 2.4								
66–116	0, 0.2, 0.4, 0.6, 0.8, 1.0, 1.2, 1.4, 1.6, 1.8, 2.0, 2.2, 2.4								
116–150	0, 0.4, 0.8, 1.2, 1.6, 2.0, 2.4								
Forward $Z \rightarrow ee$ Experimental Phase Space									
Integrated	<ul style="list-style-type: none"> <li>• One electron with <math>p_{T,\ell} &gt; 23</math> GeV and <math> \eta  &lt; 2.47</math> excluding <math>1.37 &lt;  \eta  &lt; 1.52</math></li> <li>• Additionally excluding <math>1.6 &lt;  \eta  &lt; 1.7</math> on the central electron</li> <li>• Other electron with <math>p_{T,\ell} &gt; 20</math> GeV and <math>2.5 &lt;  \eta  &lt; 4.9</math> excluding <math>3.16 &lt;  \eta  &lt; 3.35</math></li> <li>• 2 mass bins: <ul style="list-style-type: none"> <li>– <math>m_{\ell\ell} = 66 - 116 - 150</math> GeV</li> </ul> </li> </ul>								
Differential	<ul style="list-style-type: none"> <li>• One electron with <math>p_{T,\ell} &gt; 23</math> GeV and <math> \eta  &lt; 2.47</math> excluding <math>1.37 &lt;  \eta  &lt; 1.52</math></li> <li>• Additionally excluding <math>1.6 &lt;  \eta  &lt; 1.7</math> on the central electron</li> <li>• Other electron with <math>p_{T,\ell} &gt; 20</math> GeV and <math>2.5 &lt;  \eta  &lt; 4.9</math> excluding <math>3.16 &lt;  \eta  &lt; 3.35</math></li> <li>• <math>d\sigma/d y_{\ell\ell} dm_{\ell\ell}</math>: <table border="1"> <thead> <tr> <th><math>m_{\ell\ell}</math> [ GeV ]</th> <th><math> y_{\ell\ell} </math></th> </tr> </thead> <tbody> <tr> <td>66–116</td> <td>1.2, 1.4, 1.6, 1.8, 2.0, 2.2, 2.4, 2.8, 3.2, 3.6</td> </tr> <tr> <td>116–150</td> <td>1.2, 1.6, 2.0, 2.4, 2.8, 3.2, 3.6</td> </tr> </tbody> </table> </li> </ul>	$m_{\ell\ell}$ [ GeV ]	$ y_{\ell\ell} $	66–116	1.2, 1.4, 1.6, 1.8, 2.0, 2.2, 2.4, 2.8, 3.2, 3.6	116–150	1.2, 1.6, 2.0, 2.4, 2.8, 3.2, 3.6		
$m_{\ell\ell}$ [ GeV ]	$ y_{\ell\ell} $								
66–116	1.2, 1.4, 1.6, 1.8, 2.0, 2.2, 2.4, 2.8, 3.2, 3.6								
116–150	1.2, 1.6, 2.0, 2.4, 2.8, 3.2, 3.6								
$Z \rightarrow \mu\mu$ Experimental Phase Space									
Integrated	<ul style="list-style-type: none"> <li>• Both <math>p_{T,\ell} &gt; 20</math> GeV</li> <li>• Both <math> \eta  &lt; 2.4</math></li> <li>• 1 + 4 mass bins: <ul style="list-style-type: none"> <li>– <math>m_{\ell\ell} = 66 - 116</math> GeV</li> <li>– <math>m_{\ell\ell} = 66 - 76 - 91 - 106 - 116</math> GeV</li> </ul> </li> </ul>								
Differential	<ul style="list-style-type: none"> <li>• Both <math>p_{T,\ell} &gt; 20</math> GeV</li> <li>• Both <math> \eta  &lt; 2.4</math></li> <li>• <math>d\sigma/d y_{\ell\ell} dm_{\ell\ell}</math>: <table border="1"> <thead> <tr> <th><math>m_{\ell\ell}</math> [ GeV ]</th> <th><math> y_{\ell\ell} </math></th> </tr> </thead> <tbody> <tr> <td>46–66</td> <td>0, 0.4, 0.8, 1.2, 1.6, 2.0, 2.4</td> </tr> <tr> <td>66–116</td> <td>0, 0.2, 0.4, 0.6, 0.8, 1.0, 1.2, 1.4, 1.6, 1.8, 2.0, 2.2, 2.4</td> </tr> <tr> <td>116–150</td> <td>0, 0.4, 0.8, 1.2, 1.6, 2.0, 2.4</td> </tr> </tbody> </table> </li> </ul>	$m_{\ell\ell}$ [ GeV ]	$ y_{\ell\ell} $	46–66	0, 0.4, 0.8, 1.2, 1.6, 2.0, 2.4	66–116	0, 0.2, 0.4, 0.6, 0.8, 1.0, 1.2, 1.4, 1.6, 1.8, 2.0, 2.2, 2.4	116–150	0, 0.4, 0.8, 1.2, 1.6, 2.0, 2.4
$m_{\ell\ell}$ [ GeV ]	$ y_{\ell\ell} $								
46–66	0, 0.4, 0.8, 1.2, 1.6, 2.0, 2.4								
66–116	0, 0.2, 0.4, 0.6, 0.8, 1.0, 1.2, 1.4, 1.6, 1.8, 2.0, 2.2, 2.4								
116–150	0, 0.4, 0.8, 1.2, 1.6, 2.0, 2.4								

**Table 6.1:** Complete list of experimental measurements considered in the  $Z \rightarrow ee$  and  $Z \rightarrow \mu\mu$  channels.

## 6.2 Purity and Stability

The purity,  $P^i$ , and stability,  $S^i$ , in each bin are defined as:

$$P^i = \frac{N_{\text{rec\&gen, all reco cuts}}^i}{N_{\text{rec, all reco cuts}}^i}, \quad S^i = \frac{N_{\text{rec\&gen, all reco cuts}}^i}{N_{\text{gen, all reco cuts}}^i}, \quad (6.4)$$

where

- $N_{\text{rec, all reco cuts}}^i$  — is the sum of event weights reconstructed in bin  $i$ ,
- $N_{\text{gen, all reco cuts}}^i$  — is the sum of event weights generated in bin  $i$ ,
- $N_{\text{rec\&gen, all reco cuts}}^i$  — is the sum of event weights which were generated and reconstructed in bin  $i$ .

Purity is a measure of migrations into the bin, i.e. the fraction of events reconstructed in the bin that were also generated in the bin, while stability measures migrations out of the bin, i.e. the fraction of events generated in the bin that are also reconstructed in the bin.

The purity in each bin of a measurement is a useful quantity to motivate the choice of unfolding technique. If the purity is above  $\sim 0.8$ , then bin-by-bin unfolding can be considered. Otherwise an iterative method is preferred as this corrects for potential biases from a difference in shape between data and simulation caused by bin migrations. However an iterative procedure introduces bin correlations and this increases the statistical uncertainty.

Purity and stability can also be used to validate the binning used for the differential measurement. Purity below 0.5 would indicate significant migrations and a new approach to the measurement should be considered.

The purity and stability as a function of the di-electron invariant mass can be seen in Fig. 6.1. The mass bins 91–106 GeV and 106–116 GeV show migrations of around 20%, while the bins 66–76 GeV and 76–91 GeV show migrations of around 40–50%.

These are high enough to consider an iterative approach, and a comparison of bin-by-bin unfolding with ten iterations of Bayesian unfolding is shown in Fig. 6.2.

After three iterations of Bayesian unfolding, the difference in the unfolded spectrum compared to a bin-by-bin approach is negligible, while there is also no significant increase in the statistical uncertainty w.r.t. to the bin-by-bin method. The iterative Bayesian unfolding with three iterations is therefore used for the cross section measurement.

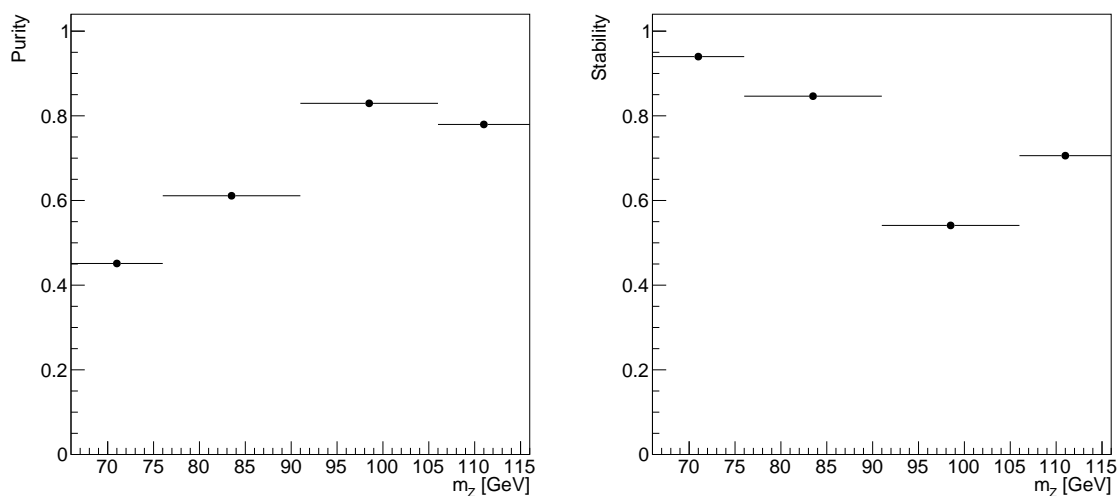


**Figure 6.1:** Purity (left) and stability (right) measured in bins of di-electron invariant mass.

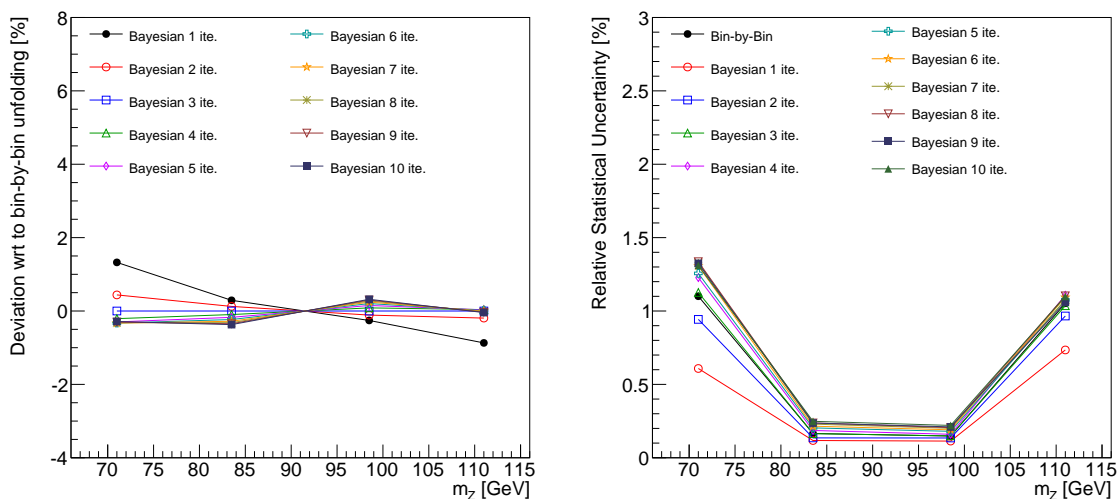


**Figure 6.2:** Deviation in percent with respect to bin-by-bin unfolding of the Bayesian-unfolded distribution for ten iterations (left) and the statistical uncertainty for different unfolding options (right).

## 7 Systematic Uncertainties on the Cross Section Measurement

A number of systematic uncertainties have to be considered in the cross section measurement. These arise from corrections applied either to the data collected, or the simulated MC samples. The sources of systematic uncertainty can be separated into experimental and theoretical categories.

Uncertainties can be either bin-to-bin correlated or uncorrelated. The uncertainties are propagated by one of two methods:

- The offset method, which is used for propagation of bin-to-bin correlated uncertainties,
- The toy Monte Carlo method, which is used for uncorrelated uncertainties.

Many systematic uncertainty sources actually consist of both correlated and uncorrelated components. In those cases, it is possible to construct a *combined toy MC method* which includes both the correlated and uncorrelated components. The toy MC method is described in Sec. 7.1. Statistical uncertainties are treated as uncorrelated between bins.

The offset method varies each correction up to the upper limit of its systematic uncertainty, and similarly down to the lower limit. The contribution of each correction's uncertainty to the correlated systematic uncertainty on the combined cross section, called a nuisance parameter, is taken as the symmetric approximation  $\Delta = (\delta^{up} - \delta^{down})/2$ , where  $\delta^{up(down)}$  is the correction factor when shifting each correction up (down).

### 7.1 Propagation of Uncertainties Using the Toy Monte Carlo Method

Propagation of uncorrelated uncertainties, as well as propagation of combined correlated and uncorrelated uncertainties, can be performed using the toy MC method. This involves preparing a number of samples  $N$ , of biases  $B_i^k$ , where  $i = 1 \dots N$  runs over the number of samples and  $k$  runs over bin number. Thus in each bin,  $k$ , there are  $N$  biases to be applied to the scale factor (SF). The bias in each case is taken as a Gaussian random number with a mean of 0 and standard deviation equal to the uncorrelated uncertainty plus the statistical uncertainty, such that:

$$B_i^k = \Delta SF_{\text{stat+uncorr}}^k \cdot \text{Gauss}^k(0, 1). \quad (7.1)$$

This results in  $N$  samples of the correction factor in each bin for each SF:

$$SF^k \longrightarrow SF + B_i^k \quad (7.2)$$

The systematic uncertainty is then taken to be the standard deviation of these samples. This method explains how to propagate an uncorrelated uncertainty but systematic uncertainties are

usually some combination of uncorrelated and correlated components. The above prescription can be extended to take into account this mixture. This is called the combined toy MC method and follows a similar procedure, with the addition of the correlated uncertainty sources into the biases:

$$B_i^k = \Delta\text{SF}_{\text{stat+uncorr}}^k \cdot \text{Gauss}^k(0, 1) + \sum_{s=1}^S \Delta\text{SF}_{\text{cor},s}^k \cdot \text{Gauss}(0, 1)_{i,s} \quad (7.3)$$

where  $s = 1 \dots S$  runs over all correlated sources. An important distinction to note is that for the uncorrelated component, the Gaussian random numbers are independent for each bin  $k$  and each sample  $i$ , whereas for the correlated component,  $\text{Gauss}(0, 1)_{i,s}$  is the same for all bins  $k$  and a given source  $s$  and sample  $i$ .

Certain uncertainty sources have differing types of correlation. They can be correlated bin-to-bin and between data sets, correlated bin-to-bin but uncorrelated across data sets, uncorrelated bin-to-bin but correlated across data sets, or fully uncorrelated. To correctly take these correlations into account, correlation matrices for each uncertainty in each data set must be constructed and decomposed. Construction of the correlation matrices is described below.

### 7.1.1 Extraction of Correlated Uncertainties

For  $S$  systematic shifts in  $K$  bins, the elements of the covariance matrix  $C$  are given by [62]:

$$C_{ij} = \sum_{s=1}^S (m_{is} - \mu_i)(m_{js} - \mu_j) \quad (7.4)$$

where

- $i, j$  is a bin number from 1 to  $K$ ,
- $\mu_{i(j)}$  is the central value of the SF in bin  $i(j)$ ,
- $m_{i(j)s}$  is the scale factor in bin  $i(j)$  for systematic  $s$ .

$C$  can be written as:

$$C_{ij} = G_{il}^{-1} D_{lk} G_{kj} \quad (7.5)$$

where the eigenvectors of  $C$  make up the columns of  $G^{-1}$ , and  $D$  is a diagonal matrix of the eigenvalues, with the indices going from 1 to  $K$  bins.

Decomposition of the matrix following the prescription in [62] gives a number of bin-to-bin correlated systematic uncertainties and an uncorrelated uncertainty, which can be represented as nuisance parameters, allowing for coherent treatment of the correlated uncertainties.

## 7.2 Experimental Systematic Uncertainties

### 7.2.1 Electron Energy Scale and Resolution Uncertainty

The electron energy scale correction described in Sec. 5.5.2 has some associated systematic uncertainties, arising from [52]:

- *Statistical* component of the scale uncertainty
- Uncertainty from possible bias of the calibration *method*
- Scale uncertainty from the choice of *generator*
- Uncertainty from the presampler energy scale
- Imperfect knowledge of the material in front of the EM calorimeter
- low- $p_T$  uncertainty

The maximum deviation from the nominal result when independently applying each component's fractional up/down shift to Monte Carlo is taken as the uncertainty contribution from that component to the cross section measurement. The total energy scale uncertainty is the quadratic sum of the components [63].

The same technique is applied to obtain the uncertainty from the energy resolution, i.e. the maximum deviation from up and down variations with respect to the nominal smearing correction.

### 7.2.2 Di-Electron Trigger Efficiency Uncertainty

The uncertainty from the di-electron trigger SF described in Sec. 5.5.1 is split into a correlated component, and an uncorrelated component. The uncertainty is propagated using the *combined toy MC method*.

### 7.2.3 Reconstruction and Identification Efficiency Uncertainty

The reconstruction and ID SFs contain a correlated and uncorrelated component and the uncertainties propagated using the *combined toy MC method* described in Sec. 7.1.

### 7.2.4 Electroweak and $t\bar{t}$ Background Uncertainty

The uncertainty arising from the electroweak and  $t\bar{t}$  background normalisations are estimated by varying their cross sections up and down within their uncertainties as stated for each individual contribution in Sec. 5.7.1.

### 7.2.5 Multi-jet Background Uncertainty

The uncertainty from the multi-jet background estimation is obtained by varying the parameters of the estimation procedure, as described in Sec. 5.7.4. More specifically, the range in which the normalisation is obtained is varied and the background is estimated for each variation. The maximum and minimum of the range of the resulting background estimations is taken as an up and down variation for the systematic uncertainty.

## 7.3 Theoretical Systematic Uncertainties

Uncertainties relating to prediction and simulation must also be considered in the cross section calculation. These include the choice of PDF used, the impact of the MC sample's associated parton shower and underlying event simulation, and the choice of MC generator itself.

### 7.3.1 PDF Uncertainty

The CT10 NLO PDF set is used for the nominal matrix element calculations. This set has 52 associated *error sets* [64] which are individually unfolded. These arise from the fact that there are 26 free parameters in the PDF set, giving 26 eigenvector directions and so 52 total error PDFs accounting for up and down variations. These variations are separately added in quadrature and then averaged to give a symmetric uncertainty.

### 7.3.2 Generator (Matrix Element) Uncertainty

The uncertainty arising from the choice of generator is estimated by comparing the cross section result when unfolding using an alternative MC sample, namely  $\text{MC@NLO}$ . This introduces a new *matrix element* while retaining the same parton showering, and the resulting difference in the cross section is taken as the uncertainty from the choice of ME.

### 7.3.3 Parton Shower Uncertainty

Similarly, the parton shower uncertainty is evaluated using an alternate MC,  $\text{POWHEG HERWIG}$  to perform the unfolding. This retains the ME from the nominal sample but uses a different PS. The difference to the nominal is taken to be the systematic uncertainty.

## 8 Results of the Cross Section Measurement

The measured cross section as a function of the di-electron invariant mass can be seen in Fig. 8.1. The contributions from individual sources to the total uncertainty on the cross section are listed in Tab. 8.2 and shown in Fig. 8.2.

The statistical uncertainty on the events in data is labelled *Stat. Uncertainty* while that from simulation is labelled *Stat. Uncertainty (MC)*. The simulation sample size is significantly larger than that from data and accordingly the statistical uncertainty from simulation is lower. The shape of the statistical uncertainty contribution reflects the shape of the  $Z$  mass distribution.

The largest systematic contribution comes from the electron energy scale uncertainty, which is taken as the quadratic sum of several individual contributions to the uncertainty as described in Sec. 7.2.1. The individual contributions are calculated as the maximum of the up and down variations in the offset method of uncertainty propagation described in Sec. 7. The statistical component of the electron energy scale uncertainty is the most significant factor in the two central bins around the  $Z$  peak, as well as the highest mass bin, contributing an uncertainty of  $\sim 0.9\%$  and  $\sim 0.6\%$  respectively. The highest contribution of the energy scale uncertainty in the lowest mass bin arises from the uncertainty from imperfect knowledge in the material in front of the EM calorimeter.

The electron energy resolution uncertainty is taken as the maximum of the up and down variations in each mass bin. The smearing applied to the simulation to correct the energy resolution is derived from fits to the peak of the invariant mass distribution as described in Sec. 5.5.3. The measurement is therefore highly sensitive to the resolution uncertainty and it's a significant contribution of the order of  $0.5 - 0.8\%$ .

The trigger, ID, and reconstruction scale factor uncertainties are propagated using the *combined toy MC method*. Of these, the reconstruction SF uncertainty is the largest contribution in each bin. For all three SFs, the uncertainty is largest in the lowest mass bin,  $66 - 76$  GeV.

The uncertainty from boson  $p_T$  reweighting is taken from the difference in the cross sections when reweighting the  $p_T$  distribution of the signal sample to POWHEG PYTHIA8 and to SHERPA. The uncertainty is on the order of a per mille in each mass bin.

The uncertainty labelled *EWK Background* encompasses the uncertainty from the normalisation of the individual electroweak background as well as the  $Z/\gamma^* \rightarrow \tau\tau$  background. It is most significant in the tails of the mass distribution. The uncertainty is evaluated by coherent variation of the cross sections up and down within their uncertainties, the sources of which are described in Sec. 5.7.

The shape of the multi-jet background uncertainty is similar to the EWK background uncertainty and is of the order of  $0.2\%$  in the two bins furthest from the  $Z$  peak.

The statistical uncertainty from background contributions is insignificant in the two mass bins around the peak, rising to  $0.425\%$  and  $0.135\%$  in the lowest and highest mass bins respec-

tively.

The default MC sample was produced using the POWHEG PYTHIA6 generator, where POWHEG was used to generate the hard scattering and PYTHIA6 was used for parton showering. The uncertainty from the choice of the program used to simulate parton showering is estimated by unfolding using a different showering program while retaining the hard scattering, POWHEG HERWIG. The uncertainty is largest in the 76 – 91 GeV mass bin, 0.541%.

Similarly, the uncertainty from the choice of hard scattering program is estimated by replacing the hard scattering, but retaining the showering program. MC@NLO HERWIG is compared with POWHEG HERWIG. For technical reasons this is not displayed in Tab. 8.2 or Fig. 8.2, but has been calculated on  $Z \rightarrow \mu\mu$  events in the same binning and is of the order of 0.07% in each mass bin [65].

The PDF uncertainty is evaluated using a set of 52 error eigenvectors as described in Sec. 7.3.1, with the treatment as prescribed in [64]. Similar to the uncertainty from hard scattering, technical problems mean that this uncertainty has not been evaluated in  $Z \rightarrow ee$  events, but has been done for  $Z \rightarrow \mu\mu$ . This uncertainty is  $\sim 0.1\%$  in the first and last bins, and  $< 0.1\%$  in the two central bins [65].

$m_Z$ [GeV]	$\sigma_{m_Z/\gamma^*}$ [pb]	stat. unc. [pb]	syst. unc. [pb]	lumi. unc. [pb]
$66.00 < m_Z < 76.00$	0.696	0.008	0.009	0.013
$76.00 < m_Z < 91.00$	12.162	0.020	0.215	0.219
$91.00 < m_Z < 106.00$	14.283	0.021	0.198	0.257
$106.00 < m_Z < 116.00$	0.481	0.005	0.007	0.009

**Table 8.1:** Fiducial  $Z \rightarrow ee$  cross section as a function of di-electron invariant mass. Statistical, systematic, and luminosity uncertainties are shown as percentages of cross section.

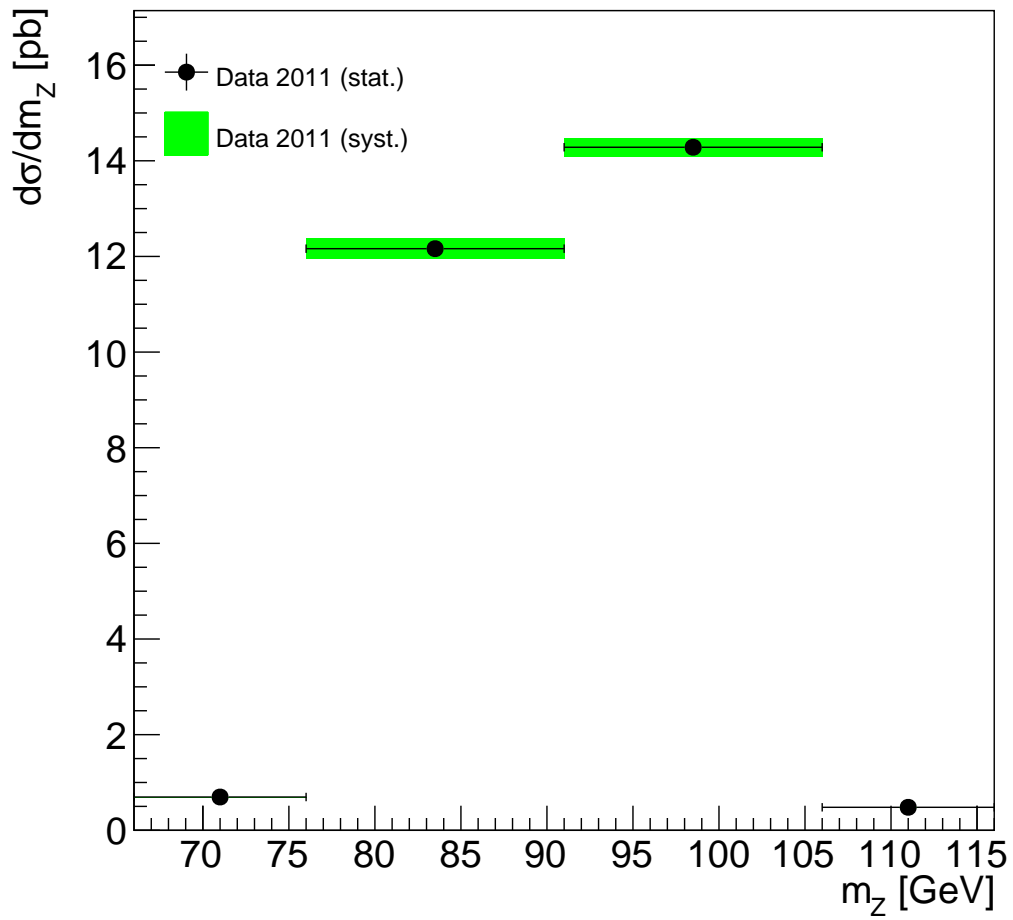


**Figure 8.1:** Measured  $Z \rightarrow ee$  differential cross section as a function of di-electron invariant mass.

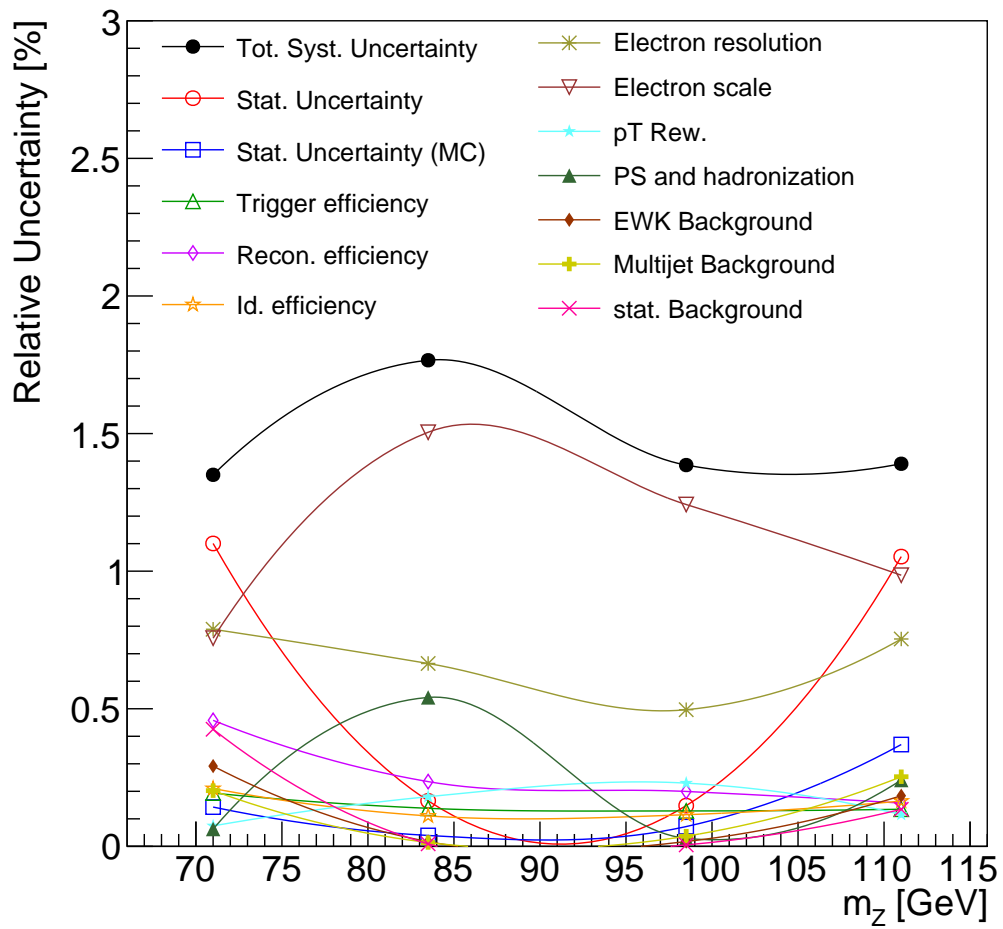


**Figure 8.2:** Systematic uncertainties as a percentage of the differential  $Z \rightarrow ee$  cross section measurement.

$m_Z$ [GeV]	66.00, 76.00	76.00, 91.00	91.00, 106.00	106.00, 116.00
Trigger efficiency	0.194	0.138	0.129	0.135
Recon. efficiency	0.458	0.235	0.200	0.157
Id. efficiency	0.210	0.111	0.115	0.165
Electron resolution	0.789	0.665	0.497	0.754
Electron scale	0.757	1.505	1.242	0.985
pT Rew.	0.074	0.180	0.230	0.116
PS and hadronization	0.063	0.541	0.029	0.241
EWK Background	0.292	0.017	0.017	0.184
Multijet Background	0.202	0.014	0.037	0.253
stat. Background	0.425	0.009	0.005	0.135
Stat. Uncertainty (MC)	0.143	0.040	0.072	0.370
Stat. Uncertainty	1.101	0.165	0.148	1.053
Tot. Syst. Uncertainty	1.350	1.766	1.386	1.390

**Table 8.2:** Systematic uncertainties as a percentage of the  $Z \rightarrow ee$  cross section as a function of di-electron invariant mass.

## 8.1 Comparison with Theoretical Predictions

The data are compared with theoretical comparisons in an extrapolated phase space with  $|\eta| < 2.5$ . An extrapolation factor,  $E_Z$  is calculated by taking ratio of the sum of generated event weights between the experimental and extrapolated phase spaces in measurement bins as described by Eqn. 5.3.

The uncertainties on the extrapolation factors are estimated taking into account four different contributions:

- uncertainties within one PDF set,  $\Delta_{\text{CT10}}$ , estimated by PDF reweighting the sample used to calculate the factors and evaluating the uncertainty following the standard prescription [66].
- differences between PDF sets,  $\Delta_{\text{PDFmax}}$ , taken as the maximum deviation between the factor calculated using the CT10 NLO PDF set and factors calculated from different PDF sets
- uncertainty from the generator used to evaluate the factor,  $\Delta_{\text{ME}}$ , is taken as the difference in the factor when using an alternate generator
- uncertainty from the showering in the sample used to calculate the factor,  $\Delta_{\text{PS}}$ , is taken as the difference in the factor when using an alternate showering program

The extrapolation factors and uncertainties in mass bins are listed in Tab. 8.3, and shown in Fig. 8.3.

$m_Z$ [GeV]	$E_Z$	$\Delta_{\text{CT10}}[\%]$	$\Delta_{\text{PDFmax}}[\%]$	$\Delta_{\text{ME}}[\%]$	$\Delta_{\text{PS}}[\%]$	$\Delta_{\text{tot}}[\%]$
$66.00 < m_Z < 76.00$	0.8090	0.10	0.07	-0.05	0.08	0.15
$76.00 < m_Z < 91.00$	0.8087	0.10	0.07	-0.05	-0.04	0.14
$91.00 < m_Z < 106.00$	0.8086	0.09	0.07	0.06	-0.04	0.14
$106.00 < m_Z < 116.00$	0.8071	0.09	0.07	-0.17	0.09	0.22

**Table 8.3:**  $E_Z$  factors and associated uncertainties in bins of invariant mass.

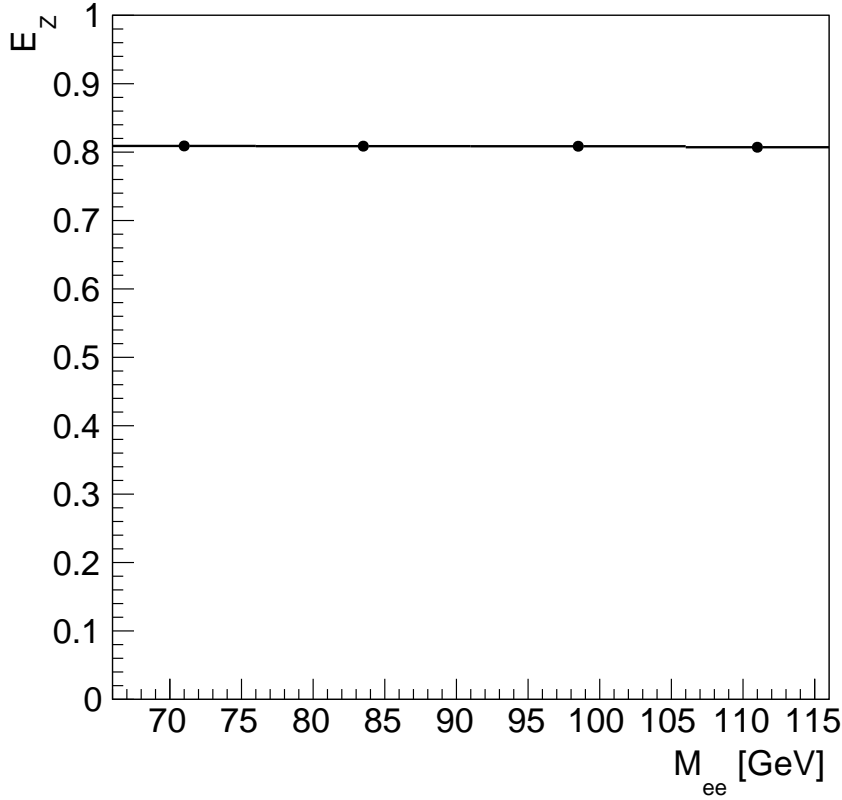


**Figure 8.3:**  $E_Z$  factors in bins of invariant mass used to extrapolate the experimental measurement to a different phase space for comparison with theoretical predictions.

$m_Z^{min} - m_Z^{max}$ [GeV]	$d\sigma/dm_Z$ [pb]	$\delta_{stat.}, \%$	$\delta_{unc.}, \%$	$\delta_{cor.}, \%$	$\delta_{tot.}, \%$
66.00–76.00	0.87	1.10	0.41	1.21	1.68
76.00–91.00	15.03	0.17	0.95	1.48	1.77
91.00–106.00	17.66	0.15	0.82	1.11	1.39
106.00–116.00	0.59	1.05	0.74	1.16	1.73

**Table 8.4:** Extrapolated differential cross section for the  $Z \rightarrow ee$  process  $d\sigma/dm$  measured for and  $P_{t,\ell} > 20$  GeV.  $\delta_{stat.}$ ,  $\delta_{unc.}$ ,  $\delta_{corr.}$  and  $\delta_{tot.}$  represent statistical, uncorrelated systematic, correlated systematic and total uncertainties.

The extrapolated cross section is compared with theoretical predictions from NNLO QCD calculations with additional NLO electroweak corrections in Fig. 8.4. The calculations are based on the following NNLO PDF sets:

- CT10 NNLO [64, 67],

- ABM11 NNLO 5fl [68],
- HERAPDF 1.5 NNLO [69, 70],
- MSTW2008 NNLO [71],
- MSTW2008CPdeut NNLO [72],
- NNPDF2.3 NNLO  $\alpha_S = 0.118$  [73],
- JR09 NNLO [74], and
- ATLAS epWZ NNLO [75] (the ATLAS fit to the 2010 W, Z inclusive data).

The best description of the data is given by the ATLAS epWZ and ABM11 fits, but none of the fits describe the shape very well. In particular the second and final bins are poorly described by all of the predictions.

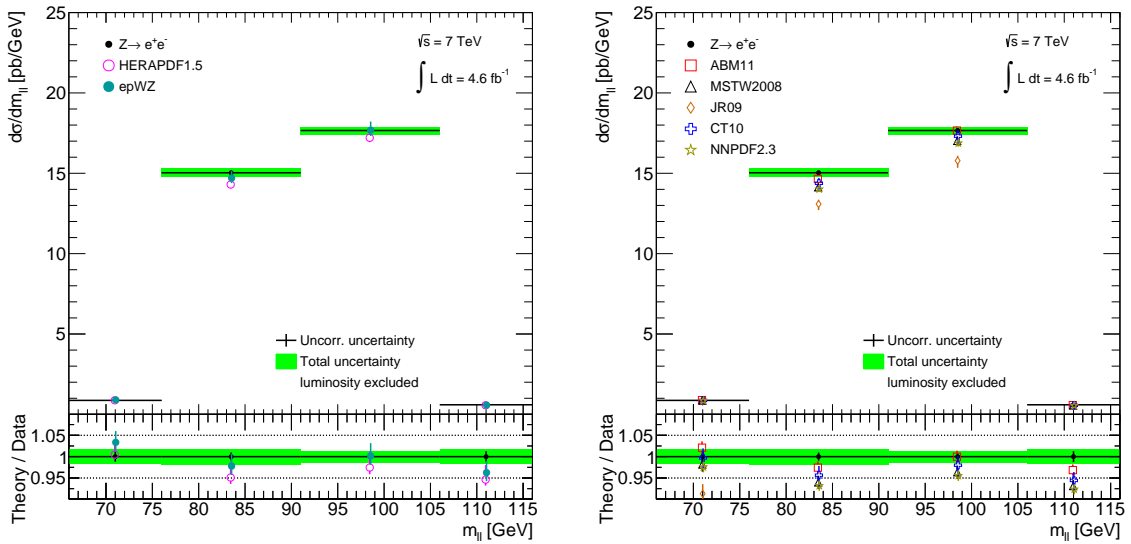


**Figure 8.4:** Extrapolated fiducial  $Z \rightarrow ee$  cross section as a function of di-electron invariant mass compared to NNLO QCD predictions with NLO EW corrections based on various NNLO PDFs.

## 9 Combination of Electron and Muon Cross Section Measurements

### 9.1 Combination Procedure

In addition to the lineshape measurement, differential measurements of the  $Z \rightarrow \ell\ell$  cross section as a function of rapidity, and the  $W \rightarrow \ell\nu$  cross section as a function of pseudo-rapidity separately in electron [76, 77] and muon [78, 79] channels were performed. The  $W \rightarrow \ell\nu$  cross sections were also measured double-differentially as a function of pseudo-rapidity and lepton  $p_T$ . This chapter describes the combination of the separate channels.

The combination of the different measurements was performed using code developed at HERA for the combination of DIS cross section data [80]. To perform the combination, correlations in the systematic uncertainties both bin-to-bin, and across data sets need to be accounted for. The data are combined in a simultaneous averaging which takes into account these correlations. The procedure distinguishes between those systematic uncertainty sources which are uncorrelated bin-to-bin, uncorrelated across data sets, and fully correlated bin-to-bin and across data sets. An overview of the correlations between the 5 different channels can be seen in Tab. 9.1 in terms of nuisance parameters.

For those uncertainties that are uncorrelated bin-to-bin, but correlated across cells, and that are propagated using the Toy MC method as described in Sec. 7.1.1, correlation and covariance matrices can be built. These matrices can be decomposed into components which are uncorrelated with each other, but correlated across measurements. These can be represented as nuisance parameters to account for these correlations in the averaging. Correlation matrices built in this way can be seen in Figs 9.1-9.5. The covariance matrices are presented in Appendix A.

The measured cross sections are extrapolated to the common fiducial volume as described in Sec. 5.3.

#### 9.1.1 Linear Averaging

For a measurement  $\mu$  with uncertainty  $\Delta$ , assuming a Gaussian shape of the uncertainty, the measurement can be considered as a probability distribution function (PDF) for a quantity  $m$ :

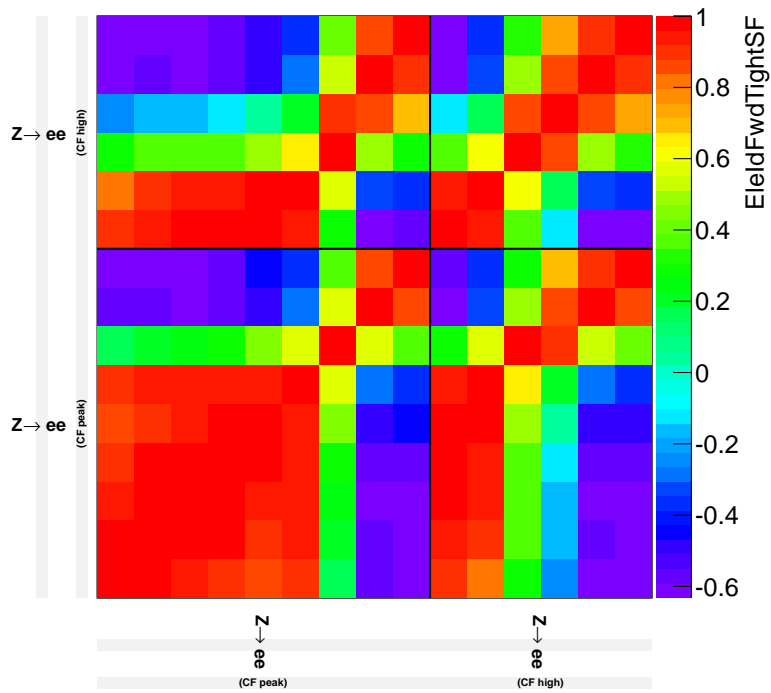
$$P(m) = \frac{1}{\sqrt{2\pi}\Delta} \exp\left(-\frac{(m - \mu)^2}{2\Delta^2}\right) \quad (9.1)$$

This can be written as a  $\chi^2$  function by taking  $-2\log$ :

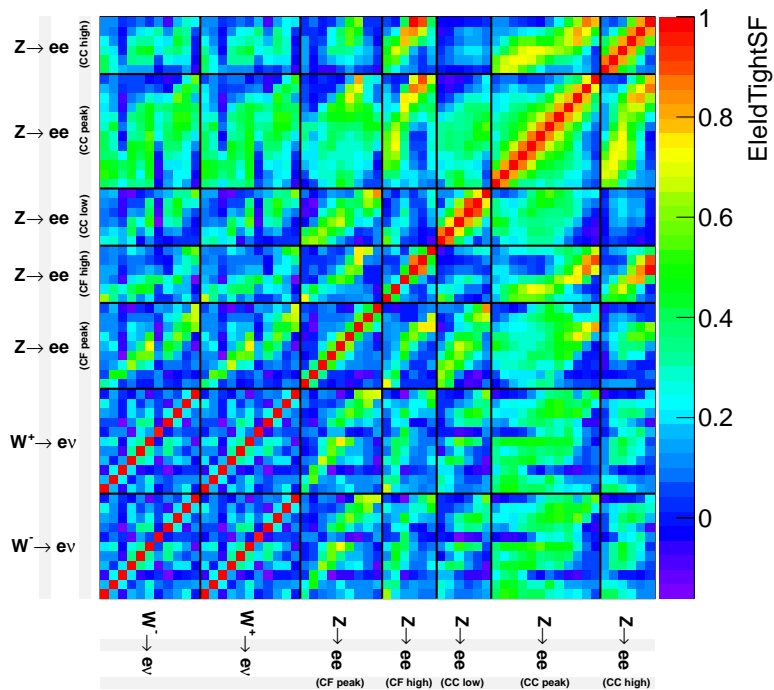
$$\chi^2(m) = \frac{(m - \mu)^2}{\Delta^2} \quad (9.2)$$

Uncertainty Source	Channel				
	$W \rightarrow e\nu$	$Z \rightarrow ee$	$Z \rightarrow ee$ (CF)	$W \rightarrow \mu\nu$	$Z \rightarrow \mu\mu$
<b>Lepton Energy (Momentum) Scale</b>	1	1	1	2	2
Electron Energy Resolution	3	3	3	–	–
Muon Momentum Resolution (ID)	–	–	–	4	4
Muon Momentum Resolution (MS)	–	–	–	5	5
Muon Curvature	–	–	–	6	6
Electron Charge MisID	7	–	–	–	–
<b>Jet Energy Scale</b>	8	–	–	8	–
Jet Resolution	9	–	–	9	–
MET Energy Scale	10	–	–	10	–
MET Resolution	11	–	–	11	–
Electron ID Tight SF	13	13	13	–	–
Electron Fwd ID SF	–	–	14	–	–
Lepton Trigger SF	15	16	15	17	17
Lepton Reco SF	18	18	18	19	19
Lepton Iso SF	20	–	20	21	21
<b>Boson Pt Reweighting</b>	23	23	23	23	23
TheoryME	24	24	24	24	24
TheoryPS	25	25	25	25	25
TheoryPDF	26	26	26	26	26
Pileup Rescaling	27	27	27	27	27
<b>Background (EWK)</b>	28	28	43	28	28
<b>Background (Multijet)</b>	29	30	u	32	33
PI Subtraction	34	34	34	–	–
Electron ID Tight SF (stat)	u36	u36	u36	–	–
Electron Fwd ID SF (stat)	–	–	u37	–	–
Electron Trigger SF (stat)	u38	u39	u38	–	–
Electron Reco SF (stat)	u40	u40	u40	–	–
Electron Iso SF (stat)	u41	–	u41	–	–
Muon SF (stat)	–	–	–	u42	u42
Background Statistical Uncertainty	u	u	u	u	u
Extrap. PS	35	35	35	35	35
Extrap. ME	36	36	36	36	36
Extrap. Uncor.	u	u	u	u	u
Theory Smoothing Uncor.	–	u	–	u	u

**Table 9.1:** Summary of the correlations for the uncertainties. Each number represents a nuisance parameter. Cells with a shared nuisance parameter are treated as correlated, whereas cells containing  $u$  are treated as uncorrelated.  $uN$  represents an uncertainty which is uncorrelated bin-to-bin, but correlated across cells with the same  $N$ . Uncertainties in red consist of multiple nuisance parameters.

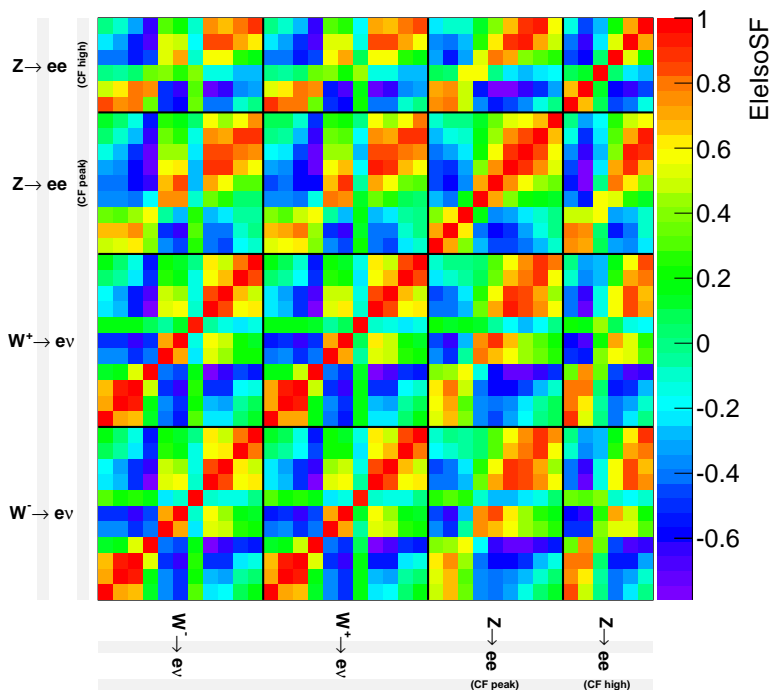


(a) Forward electron ID scale factor uncertainty

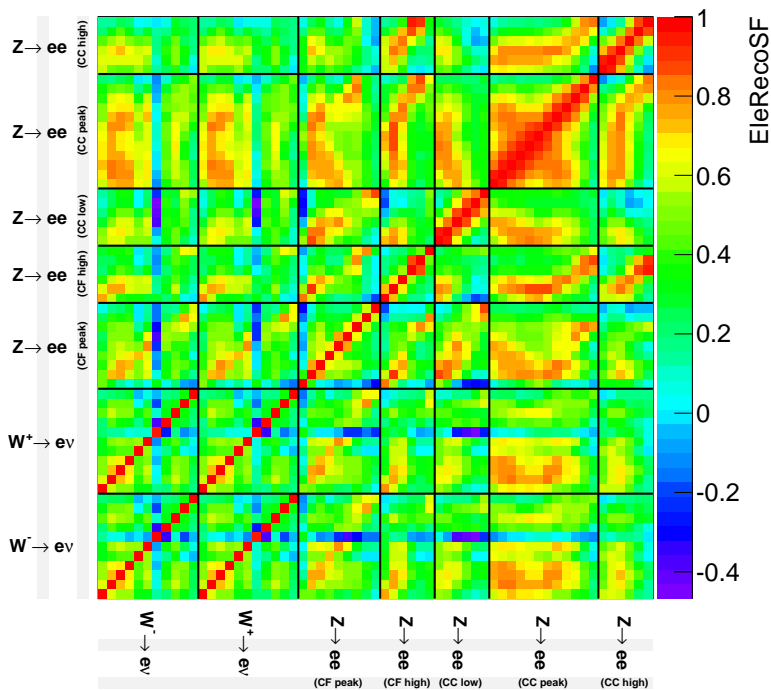


(b) Electron ID scale factor uncertainty

**Figure 9.1:** Bin-to-bin correlations across all measurements for the systematic uncertainties from the forward electron ID scale factor (top), and the electron ID scale factor (bottom).

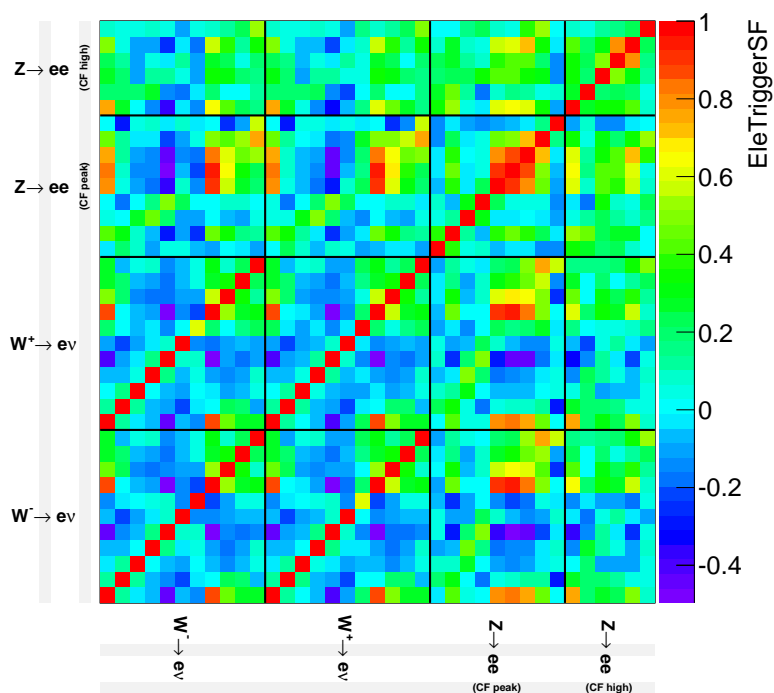


(a) Electron isolation scale factor uncertainty

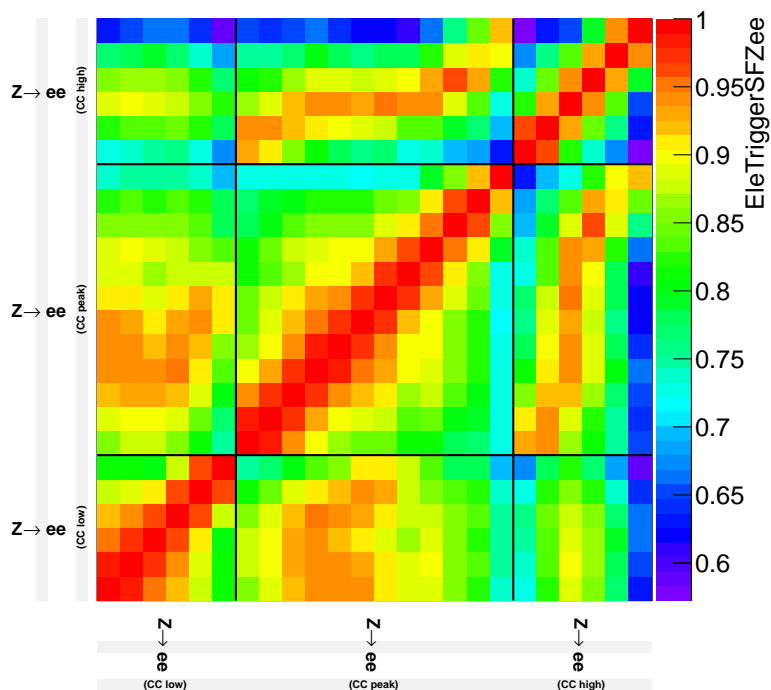


(b) Electron reconstruction scale factor uncertainty

**Figure 9.2:** Bin-to-bin correlations across all measurements for the systematic uncertainties from the electron isolation scale factor (top), and the electron reconstruction scale factor (bottom).

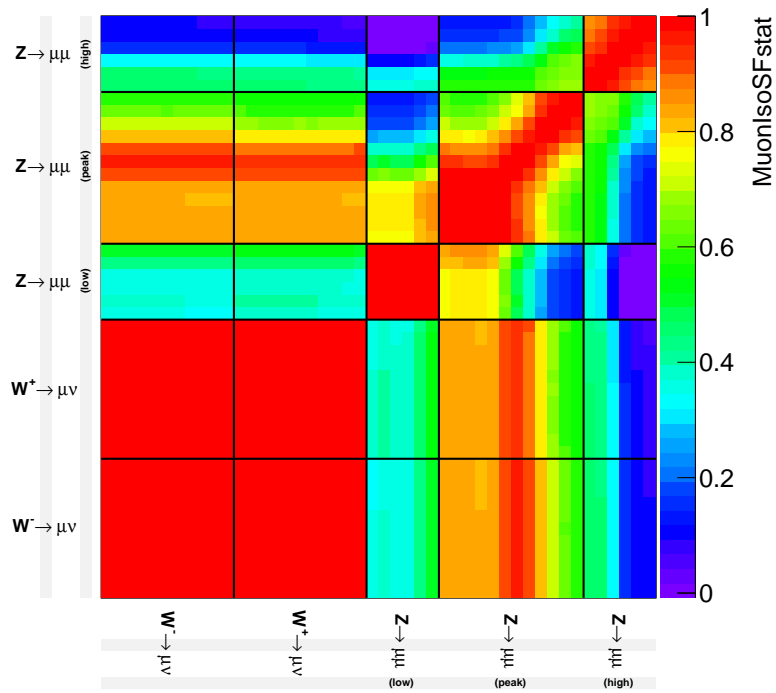


(a) Single electron trigger scale factor uncertainty

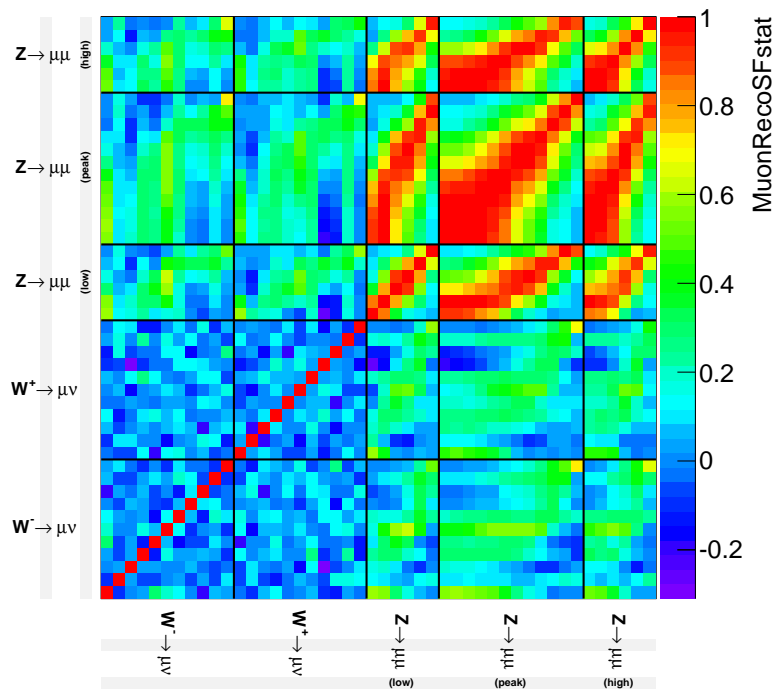


(b) Di-electron trigger scale factor uncertainty (stat.)

**Figure 9.3:** Bin-to-bin correlations across all measurements for the systematic uncertainties from the single electron trigger scale factor (top), and the di-electron trigger scale factor (bottom).

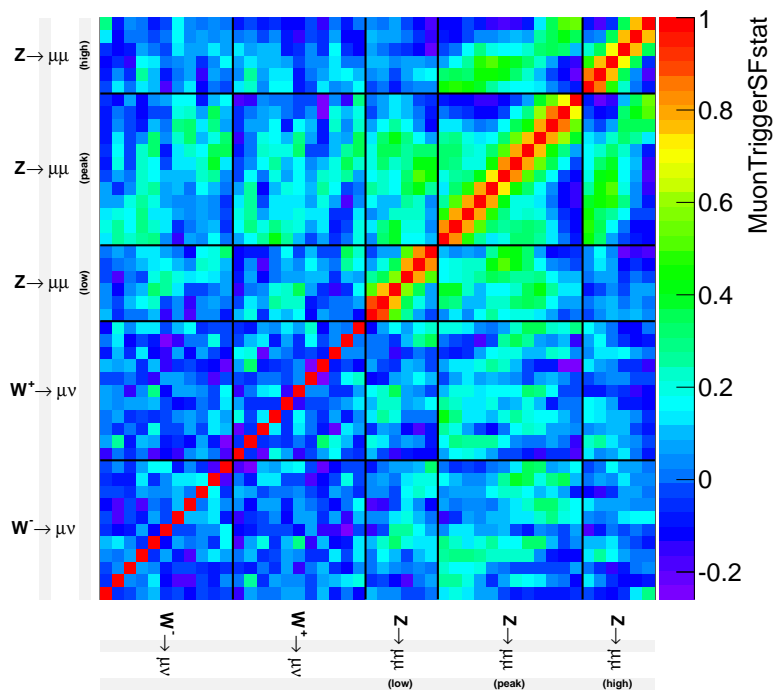


(a) Muon isolation scale factor uncertainty (stat.)



(b) Muon reconstruction scale factor uncertainty (stat.)

**Figure 9.4:** Bin-to-bin correlations across all measurements for the systematic uncertainties from the statistical components of the muon isolation scale factor (top), and the muon reconstruction scale factor (bottom).



(a) Muon trigger scale factor uncertainty (stat.)

**Figure 9.5:** Bin-to-bin correlations across all measurements for the systematic uncertainties from the statistical components of the muon trigger scale factor.

The averaging procedure takes place by  $\chi^2$  minimisation. The minimum of the  $\chi^2$  function is reached at

$$\frac{d\chi^2}{dm} = 0 \quad (9.3)$$

In the nuisance parameter representation, we can construct the following  $\chi^2$  function for a single data set:

$$\chi^2(\mathbf{m}, \mathbf{b}) = \sum_i \frac{(m_i - \mu_i - \sum_j \Gamma_i^j b_j)^2}{\Delta_i^2} + \sum_j b_j^2 \quad (9.4)$$

where

- $\mathbf{b}$  defines a vector of nuisance parameters  $b_j$  corresponding to each source of systematic uncertainty,
- summation over  $i$  runs over all data points, and summation over  $j$  runs over all correlated sources of systematic uncertainty,
- $\Gamma_i^j$  is the relative correlated systematic uncertainty, and
- $\Delta_i$  is the uncorrelated systematic uncertainty.

$\Delta_i^2$  can be separated into statistical and uncorrelated components:

$$\Delta_i^2 = \Delta_{i,stat}^2 + \Delta_{i,uncor}^2 \quad (9.5)$$

$\Gamma_i^j$  is a representation of the correlated systematic uncertainties where the uncertainty is considered proportional to the central value:  $\Gamma_i^j = m_i \gamma_i^j$ , where

$$\gamma_i^j = \frac{\partial \mu_i / \partial \alpha^j}{\mu_i} \quad (9.6)$$

and  $\alpha^j$  is the central value of the uncertainty. The relationship  $\partial \mu_i / \partial \alpha^j$  can be seen as the sensitivity of measurement  $\mu$  at point  $i$  to the systematic uncertainty source  $j$ . To combine several different data sets, a more general form of Eq. 9.4 is needed to sum over the data sets:

$$\chi_{tot}^2(\mathbf{m}, \mathbf{b}) = \sum_e \sum_{i=1}^{N_M} \frac{(m_i - \mu_{i,e} - \sum_{j=1}^{N_S} \Gamma_{i,e}^j b_j)^2}{\Delta_{i,e}^2} w_{i,e} + \sum_{j=1}^{N_S} b_j^2 \quad (9.7)$$

The sum over  $e$  runs over all data sets, and the factor  $w_{i,e}$  is equal to 1 if data set  $e$  contains a measurement at point  $i$  and is 0 otherwise. The factor  $\Gamma_{i,e}^j$  similarly quantifies the sensitivity of a measurement at  $i$  for data set  $e$  to systematic uncertainty  $j$ .

### 9.1.2 Iterative Procedure of Minimisation

Uncertainties that are considered functions of the value of the central measurement,  $m$  to which they apply are treated using a multiplicative treatment. As mentioned in Sec. 9.1.1, this is represented in the correlated systematic uncertainty case as:

$$\Gamma_i^j = m_i \gamma_i^j \quad (9.8)$$

For the uncorrelated and statistical cases respectively:

$$\Delta_{i,unc} = m_i \delta_{i,unc} \quad (9.9)$$

$$\Delta_{i,stat} = \delta_{i,unc} \sqrt{\mu_i m_i} \quad (9.10)$$

From these and Eqs. 9.4 and 9.5, the denominator can be written

$$\Delta_i^2 = \delta_{i,stat}^2 \mu_i \left( m_i - \sum_{j=1}^{N_S} \gamma_i^j m_i b_j \right) + \delta_{i,unc}^2 (m_i)^2 \quad (9.11)$$

giving

$$\chi^2(\mathbf{m}, \mathbf{b}) = \sum_i \frac{(m_i - \mu_i - \sum_j \gamma_i^j m_i b_j)^2}{\delta_{i,stat}^2 \mu_i \left( m_i - \sum_j \gamma_i^j m_i b_j \right) + \delta_{i,unc}^2 (m_i)^2} + \sum_j b_j^2 \quad (9.12)$$

The average is then found using an iterative procedure whereby initial approximations for  $\mu_{i,ave}$  and  $\beta_j$  are obtained using Eq. 9.4 and used to recalculate Eqs 9.8 and 9.11 as  $\Gamma_i^j = \mu_{i,ave} \gamma_i^j$  and  $\Delta_i^2 = \delta_{i,stat}^2 \mu_i \left( \mu_{i,ave} - \sum_{j=1}^{N_S} \gamma_i^j \mu_{i,ave} \beta_{j,ave} \right) + \delta_{i,unc}^2 (\mu_{i,ave})^2$ . The process to determine  $\mu_{i,ave}$  is then repeated iteratively and the minimisation of Eq. 9.4 is applied with these recalculated uncertainties.

## 9.2 Combination Results

The combination of differential  $d\sigma/dm_Z$  cross sections separately measured in the  $66 < m_Z < 116$  GeV region for the electron and muon channels is performed. The combined cross section can be seen in Tab. 9.2 and Fig. 9.6. The data are in good agreement with high precision, particularly in the two central mass bins.

This region is also measured differentially in rapidity separately for the muon and electron channels, with an additional electron measurement in the forward region of the detector. The combined cross section is listed in Tab. 9.4 and shown in Fig. 9.7(a). The central electron and muon data show reasonable agreement and are measured with high precision. The measured central electron cross section is higher than the muon cross section in every bin except the highest rapidity bin. There is noticeable tension with the forward electron measurement which

also has large uncertainties in this region arising from the forward electron ID scale factor efficiency..

The cross section in the low mass region,  $46 < m_Z < 66$  GeV is measured differentially in rapidity separately for the muon and electron channels. The combined cross section is listed in Tab. 9.3 and shown in Fig. 9.8(a). The electron data are systematically higher than the muon data, and also measured to a lower precision in this region, with relatively large statistical uncertainties ( $\sim 2.5\%$  in the highest rapidity bin).

The cross section in the high mass region,  $116 < m_Z < 150$  GeV is measured differentially in rapidity separately for the muon and electron channels, with an additional electron measured in the forward region of the detector. The combined cross section is listed in Tab. 9.5 and shown in Fig. 9.8(b). The central electron and muon data show reasonable agreement within their uncertainties. The forward electron measurement shows some tension particularly in the first bin and has large uncertainties in this region, again arising from the forward electron ID scale factor efficiency, but also with large contributions from the background normalisation.

The combined cross sections for the single differential  $d\sigma/d|\eta|$  for  $W^-$  and  $W^+$  measurements can be seen in Tabs. 9.6–9.7 and Figs. 9.9(a)–9.10(a) respectively. For both  $W^-$  and  $W^+$ , the data are mostly in good agreement. The final four bins in both cases shows not insignificant disagreement between the data, with the electron cross sections 1 – 2% smaller than the muon cross sections. The uncertainties on the electron measurements in this region are large, and arise from an  $m_T$  fit used to estimate the QCD background in this region. The difference in the scale of the  $e, \mu/\text{combination}$  ratio plot with respect to the  $Z$  cross sections should be noted, indicating the high precision of these measurements.

The measurements are in good agreement with  $\chi^2/d.o.f. = 50.36/53$ . The combination was performed over all measurements simultaneously.

Results from the combination of the single differential  $d\sigma/dy$  cross sections from  $Z$  with the double differential  $d\sigma/d|\eta_\ell| dp_{T,\ell}$  cross sections from  $W$  are shown in Appendix B.

The combined  $d\sigma/dm_Z$  cross section measurement in the region  $66 < m_{\ell\ell} < 116$  GeV and the combined  $d\sigma/d|\eta_\ell| W^\pm$  measurements can be compared with the measurement using data collected in 2010 [19].

An improvement in precision can be seen when comparing the 2011  $d\sigma/dm_Z$  measurement in Fig. 9.7(a) with the 2010 measurement in Fig. 9.7(b). It should also be noted that the increase in statistics allows for finer binning in the 2011 measurement.

A similar improvement is seen when comparing the 2011  $d\sigma/d|\eta_\ell| W^-$  measurement in Fig. 9.9(a) with the 2010 measurement in Fig. 9.9(b), and the  $d\sigma/d|\eta_\ell| W^+$  measurement in Fig. 9.10(a) with the 2010 measurement in Fig. 9.10(b).

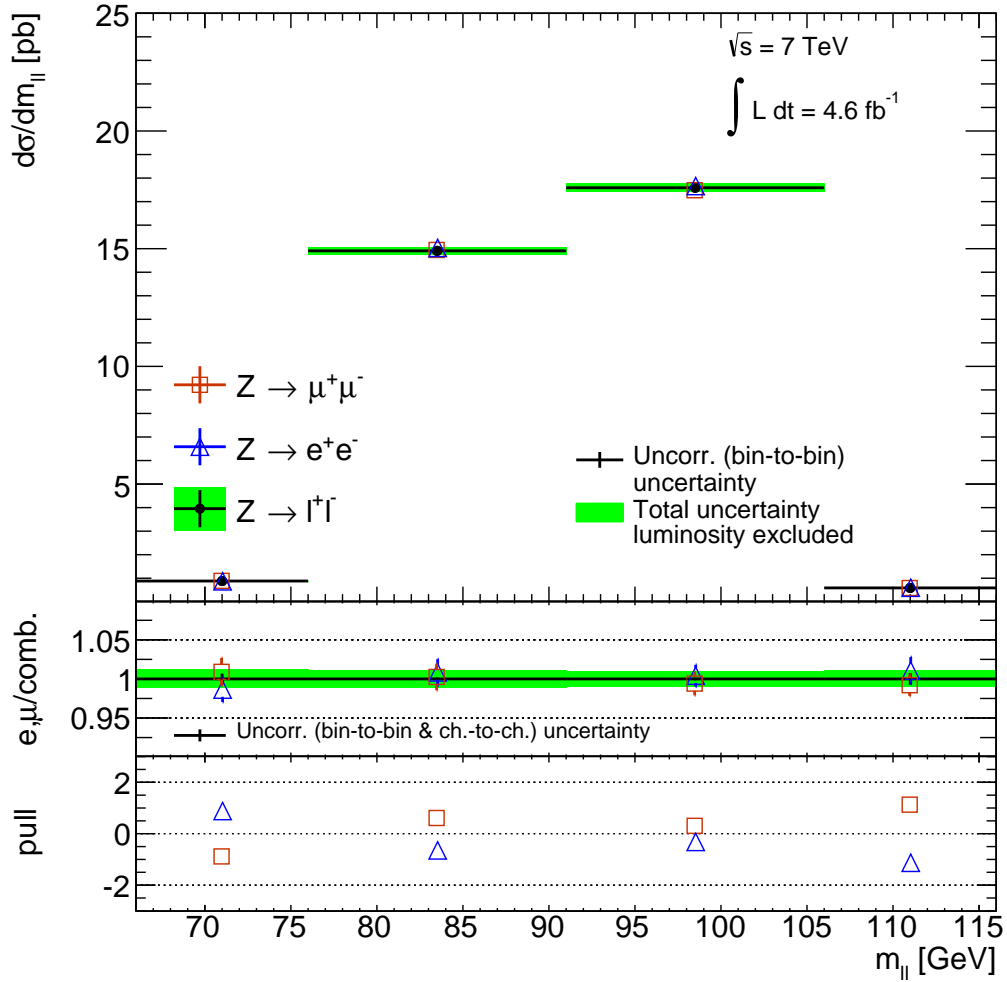
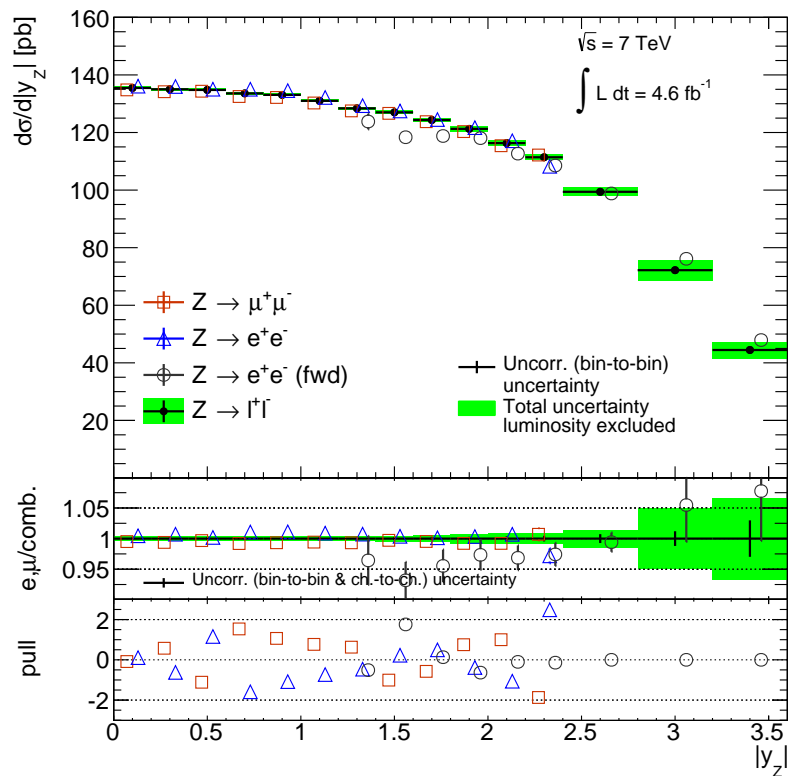


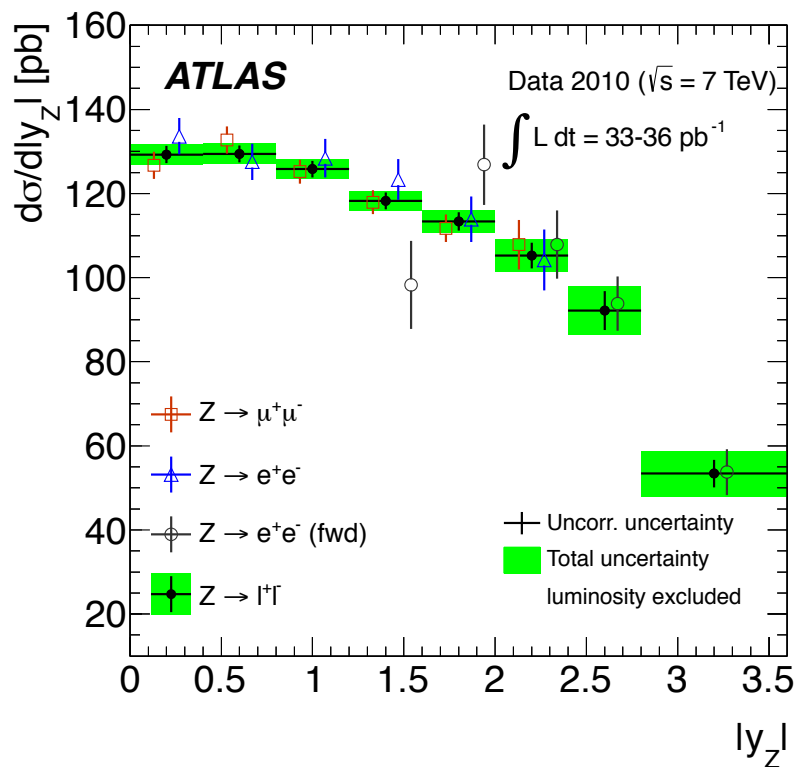
**Figure 9.6:** Differential  $d\sigma/dm_Z$  cross section in the region  $66 < m_{\ell\ell} < 116$  GeV measured using data collected in 2011. Also shown are the individual channel measurements in each bin with uncorrelated uncertainties and the pull from each point.

$m_Z^{min} - m_Z^{max}$ [GeV]	$d\sigma/dm_Z$ [pb]	$\delta_{stat.}, \%$	$\delta_{unc.}, \%$	$\delta_{cor.}, \%$	$\delta_{tot.}, \%$
66.00–76.00	0.88	0.63	0.26	0.96	1.18
76.00–91.00	14.91	0.12	0.13	1.12	1.13
91.00–106.00	17.59	0.11	0.14	0.98	1.00
106.00–116.00	0.59	0.67	0.31	0.78	1.07

**Table 9.2:** Combined differential cross section for the  $Z \rightarrow \ell\ell$  process  $d\sigma/dm$  measured for  $66 < m_Z < 116$  GeV and  $P_{t,\ell} > 20$  GeV.  $\delta_{stat.}$ ,  $\delta_{unc.}$ ,  $\delta_{corr.}$  and  $\delta_{tot.}$  represent statistical, uncorrelated systematic, correlated systematic and total uncertainties.

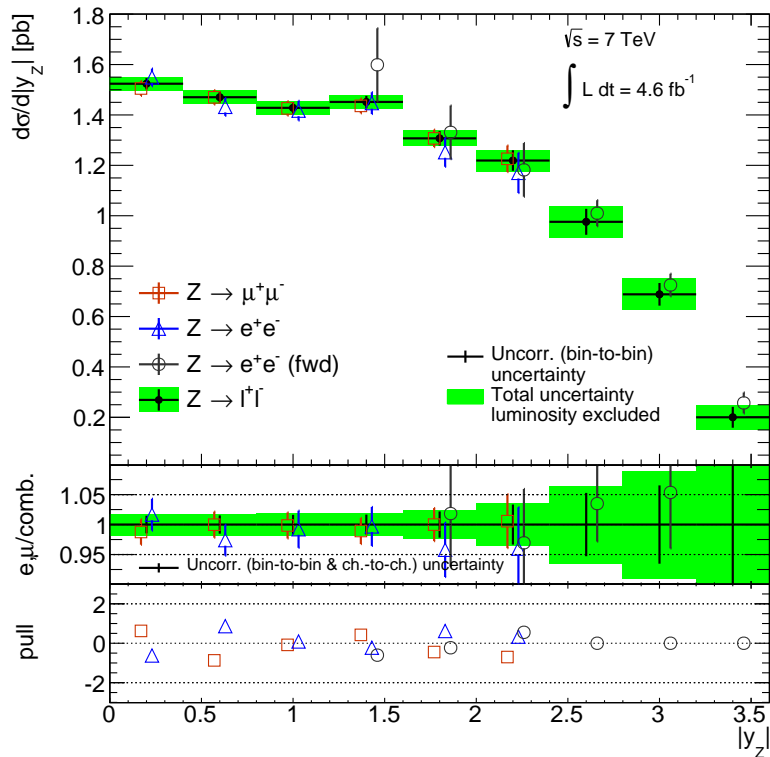
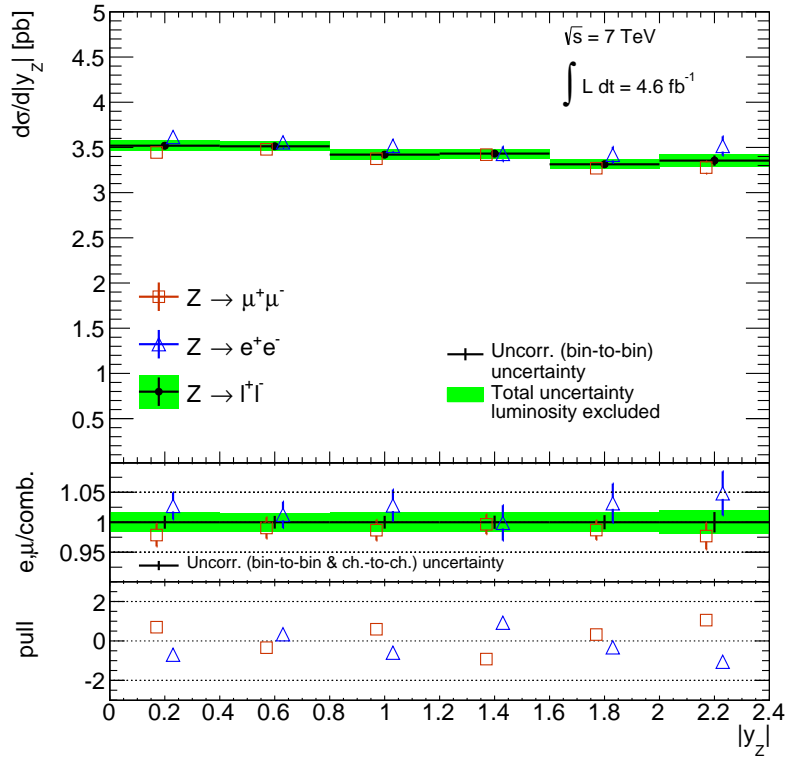


(a)  $Z: 66 < m_{\ell\ell} < 116$  GeV (2011 measurement)

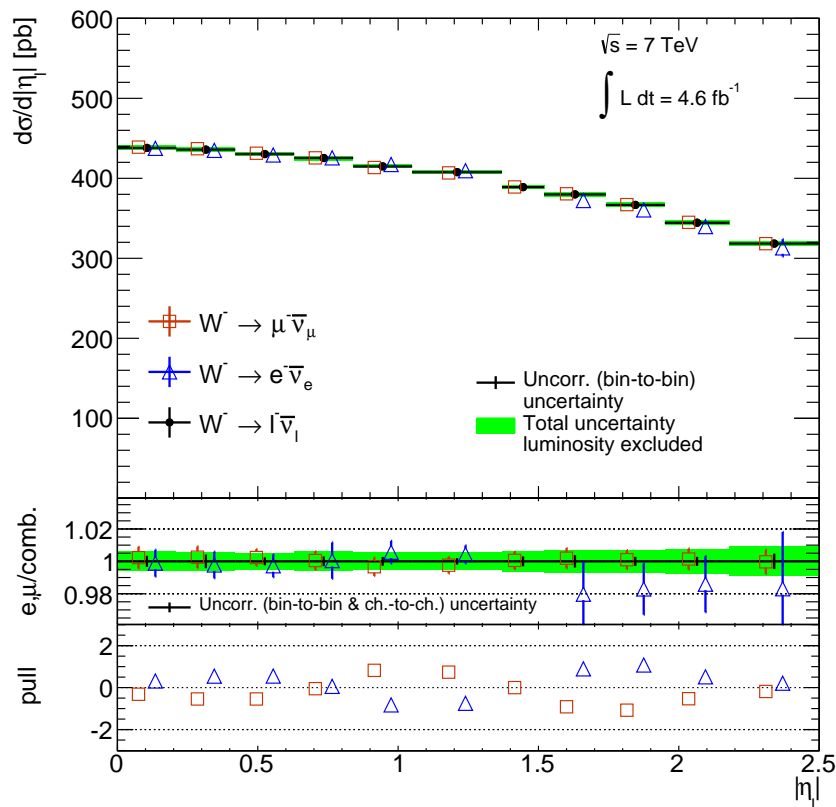
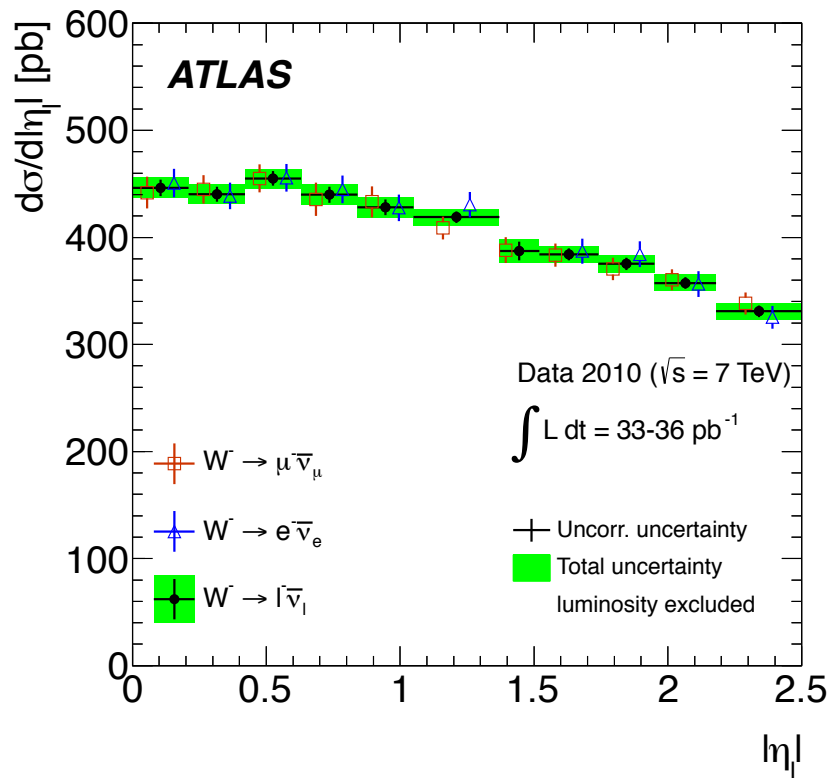


(b)  $Z: 66 < m_{\ell\ell} < 116$  GeV (2010 measurement)

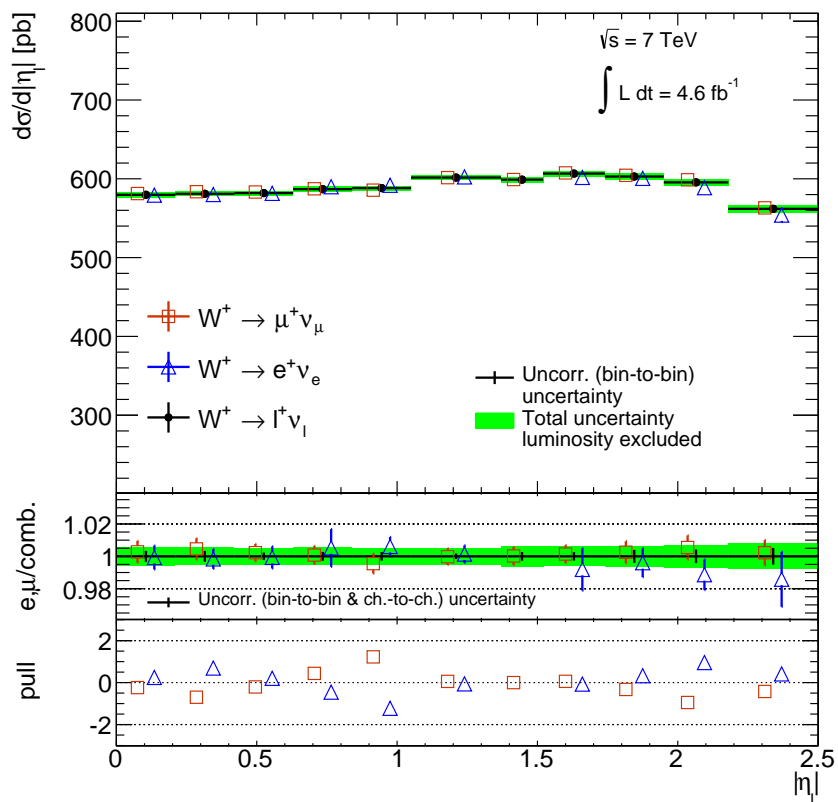
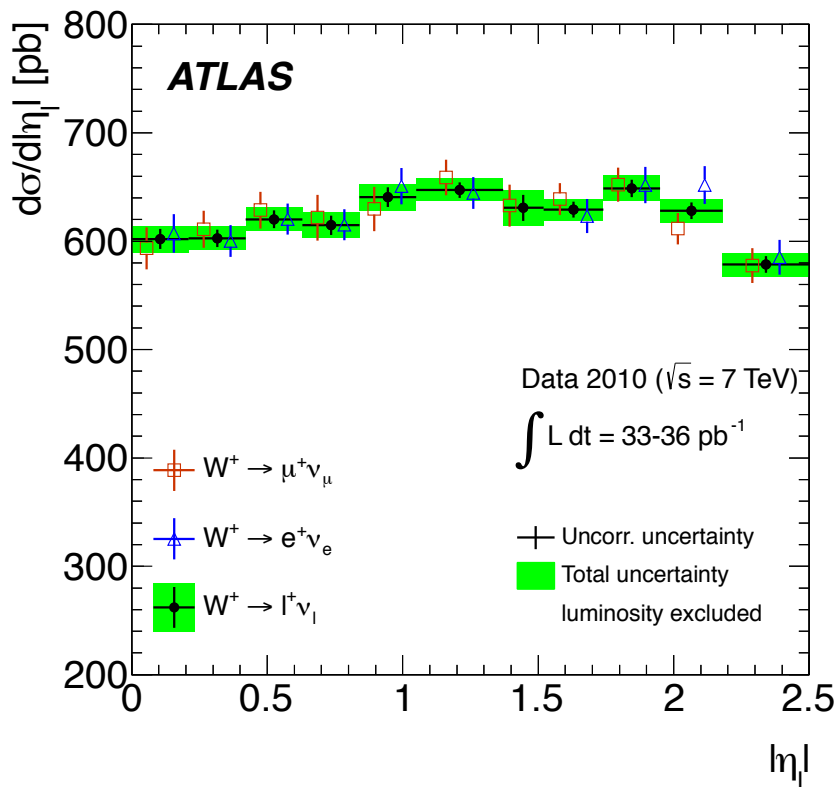
**Figure 9.7:** Combined  $d\sigma/d|y_Z|$  cross section in the region  $66 < m_{\ell\ell} < 116$  GeV measured using data collected in 2011 (top) and 2010 (bottom). Also shown for the 2011 measurement are the individual channel measurements in each bin with uncorrelated uncertainties and the pull from each point.



**Figure 9.8:** Combined  $d\sigma/d|y_Z|$  cross section in the regions  $46 < m_{\ell\ell} < 66 \text{ GeV}$  (top) and  $116 < m_{\ell\ell} < 150 \text{ GeV}$  (bottom) measured using data collected in 2011. Also shown are the individual channel measurements in each bin with uncorrelated uncertainties and the pull from each point.


 (a)  $W^-$  (2011 measurement)

 (b)  $W^-$  (2010 measurement)

**Figure 9.9:** Combined differential  $d\sigma/d|\eta|$   $W^-$  cross section measured in 2011 (top) and 2010 (bottom). Also shown for the 2011 measurement are the individual channel measurements in each bin with uncorrelated uncertainties and the pull from each point.

(a)  $W^+$  (2011 measurement)(b)  $W^+$  (2010 measurement)

**Figure 9.10:** Combined differential  $d\sigma/d|\eta|$   $W^+$  cross section measured in 2011 (top) and 2010 (bottom). Also shown for the 2011 measurement are the individual channel measurements in each bin with uncorrelated uncertainties and the pull from each point.

$y_{min} - y_{max}$	$d\sigma/dy$ [pb]	$\delta_{stat.}, \%$	$\delta_{unc.}, \%$	$\delta_{cor.}, \%$	$\delta_{tot.}, \%$
0.00–0.40	3.52	0.93	0.55	1.19	1.61
0.40–0.80	3.51	0.92	0.52	1.11	1.54
0.80–1.20	3.42	0.95	0.48	1.24	1.63
1.20–1.60	3.43	1.00	0.47	1.16	1.60
1.60–2.00	3.31	1.09	0.45	1.10	1.61
2.00–2.40	3.35	1.60	0.59	1.04	2.00

**Table 9.3:** Combined differential cross section for the  $Z \rightarrow \ell\ell$  process  $d\sigma/d|y|$  measured for  $46 < M_{\ell\ell} < 66$  GeV and  $P_{t,\ell} > 20$  GeV.  $\delta_{stat}$ ,  $\delta_{unc}$ ,  $\delta_{corr}$  and  $\delta_{tot}$  represent statistical, uncorrelated systematic, correlated systematic and total uncertainties.

$y_{min} - y_{max}$	$d\sigma/dy$ [pb]	$\delta_{stat.}, \%$	$\delta_{unc.}, \%$	$\delta_{cor.}, \%$	$\delta_{tot.}, \%$
0.00–0.20	135.47	0.19	0.11	0.29	0.36
0.20–0.40	135.01	0.19	0.10	0.29	0.36
0.40–0.60	134.78	0.19	0.10	0.29	0.37
0.60–0.80	133.58	0.20	0.10	0.30	0.37
0.80–1.00	133.07	0.20	0.10	0.30	0.37
1.00–1.20	131.00	0.21	0.10	0.30	0.37
1.20–1.40	128.39	0.21	0.10	0.31	0.38
1.40–1.60	127.01	0.22	0.10	0.35	0.42
1.60–1.80	124.34	0.24	0.10	0.49	0.55
1.80–2.00	121.27	0.27	0.13	0.69	0.75
2.00–2.20	116.32	0.32	0.17	0.75	0.83
2.20–2.40	111.40	0.40	0.23	0.72	0.86
2.40–2.80	99.41	0.35	0.63	1.20	1.40
2.80–3.20	72.18	0.52	1.08	4.77	4.92
3.20–3.60	44.46	1.29	2.68	5.92	6.62

**Table 9.4:** Combined differential cross section for the  $Z \rightarrow \ell\ell$  process  $d\sigma/d|y|$  measured for  $66 < M_{\ell\ell} < 116$  GeV and  $P_{t,\ell} > 20$  GeV.  $\delta_{stat}$ ,  $\delta_{unc}$ ,  $\delta_{corr}$  and  $\delta_{tot}$  represent statistical, uncorrelated systematic, correlated systematic and total uncertainties.

$y_{min} - y_{max}$	$d\sigma/dy$ [pb]	$\delta_{stat.}, \%$	$\delta_{unc.}, \%$	$\delta_{cor.}, \%$	$\delta_{tot.}, \%$
0.00–0.40	1.52	1.33	0.63	1.00	1.78
0.40–0.80	1.47	1.38	0.64	0.94	1.79
0.80–1.20	1.43	1.48	0.67	0.96	1.89
1.20–1.60	1.45	1.51	0.68	0.93	1.90
1.60–2.00	1.31	2.00	0.89	0.90	2.36
2.00–2.40	1.22	2.92	1.62	1.26	3.57
2.40–2.80	0.98	4.23	3.16	3.75	6.48
2.80–3.20	0.69	5.73	3.13	6.18	8.99
3.20–3.60	0.20	16.96	11.90	12.57	24.23

**Table 9.5:** Combined differential cross section for the  $Z \rightarrow \ell\ell$  process  $d\sigma/d|y|$  measured for  $116 < M_{\ell\ell} < 150$  GeV and  $P_{t,\ell} > 20$  GeV.  $\delta_{stat.}$ ,  $\delta_{unc.}$ ,  $\delta_{corr.}$  and  $\delta_{tot.}$  represent statistical, uncorrelated systematic, correlated systematic and total uncertainties.

$\eta_{min} - \eta_{max}$	$d\sigma/dy$ [pb]	$\delta_{stat.}, \%$	$\delta_{unc.}, \%$	$\delta_{cor.}, \%$	$\delta_{tot.}, \%$
0.00–0.21	437.98	0.13	0.32	0.50	0.60
0.21–0.42	435.89	0.11	0.41	0.40	0.58
0.42–0.63	430.34	0.12	0.21	0.46	0.52
0.63–0.84	425.37	0.14	0.27	0.53	0.61
0.84–1.05	414.89	0.13	0.24	0.46	0.53
1.05–1.37	407.74	0.09	0.18	0.49	0.53
1.37–1.52	389.00	0.17	0.26	0.55	0.63
1.52–1.74	379.91	0.13	0.36	0.60	0.71
1.74–1.95	366.74	0.14	0.24	0.63	0.69
1.95–2.18	344.49	0.14	0.25	0.70	0.76
2.18–2.50	318.40	0.15	0.45	0.78	0.92

**Table 9.6:** Combined differential cross section for the  $W^- \rightarrow \ell^- \bar{\nu}$   $d\sigma/d|\eta|$  measured for  $p_{t,\ell} > 20$  GeV,  $P_{t,\nu} > 25$  GeV and  $M_t > 40$  GeV.  $\delta_{stat.}$ ,  $\delta_{unc.}$ ,  $\delta_{corr.}$  and  $\delta_{tot.}$  represent statistical, uncorrelated systematic, correlated systematic and total uncertainties.

$\eta_{min} - \eta_{max}$	$d\sigma/dy$ [pb]	$\delta_{stat.}, \%$	$\delta_{unc.}, \%$	$\delta_{cor.}, \%$	$\delta_{tot.}, \%$
0.00–0.21	579.69	0.11	0.32	0.47	0.58
0.21–0.42	580.95	0.09	0.32	0.42	0.53
0.42–0.63	581.92	0.10	0.21	0.45	0.51
0.63–0.84	586.88	0.12	0.25	0.48	0.55
0.84–1.05	588.24	0.09	0.25	0.43	0.51
1.05–1.37	601.59	0.07	0.15	0.48	0.51
1.37–1.52	598.94	0.13	0.23	0.57	0.63
1.52–1.74	606.64	0.10	0.24	0.53	0.59
1.74–1.95	602.90	0.09	0.39	0.51	0.65
1.95–2.18	595.49	0.08	0.41	0.55	0.69
2.18–2.50	561.88	0.10	0.51	0.60	0.79

**Table 9.7:** Combined differential cross section for the  $W^+ \rightarrow \ell^+\nu$   $d\sigma/d|\eta|$  measured for  $p_{t,\ell} > 20$  GeV,  $P_{t,\nu} > 25$  GeV and  $M_t > 40$  GeV.  $\delta_{stat.}$ ,  $\delta_{unc.}$ ,  $\delta_{corr.}$  and  $\delta_{tot.}$  represent statistical, uncorrelated systematic, correlated systematic and total uncertainties.

### 9.2.1 Combined Cross Section Results Compared to Theoretical Predictions

The combined data are compared to NNLO QCD + NLO EWK predictions as the mass-differential electron data were in Sec. 8.1. The same predictions listed in that section are used.

The combined  $d\sigma/dm_Z$  cross section measurement is compared to theory in Fig. 9.11. As for the comparison with the electron data in Sec. 8.1, the ATLAS epWZ and ABM11 fits show the best description of the combined data, but the shape is not in good agreement. The second and final bins are particularly poorly described by all PDF fits.

The ATLAS epWZ fit is a fit to the 2010 inclusive W,Z inclusive data. The fit suggests enhanced strangeness in the proton w.r.t. to the  $d$  sea [75]. The comparison of  $d\sigma/d|y_Z|$  distribution in the  $66 < m_Z < 116$  GeV region with this fit is shown in Fig. 9.12 (left). There is good agreement in particular in the central region of  $|y_Z| < 2.5$ , indicating that the new data support the observation of enhanced strangeness.

The data in the low ( $46 < m_Z < 66$  GeV) and high ( $116 < m_Z < 150$  GeV) mass bins do not show good agreement with the ATLAS epWZ fit or any other fit, as can be seen in Figs. 9.13 and 9.14 respectively.

ABM11 provides a reasonable description of the  $W^-$  data as can be seen in Fig. 9.15 (left), but overshoots the data for  $|\eta_l| < 1$ . The opposite behaviour is observed for HERAPDF1.5 which describes the data within uncertainties in this region, but overshoots it at higher  $|\eta_l|$ .

The  $W^+$  data in Fig. 9.15 (right) is also described by HERAPDF1.5 within uncertainties, as well as CT10.

In all regions, the JR09 fit shows the worst agreement with the combined data.

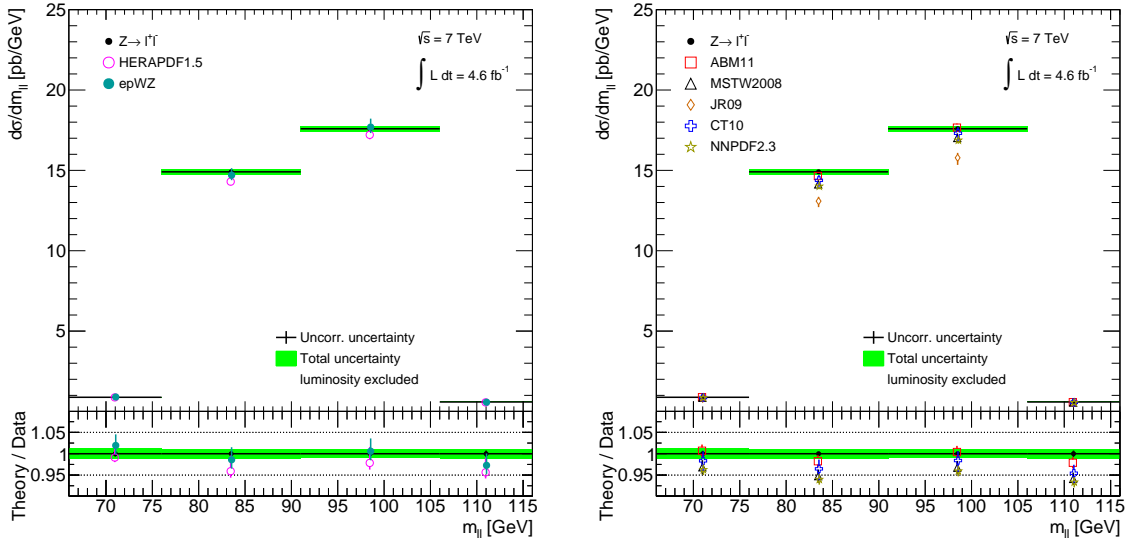


**Figure 9.11:** Combined  $Z \rightarrow \ell\ell$  cross section as a function of di-electron invariant mass in the region  $66 < m_Z < 116$  GeV compared to NNLO QCD predictions with NLO EW corrections based on various NNLO PDFs.

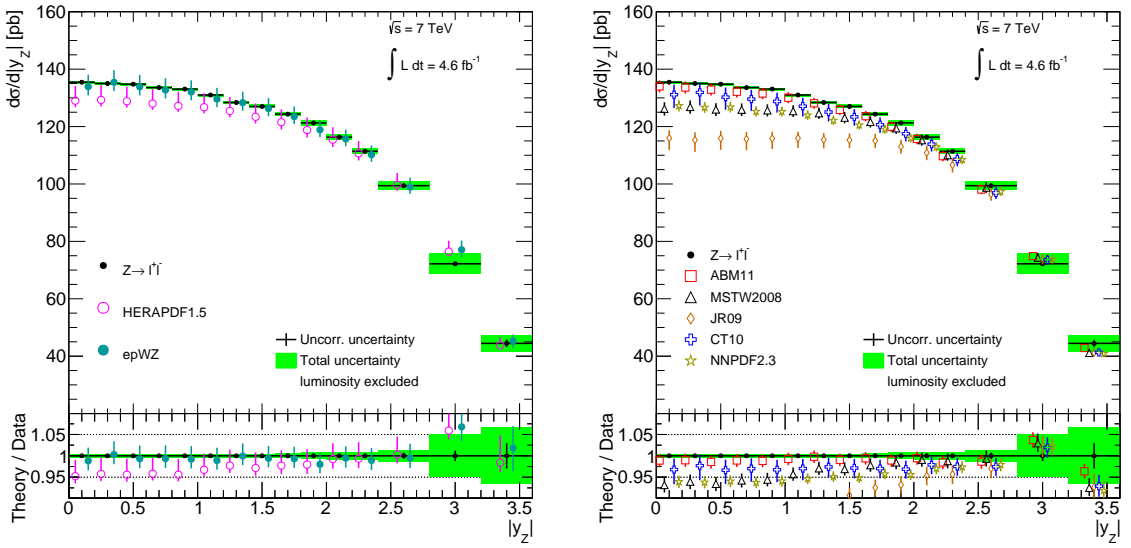


**Figure 9.12:** Combined  $Z \rightarrow \ell\ell$  cross section as a function of  $Z$  boson rapidity in the region  $66 < m_Z < 116$  GeV compared to NNLO QCD predictions with NLO EW corrections based on various NNLO PDFs.

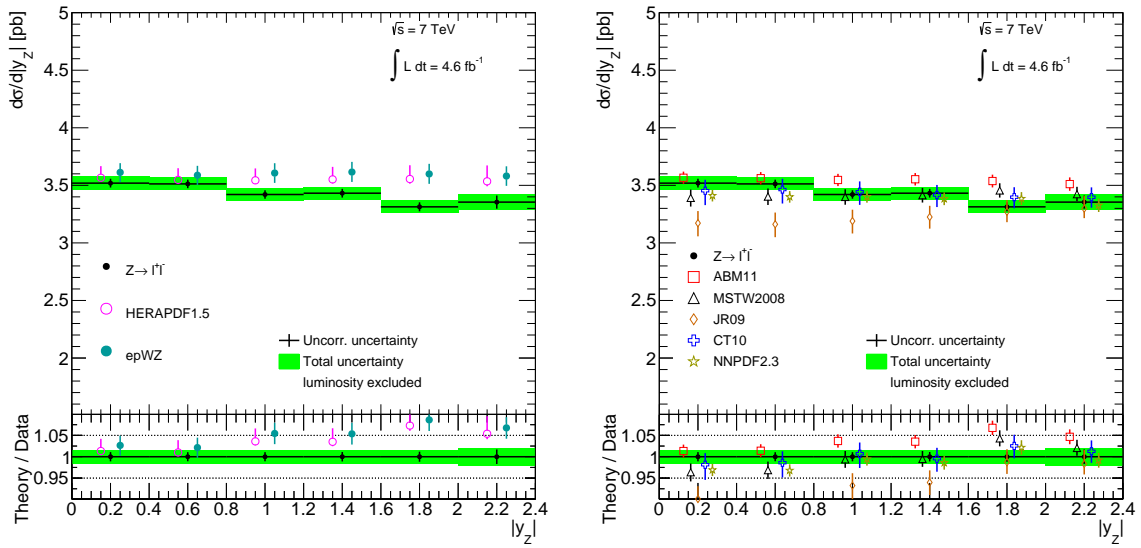


**Figure 9.13:** Combined  $Z \rightarrow \ell\ell$  cross section as a function of  $Z$  boson rapidity in the region  $46 < m_Z < 66$  GeV compared to NNLO QCD predictions with NLO EW corrections based on various NNLO PDFs.

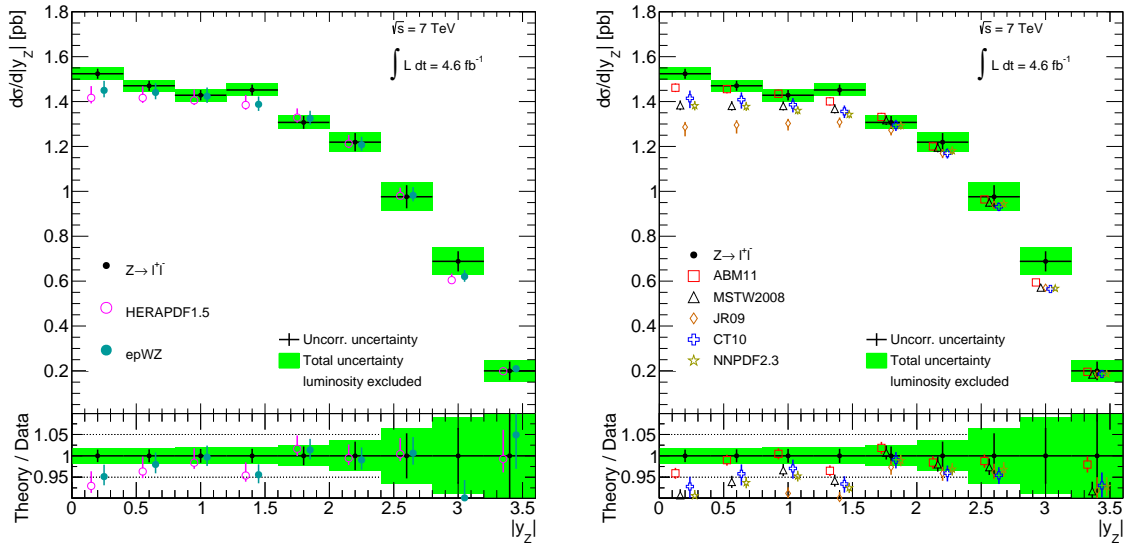


**Figure 9.14:** Combined  $Z \rightarrow \ell\ell$  cross section as a function of  $Z$  boson rapidity in the region  $116 < m_Z < 150$  GeV compared to NNLO QCD predictions with NLO EW corrections based on various NNLO PDFs.

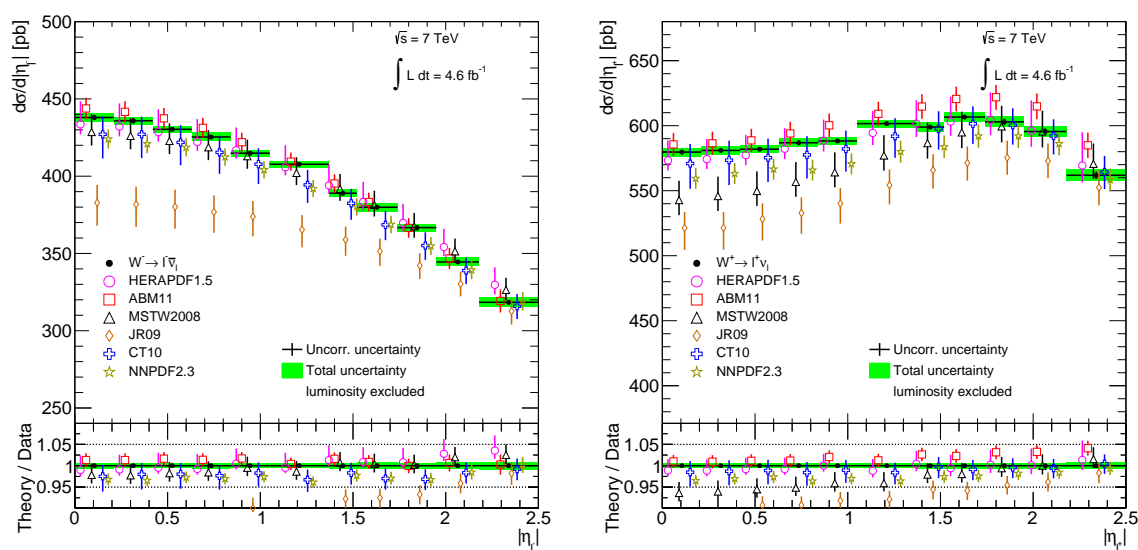


**Figure 9.15:** Combined  $W^-$  (left) and  $W^+$  (right) cross sections as a function of lepton pseudo-rapidity compared to NNLO QCD predictions with NLO EW corrections based on various NNLO PDFs.

## 10 Combined ATLAS $Z/\gamma^* \rightarrow \ell\ell$ Cross Section vs. $m_{\ell\ell}$

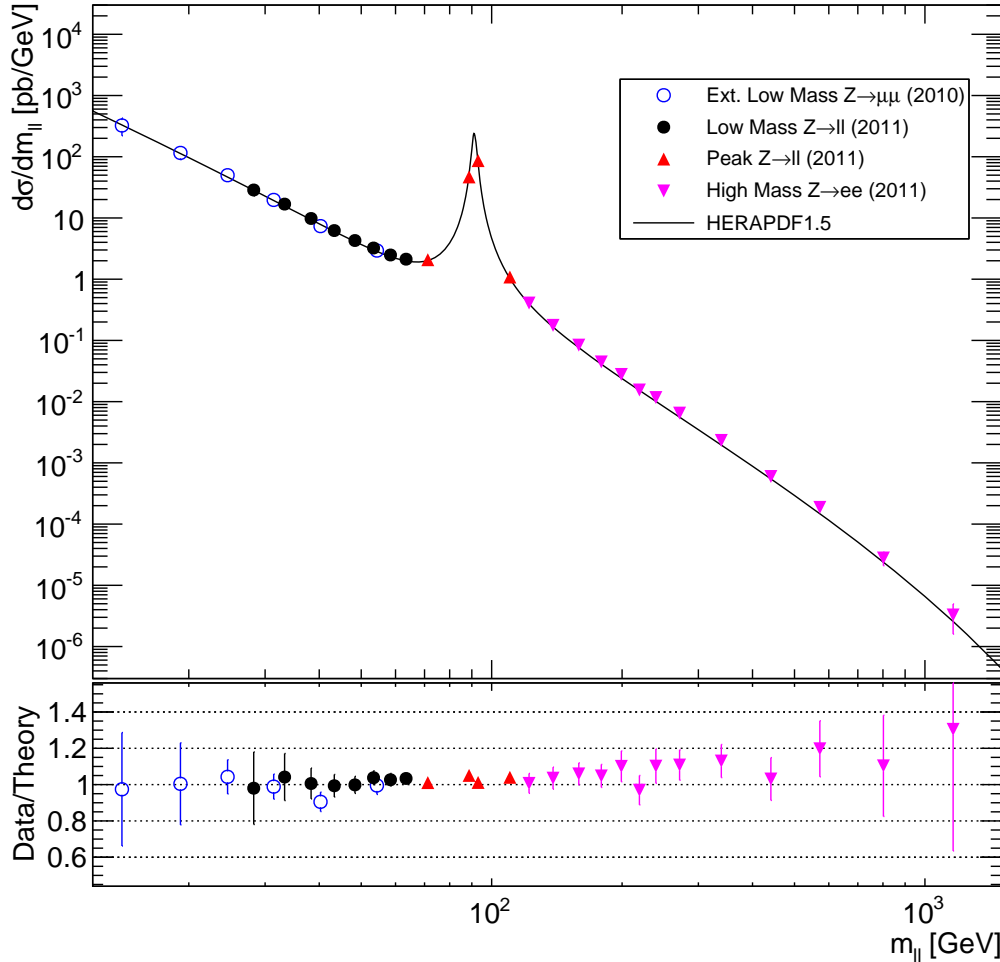


**Figure 10.1:** Differential cross section as a function of,  $m_{\ell\ell}$  for the neutral current process,  $Z/\gamma^* \rightarrow \ell\ell$ . The line shape measurement is displayed as red triangles.

The combined  $d\sigma/dm_Z$  data are extrapolated to the total cross sections (i.e. no selection cuts apart from di-electron mass) by an acceptance factor,  $A_Z$  as described by Eqn. 5.4. These factors and their associated uncertainties were calculated in the same way as for the  $E_Z$  factors listed in Sec. 8.1.

The acceptance factors are listed in Tab. 10.1 and shown in Fig. 10.2.

$m_Z$ [GeV]	$A_Z$	$\Delta_{\text{CT10}}[\%]$	$\Delta_{\text{PDFmax}}[\%]$	$\Delta_{\text{ME}}[\%]$	$\Delta_{\text{PS}}[\%]$	$\Delta_{\text{tot}}[\%]$
$66.00 < m_Z < 76.00$	0.4096	0.91	-0.53	-0.27	-0.83	1.37
$76.00 < m_Z < 91.00$	0.5008	0.86	0.91	-0.61	-0.78	1.59
$91.00 < m_Z < 106.00$	0.5159	0.83	0.92	-0.17	-0.74	1.46
$106.00 < m_Z < 116.00$	0.5551	0.72	0.80	-0.24	-0.54	1.23

**Table 10.1:**  $A_Z$  factors and associated uncertainties in bins of invariant mass.

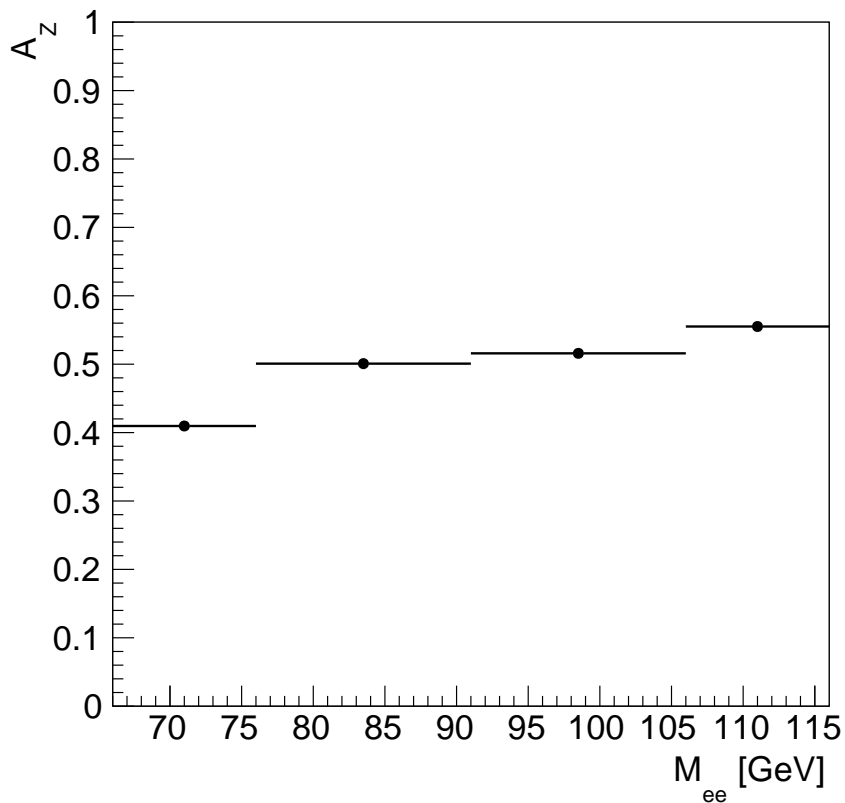


**Figure 10.2:**  $A_Z$  factors in bins of invariant mass used to extrapolate the experimental measurement to a different phase space for comparison with theoretical predictions.

The full spectrum of the differential cross section as a function of mass in the range up to 1500 GeV can be seen in Fig. 10.1. This plot combines data from low- and high-mass Drell-Yan measurements with the line shape measurement in the peak region, 66 – 116 GeV from this analysis.

There is also an extended low mass measurement of the  $Z \rightarrow \mu\mu$  cross section using 35  $\text{pb}^{-1}$  of data collected in 2010.

The theoretical prediction was calculated using the Vrap [81] program which can be used to produce LO, NLO, and NNLO cross section predictions for lepton-pair-production processes.

A correction is applied to obtain the differential measurement in each bin from the value integrated over the bin. The correction takes the theoretical differential cross section at the centre of the bin divided by the theoretical differential cross integrated over the bin. This correction factor is then applied to the measured value in each bin. In this case, the centre of the bin is taken to be the mean of the distribution in that bin.

$$\delta_{BC} = \frac{\frac{d\sigma^{theory}}{dM_{ee}}(\text{bin centre})}{\int_{low}^{high} \frac{d\sigma^{theory}}{dM_{ee}}} \quad (10.1)$$

## 11 Summary

A measurement of the differential  $Z \rightarrow ee$  cross section as function of di-electron invariant mass using  $4.58 \text{ fb}^{-1}$  of data collected in 2011 with the ATLAS detector at the LHC was performed. This measurement expands upon previously published data from ATLAS that measured the inclusive  $Z/\gamma^*$  cross section as a function of the  $Z$  boson rapidity using  $36 \text{ pb}^{-1}$  of data collected in 2010. The increased statistics allowed for an introduction of the cross section measurement in a new dimension: invariant mass.

The total systematic uncertainty on the cross section is within 2%, and a detailed treatment of the full set of uncertainty sources has been described. QCD background can't be estimated using simulation for practical reasons, and its estimation using data-driven techniques introduces uncertainties into the cross section measurement which were explained in detail.

A comparison with different theoretical predictions from various NNLO QCD fits with NLO EWK correction validated the hypothesis that a precision measurement allows discrimination between the different PDFs. It is seen that the NNLO QCD and NLO EWK theory are limiting factors in the interpretation of the data and in this way the measurement can be used to probe QCD and determine PDFs.

In addition to the  $d\sigma/dm_Z$  cross section measurement in the electron channel, a combination of this cross section with a measurement in the muon channel. Also combined were separately measured electron and muon  $d\sigma/d|y_Z| Z$  and  $d\sigma/d|\eta| W^\pm$  cross sections.

The measurements were extrapolated to a common electron and muon phase space and then combined in a linear averaging procedure that accounts for the uncertainties from each channel and the correlations between them.

Tension is observed with the forward electron data but the central electron cross sections are in reasonable agreement with the muons. The combined data in the peak  $Z$  mass region  $66 < m_Z < 116 \text{ GeV}$ , as well as the separately combined  $W^+$  and  $W^-$  data are compared with previous measurements in the same regime. As expected with increased statistics and more mature analysis techniques, a significant improvement in the precision of the measurements is observed.

These combined measurements are also compared against various NNLO QCD + NLO EWK fits resulting in strong PDF discrimination. The measurement precision is better than the PDF uncertainties in almost all of the measurement bins. The combined data can be used to inform PDFs in future NNLO QCD calculations.

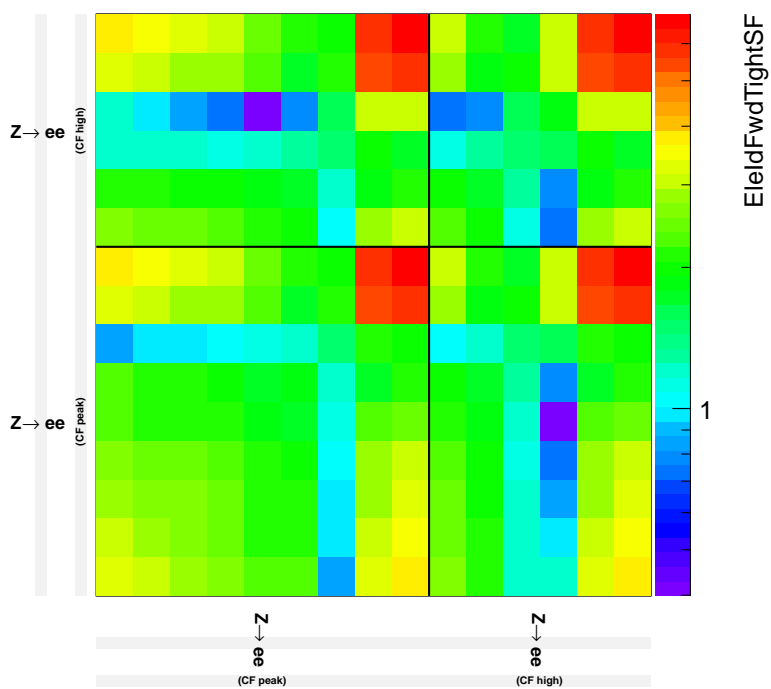
Finally the total  $d\sigma/dm_Z$  cross section measurement is concurrently compared to a theoretical prediction with low and high mass Drell-Yan data measured in ATLAS. The data show good agreement to the NNLO QCD-calculated prediction.

## A Covariance of correlated systematic uncertainty sources

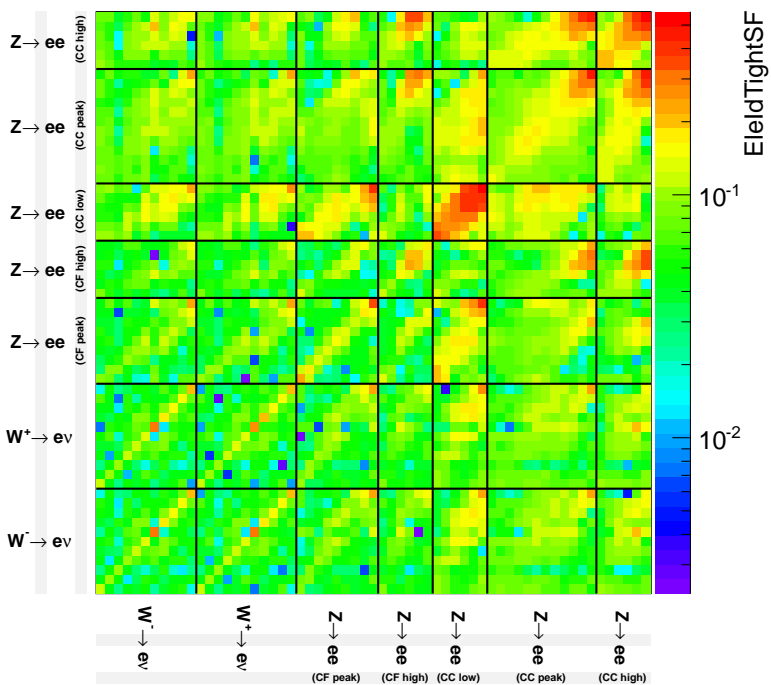
In addition to the correlation matrices shown in Sec. 9.1, covariance matrices are built. To illustrate the covariance more clearly, it is shown in terms of square-root percentage fraction of the average cross section in each cell, i.e. for cell  $i, j$ :

$$\sqrt{\frac{\text{cov}(i, j)}{\sigma_i \sigma_j}} \quad (\text{A.1})$$

where  $\sigma_{i(j)}$  is the average cross section in cell  $i(j)$  across all Toy MC replicas. These matrices are shown in Figs A.1-A.5.

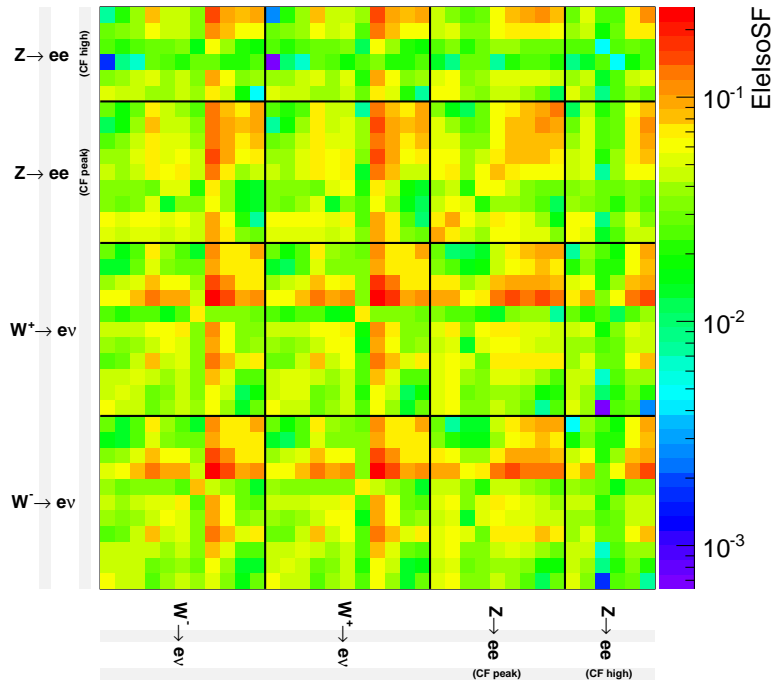


(a) Forward electron ID scale factor uncertainty

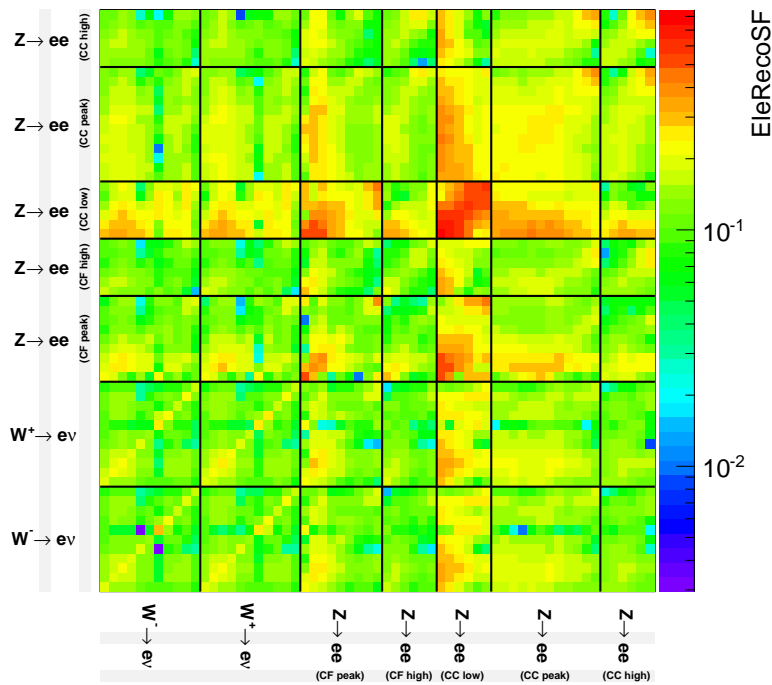


(b) Electron ID scale factor uncertainty

**Figure A.1:** Bin-to-bin covariance across all measurements for the systematic uncertainties from the forward electron ID scale factor (top), and the electron ID scale factor (bottom).

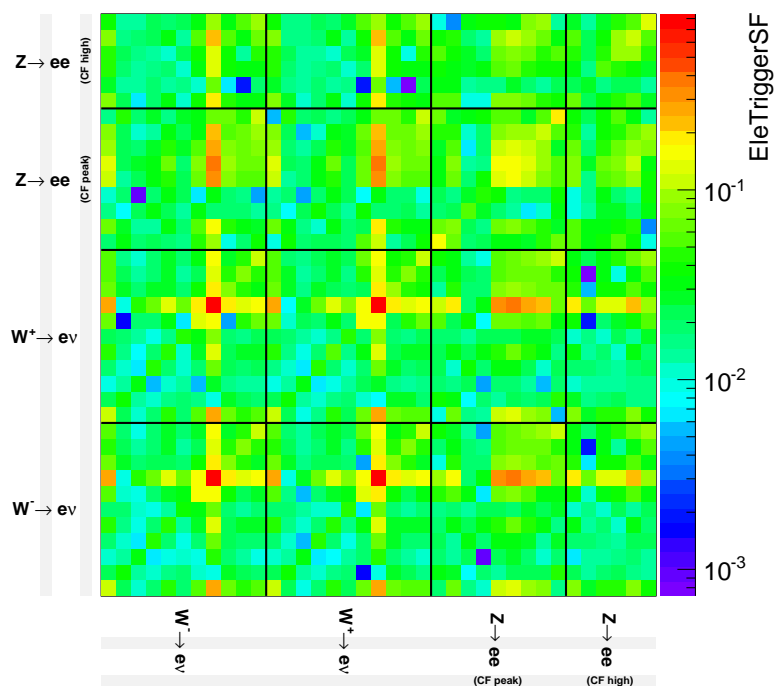


(a) Electron isolation scale factor uncertainty

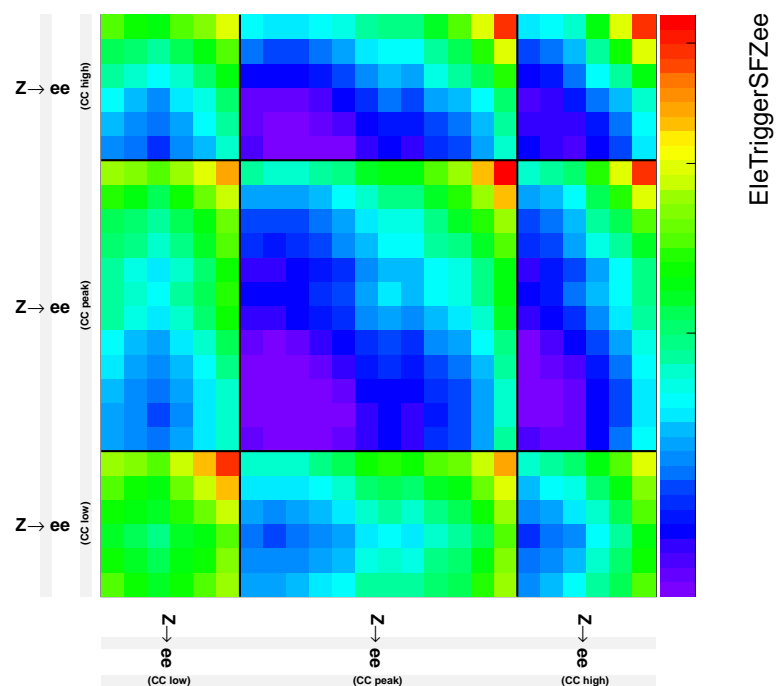


(b) Electron reconstruction scale factor uncertainty

**Figure A.2:** Bin-to-bin covariance across all measurements for the systematic uncertainties from the electron isolation scale factor (top), and the electron reconstruction scale factor (bottom).

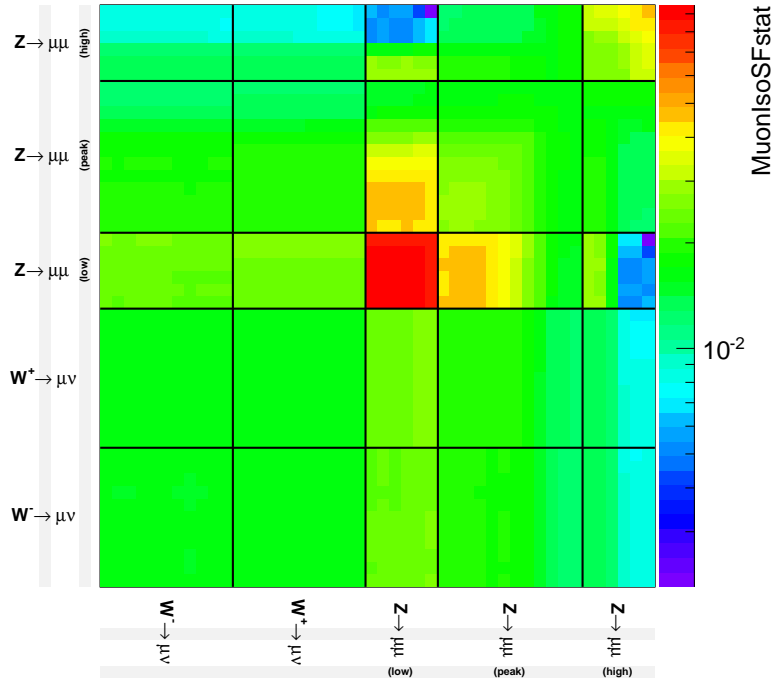


(a) Single electron trigger scale factor uncertainty

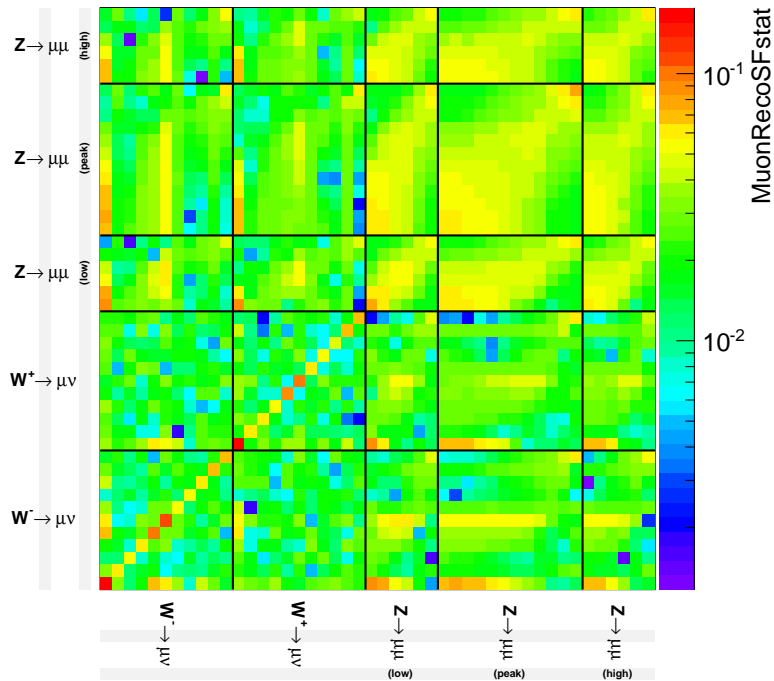


(b) Di-electron trigger scale factor uncertainty (stat.)

**Figure A.3:** Bin-to-bin covariance across all measurements for the systematic uncertainties from the single electron trigger scale factor (top), and the statistical component of the di-electron trigger scale factor (bottom).

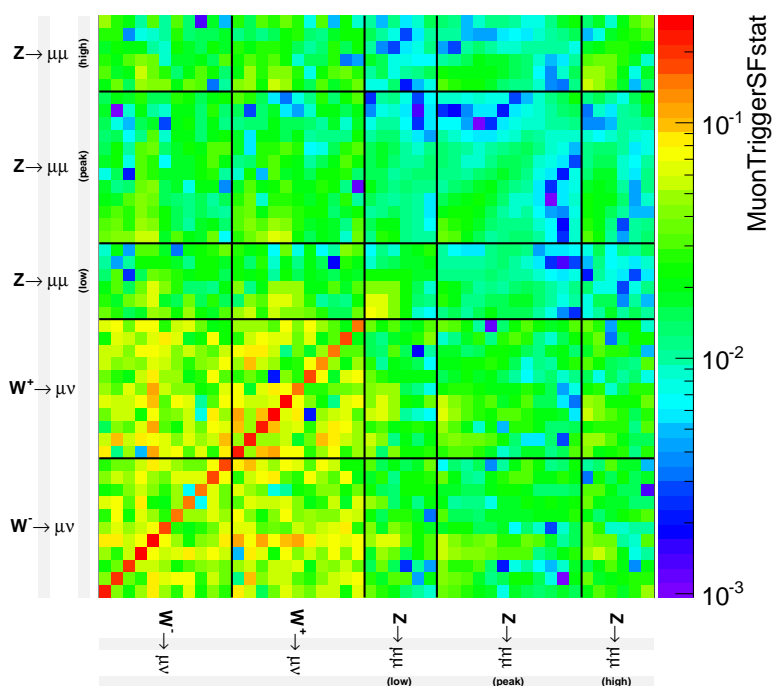


(a) Muon isolation scale factor uncertainty (stat.)



(b) Muon reconstruction scale factor uncertainty (stat.)

**Figure A.4:** Bin-to-bin covariance across all measurements for the systematic uncertainties from the statistical components of the muon isolation scale factor (top), and the muon reconstruction scale factor (bottom).

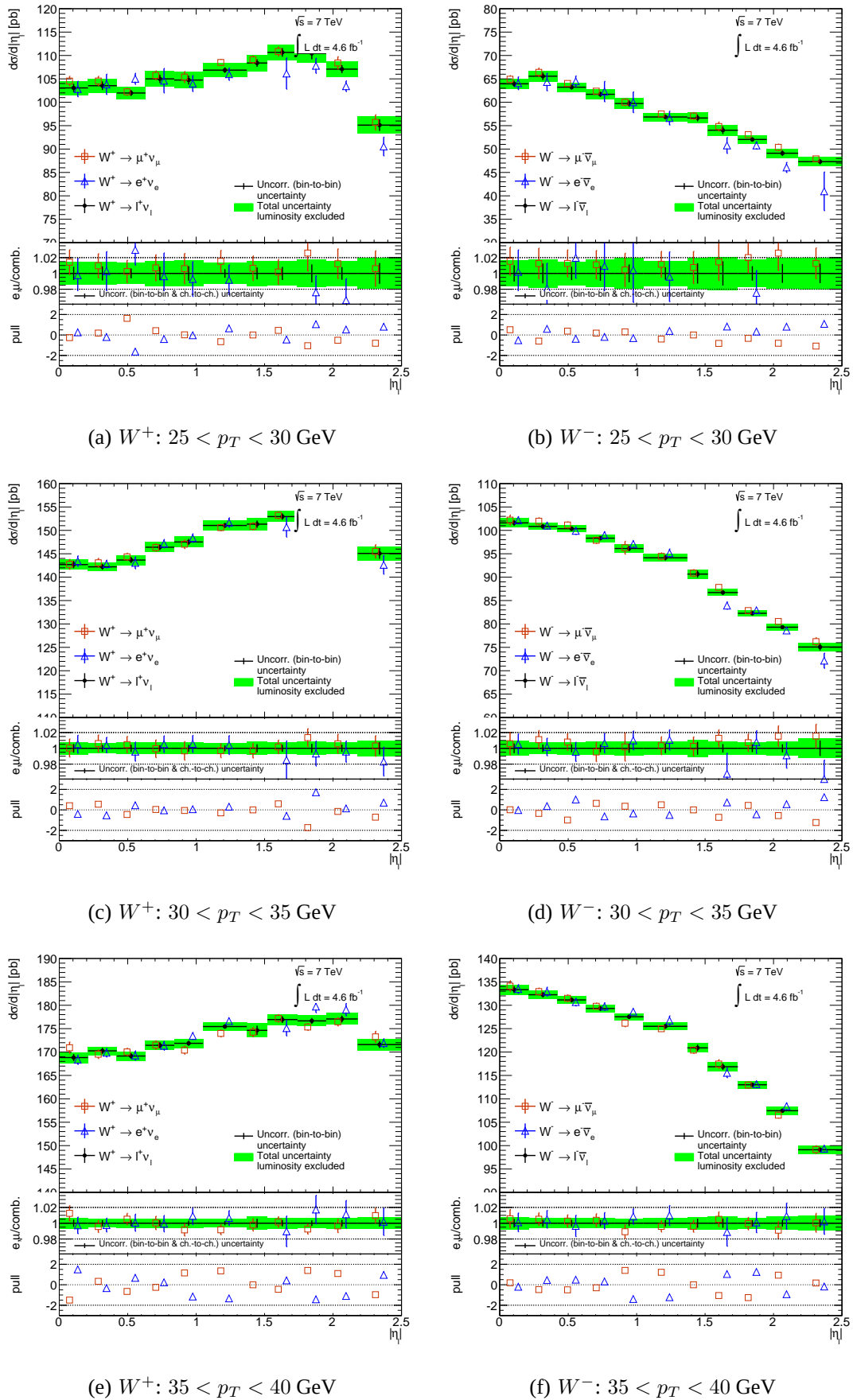


(a) Muon trigger scale factor uncertainty (stat.)

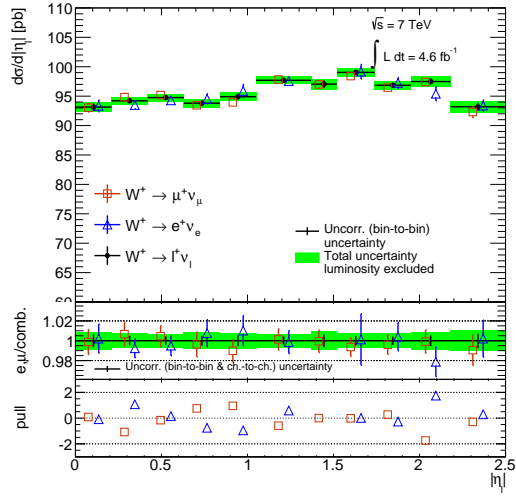
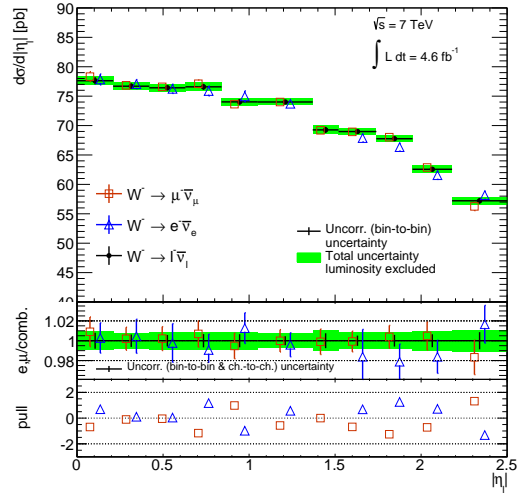
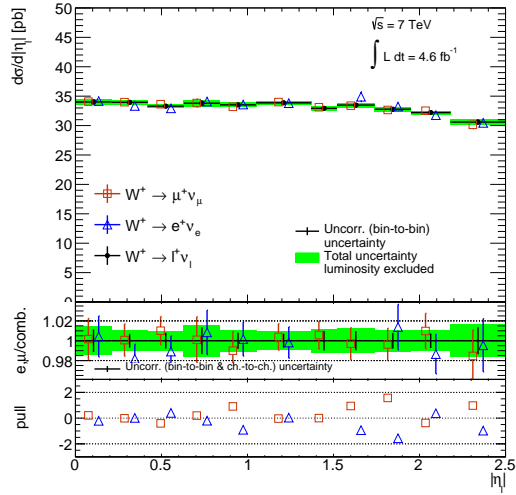
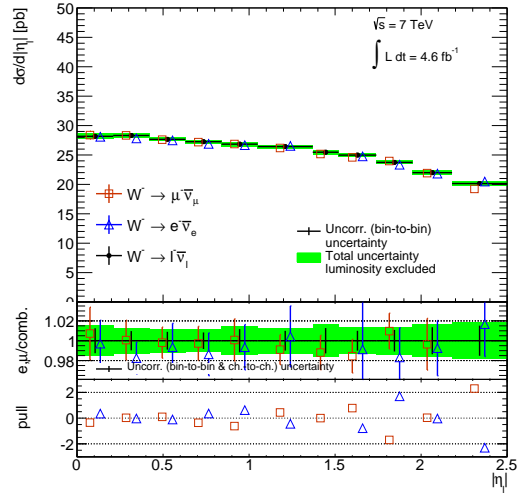
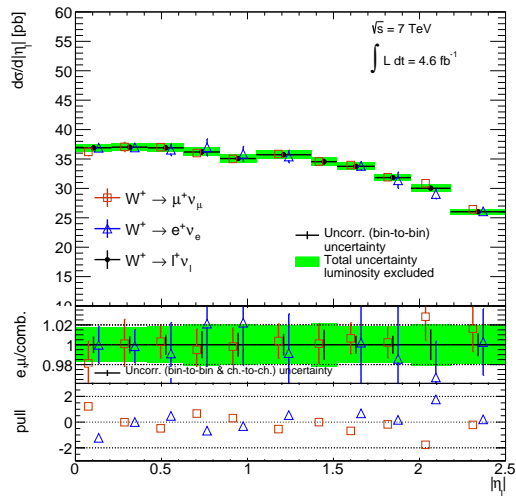
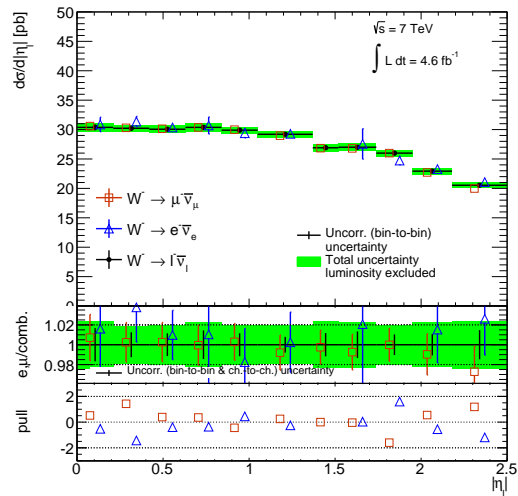
**Figure A.5:** Bin-to-bin covariance across all measurements for the systematic uncertainties from the statistical components of the muon trigger scale factor.

## B Combination of Double Differential Cross Sections

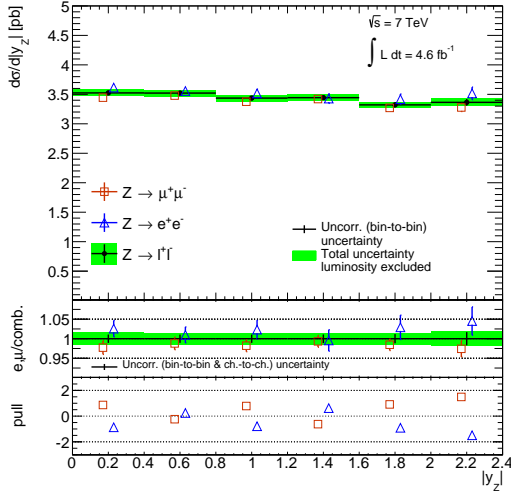
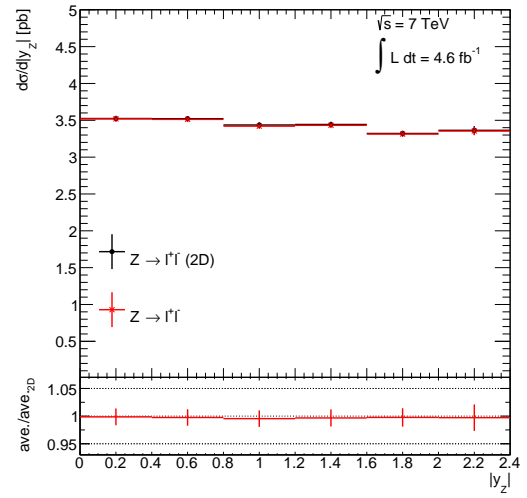
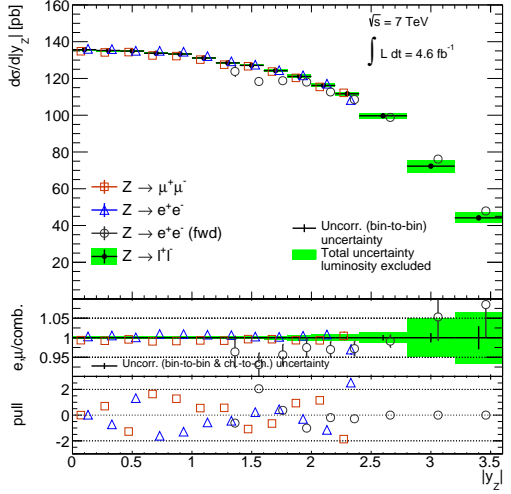
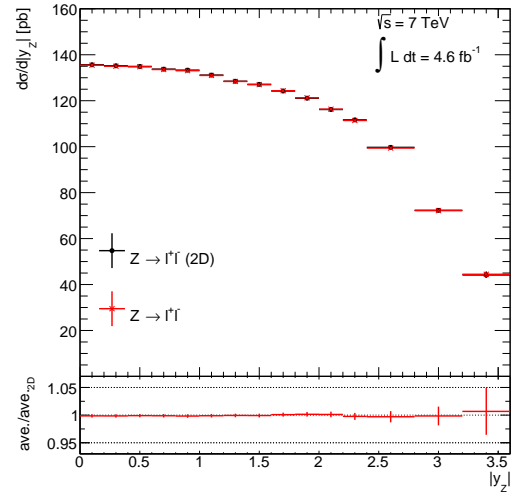
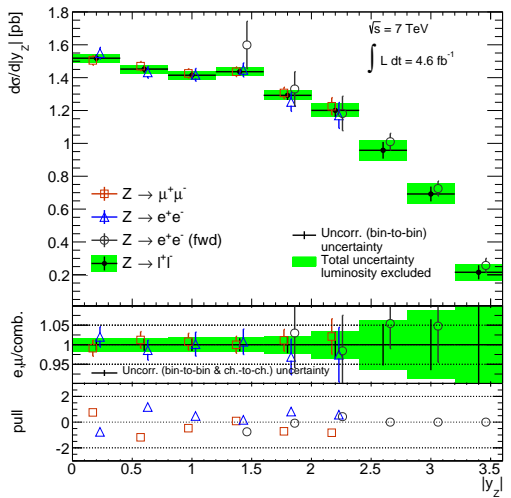
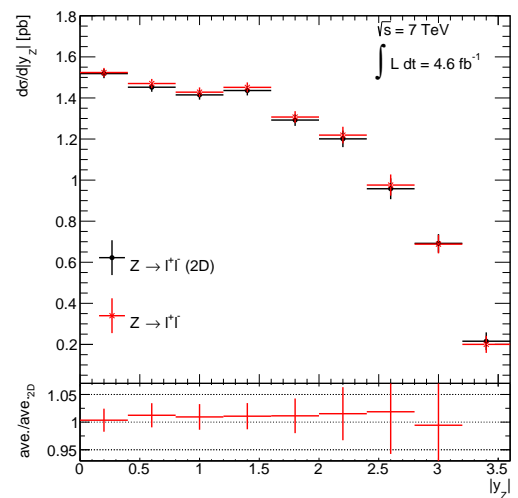
This section contains the results from the combination of the single differential  $d\sigma/dy$  cross sections from  $Z$  with the double differential  $d\sigma/d|\eta| dp_{T,\ell}$  cross sections from  $W$ . The combined 2D measurements are in good agreement with  $\chi^2/d.o.f. = 144.15/153$ . The combination was performed over all measurements simultaneously.



**Figure B.1:** Combination double-differential  $d\sigma/d|\eta| dp_{T,\ell}$  cross section measurements for  $W^+$  (left) and  $W^-$  (right). Also shown are the measurements in each bin with uncorrelated uncertainties.

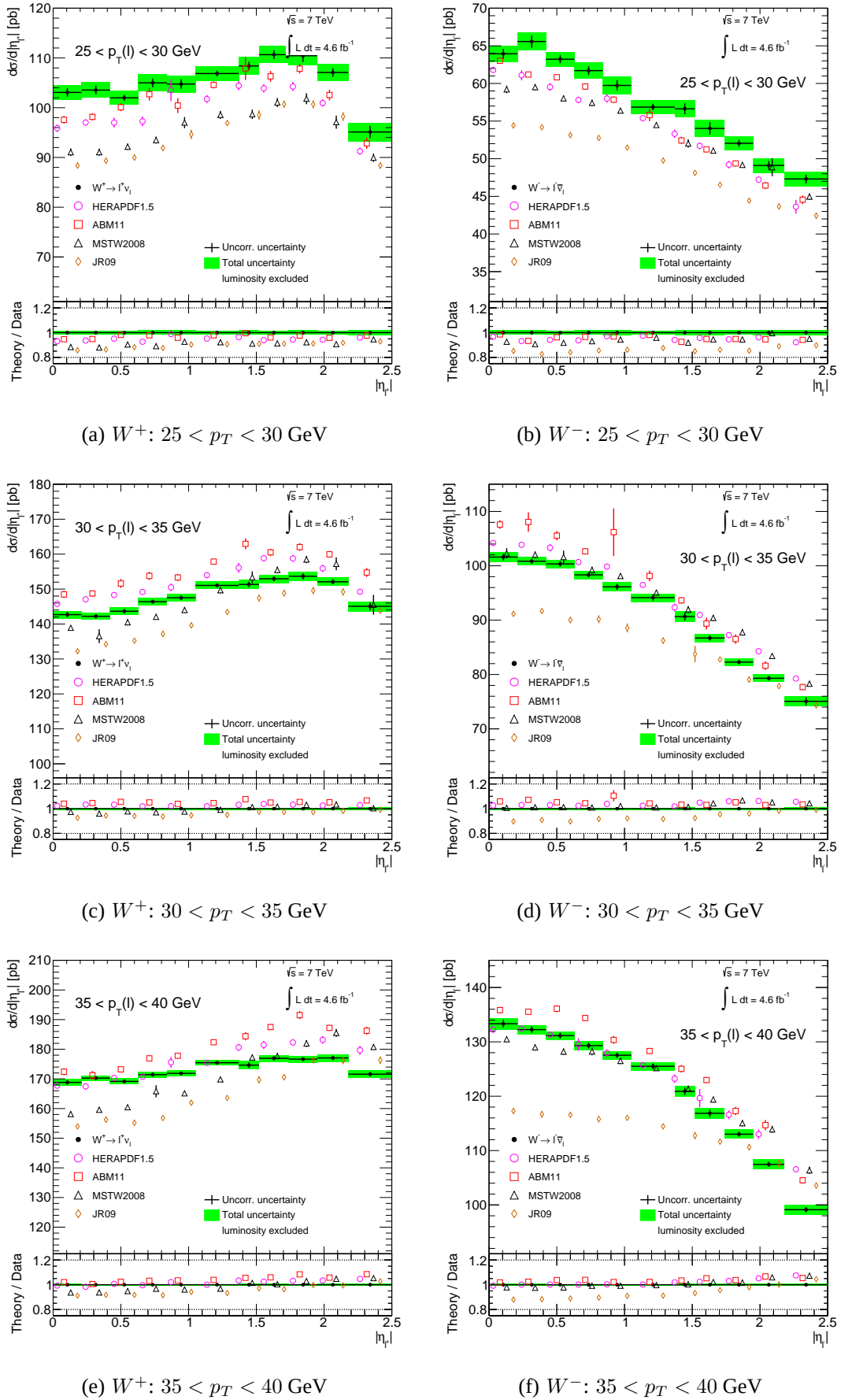
(a)  $W^+$ :  $40 < p_T < 45$  GeV(b)  $W^-$ :  $40 < p_T < 45$  GeV(c)  $W^+$ :  $45 < p_T < 50$  GeV(d)  $W^-$ :  $45 < p_T < 50$  GeV(e)  $W^+$ :  $p_T > 50$  GeV(f)  $W^-$ :  $p_T > 50$  GeV

**Figure B.2:** Combination double-differential  $d\sigma/d|\eta| dp_{T,\ell}$  cross section measurements for  $W^+$  (left) and  $W^-$  (right).

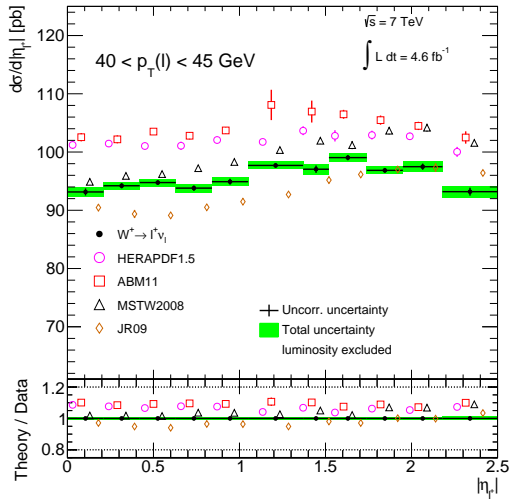
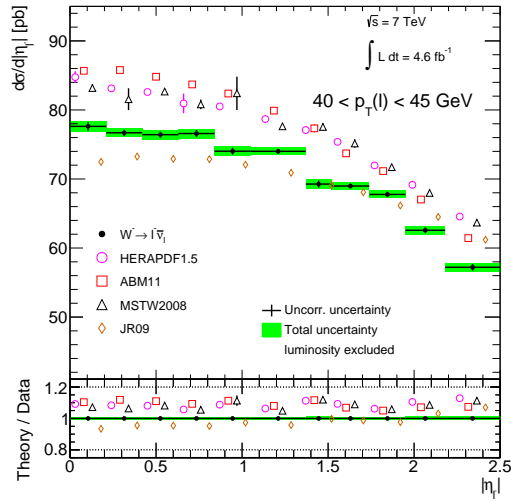
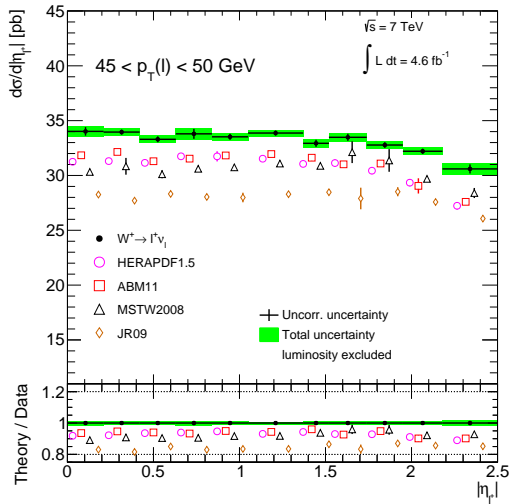
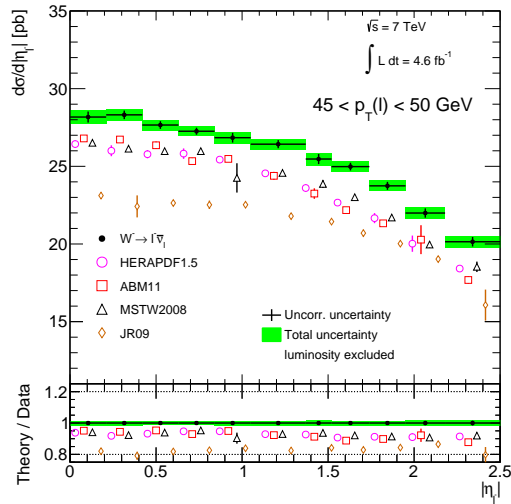
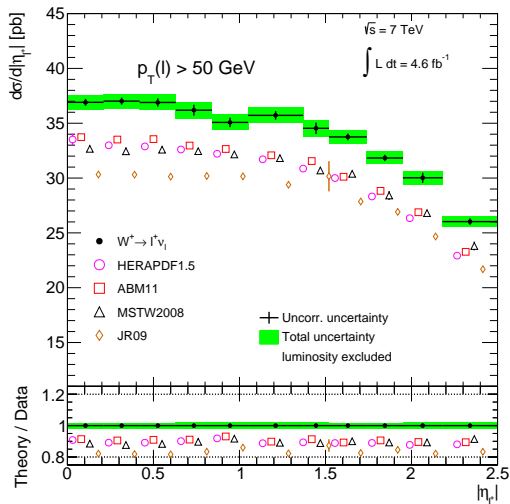
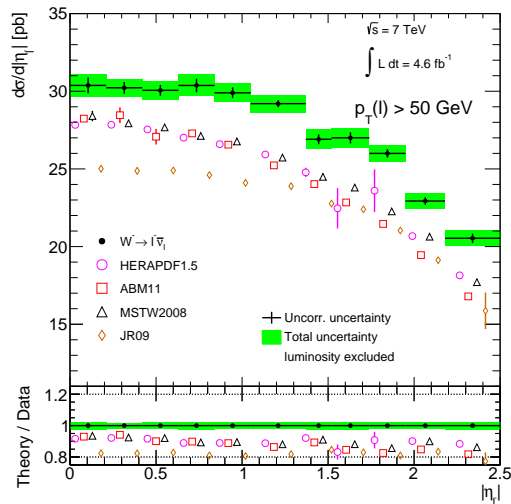
(a)  $Z: 46 < m_{\ell\ell} < 66$  GeV(b)  $Z: 46 < m_{\ell\ell} < 66$  GeV(c)  $Z: 66 < m_{\ell\ell} < 116$  GeV(d)  $Z: 66 < m_{\ell\ell} < 116$  GeV(e)  $Z: 116 < m_{\ell\ell} < 150$  GeV(f)  $Z: 116 < m_{\ell\ell} < 150$  GeV

**Figure B.3:** Combined differential  $d\sigma/d|y_Z|$  cross section measurements when combined with  $d\sigma/d|\eta_{\ell}| dp_{T,\ell}$  (left) and their comparison to the measurements combined with  $d\sigma/d|\eta_{\ell}|$  (right).

## **B.1 Combined Double Differential Cross Section Results Compared to Theoretical Predictions**



**Figure B.4:** Combination double-differential  $d\sigma/d|\eta_l| dp_{T,\ell}$  cross section measurements for  $W^+$  (left) and  $W^-$  (right). Also shown are the measurements in each bin with uncorrelated uncertainties.

(a)  $W^+$ :  $40 < p_T < 45$  GeV(b)  $W^-$ :  $40 < p_T < 45$  GeV(c)  $W^+$ :  $45 < p_T < 50$  GeV(d)  $W^-$ :  $45 < p_T < 50$  GeV(e)  $W^+$ :  $p_T > 50$  GeV(f)  $W^-$ :  $p_T > 50$  GeV

**Figure B.5:** Combination double-differential  $d\sigma/d|\eta_l| dp_{T,\ell}$  cross section measurements for  $W^+$  (left) and  $W^-$  (right).

## C Phase Space Definitions

Listed here is the  $W \rightarrow \ell\nu$  experimental phase space in Tab. C.1, and the combined measurements in Tab. C.2.

$W \rightarrow e\nu$ Experimental Phase Space	
Integrated	<ul style="list-style-type: none"> <li>• Separately <math>W^+</math>, <math>W^-</math> and <math>W^+ + W^-</math></li> <li>• <math>p_{T,e} &gt; 25</math> GeV</li> <li>• <math> \eta  &lt; 2.47</math> excluding <math>1.37 &lt;  \eta  &lt; 1.52</math></li> <li>• Additionally excluding <math>1.6 &lt;  \eta  &lt; 1.7</math></li> <li>• <math>p_{T,\nu} &gt; 25</math> GeV</li> <li>• <math>m_T &gt; 40</math> GeV</li> </ul>
Differential	<ul style="list-style-type: none"> <li>• Separately <math>W^+</math> and <math>W^-</math></li> <li>• <math>p_{T,\nu} &gt; 25</math> GeV</li> <li>• <math>m_T &gt; 40</math> GeV</li> <li>• Additionally excluding <math>1.6 &lt;  \eta  &lt; 1.7</math></li> <li>• <math>d\sigma/d \eta_\ell </math> in 10 <math> \eta_\ell </math> bins for <math>p_{T,e} &gt; 25</math> GeV: <math> \eta_\ell  : 0.0, 0.21, 0.42, 0.63, 0.84, 1.05, 1.37 - 1.52, 1.74, 1.95, 2.18, 2.47</math></li> <li>• <math>d\sigma/d \eta_\ell  dp_{T,e}</math> in <math>10 \times 7</math> <math> \eta_\ell  \times p_{T,e}</math> bins: <math> \eta_\ell  : 0.0, 0.21, 0.42, 0.63, 0.84, 1.05, 1.37 - 1.52, 1.74, 1.95, 2.18, 2.47</math> <math>p_{T,e} : 25, 30, 35, 40, 45, 50, \infty</math> [ GeV ]</li> </ul>
$W \rightarrow \mu\nu$ Experimental Phase Space	
Integrated	<ul style="list-style-type: none"> <li>• Separately <math>W^+</math>, <math>W^-</math> and <math>W^+ + W^-</math></li> <li>• <math> \eta  &lt; 2.4</math></li> <li>• <math>p_{T,\nu} &gt; 25</math> GeV</li> <li>• <math>m_T &gt; 40</math> GeV</li> <li>• <math>p_{T,e} &gt; 25</math> GeV</li> </ul>
Differential	<ul style="list-style-type: none"> <li>• Separately <math>W^+</math> and <math>W^-</math></li> <li>• <math>p_{T,\nu} &gt; 25</math> GeV</li> <li>• <math>m_T &gt; 40</math> GeV</li> <li>• <math>d\sigma/d \eta_\ell </math> in 11 <math> \eta_\ell </math> bins: <math> \eta_\ell  : 0.0, 0.21, 0.42, 0.63, 0.84, 1.05, 1.37, 1.52, 1.74, 1.95, 2.18, 2.4</math></li> <li>• <math>d\sigma/d \eta_\ell  dp_{T,e}</math> in <math>11 \times 7</math> <math> \eta_\ell  \times p_{T,e}</math> bins for <math>p_{T,e} &gt; 20</math> GeV: <math> \eta_\ell  : 0.0, 0.21, 0.42, 0.63, 0.84, 1.05, 1.37, 1.52, 1.74, 1.95, 2.18, 2.4</math> <math>p_{T,e} : 20, 25, 30, 35, 40, 45, 50, \infty</math> [ GeV ]</li> </ul>

**Table C.1:** Complete list of experimental measurements considered in the  $W \rightarrow e\nu$  and  $W \rightarrow \mu\nu$  channels.

Combined Integrated $W \rightarrow \ell\nu$									
Fiducial	<ul style="list-style-type: none"> <li>• Separately <math>W^+</math>, <math>W^-</math> and <math>W^+ + W^-</math></li> <li>• <math>p_{T,\nu} &gt; 25</math> GeV</li> <li>• <math>m_T &gt; 40</math> GeV</li> <li>• <math> \eta_\ell  &lt; 2.5</math></li> <li>• <math>p_{T_\ell} &gt; 25</math> GeV</li> </ul>								
Total	<ul style="list-style-type: none"> <li>• Separately <math>W^+</math>, <math>W^-</math> and <math>W^+ + W^-</math></li> <li>• No further cuts</li> </ul>								
Combined Differential $W \rightarrow \ell\nu$									
	<ul style="list-style-type: none"> <li>• Separately <math>W^+</math> and <math>W^-</math></li> <li>• <math>p_{T,\nu} &gt; 25</math> GeV</li> <li>• <math>m_T &gt; 40</math> GeV</li> <li>• <math>p_{T_\ell} &gt; 25</math> GeV</li> <li>• <math>d\sigma/d \eta_\ell </math> in 11 <math> \eta_\ell </math> bins:  <math> \eta_\ell  : 0.0, 0.21, 0.42, 0.63, 0.84, 1.05, 1.37, 1.52, 1.74, 1.95, 2.18, 2.5</math></li> <li>• <math>d\sigma/d \eta_\ell  dp_{T,\ell}</math> in <math>11 \times 7</math> <math> \eta_\ell  \times p_{T,\ell}</math> bins for <math>p_{T,\ell} &gt; 20</math> GeV:  <math> \eta_\ell  : 0.0, 0.21, 0.42, 0.63, 0.84, 1.05, 1.37, 1.52, 1.74, 1.95, 2.18, 2.5</math>  <math>p_{T,\ell} : 20, 25, 30, 35, 40, 45, 50, \infty</math> [ GeV ]</li> </ul>								
Combined Integrated $Z \rightarrow \ell\ell$									
Central Fiducial	<ul style="list-style-type: none"> <li>• Both <math>p_{T,\ell} &gt; 20</math> GeV</li> <li>• Both <math> \eta  &lt; 2.5</math></li> <li>• 1 + 4 mass bins: <ul style="list-style-type: none"> <li>– <math>m_{\ell\ell} = 66 - 116</math> GeV</li> <li>– <math>m_{\ell\ell} = 66 - 76 - 91 - 106 - 116</math> GeV</li> </ul> </li> </ul>								
Forward Fiducial	<ul style="list-style-type: none"> <li>• Both <math>p_{T,\ell} &gt; 20</math> GeV</li> <li>• One <math> \eta  &lt; 2.5</math>, other <math>2.5 &lt;  \eta  &lt; 4.9</math></li> <li>• 2 mass bins <math>m_{\ell\ell} = 66 - 116 - 150</math> GeV</li> </ul>								
Total	<ul style="list-style-type: none"> <li>• 1 + 4 mass bins: <ul style="list-style-type: none"> <li>– <math>m_{\ell\ell} = 66 - 116</math> GeV</li> <li>– <math>m_{\ell\ell} = 66 - 76 - 91 - 106 - 116</math> GeV</li> </ul> </li> </ul>								
Combined Differential $Z \rightarrow \ell\ell$									
	<ul style="list-style-type: none"> <li>• Both <math>p_{T,\ell} &gt; 20</math> GeV</li> <li>• extrapolated to all <math>\eta_\ell</math>, i.e. no <math>\eta_\ell</math> cuts</li> <li>• <math>d\sigma/d y_{\ell\ell}  dm_{\ell\ell}</math>: <table border="1" style="margin-left: 20px;"> <thead> <tr> <th><math>m_{\ell\ell}</math> [ GeV ]</th> <th><math> y_{\ell\ell} </math></th> </tr> </thead> <tbody> <tr> <td>46–66</td> <td>0, 0.4, 0.8, 1.2, 1.6, 2.0, 2.4 (6 bins)</td> </tr> <tr> <td>66–116</td> <td>0, 0.2, 0.4, 0.6, 0.8, 1.0, 1.2, 1.4, 1.6, 1.8, 2.0, 2.2, 2.4, 2.8, 3.2, 3.6 (15 bins)</td> </tr> <tr> <td>116–150</td> <td>0, 0.4, 0.8, 1.2, 1.6, 2.0, 2.4, 2.8, 3.2, 3.6 (9 bins)</td> </tr> </tbody> </table> </li> </ul>	$m_{\ell\ell}$ [ GeV ]	$ y_{\ell\ell} $	46–66	0, 0.4, 0.8, 1.2, 1.6, 2.0, 2.4 (6 bins)	66–116	0, 0.2, 0.4, 0.6, 0.8, 1.0, 1.2, 1.4, 1.6, 1.8, 2.0, 2.2, 2.4, 2.8, 3.2, 3.6 (15 bins)	116–150	0, 0.4, 0.8, 1.2, 1.6, 2.0, 2.4, 2.8, 3.2, 3.6 (9 bins)
$m_{\ell\ell}$ [ GeV ]	$ y_{\ell\ell} $								
46–66	0, 0.4, 0.8, 1.2, 1.6, 2.0, 2.4 (6 bins)								
66–116	0, 0.2, 0.4, 0.6, 0.8, 1.0, 1.2, 1.4, 1.6, 1.8, 2.0, 2.2, 2.4, 2.8, 3.2, 3.6 (15 bins)								
116–150	0, 0.4, 0.8, 1.2, 1.6, 2.0, 2.4, 2.8, 3.2, 3.6 (9 bins)								

**Table C.2:** Complete list of combined measurements considered for all the  $W \rightarrow \ell\nu$  and  $Z \rightarrow \ell\ell$  channels.

## D References

- [1] R. P. Feynman, *Very High-Energy Collisions of Hadrons*, *Phys. Rev. Lett.* **23** (1969) 1415–1417. <http://link.aps.org/doi/10.1103/PhysRevLett.0B23.1415>. 3
- [2] J. D. Bjorken and E. A. Paschos, *Inelastic Electron-Proton and  $\gamma$ -Proton Scattering and the Structure of the Nucleon*, *Phys. Rev.* **185** (1969) 1975–1982. <http://link.aps.org/doi/10.1103/PhysRev.185.1975>. 3
- [3] S. D. Drell and T.-M. Yan, *Massive Lepton-Pair Production in Hadron-Hadron Collisions at High Energies*, *Phys. Rev. Lett.* **25** (1970) 316–320. <http://link.aps.org/doi/10.1103/PhysRevLett.25.316>. 3
- [4] F. Halzen and A. D. Martin, *Quarks and Leptons*. Wiley, 1984. 4
- [5] G. Miller, E. D. Bloom, G. Buschhorn, D. H. Coward, H. DeStaabler, J. Drees, C. L. Jordan, L. W. Mo, R. E. Taylor, J. I. Friedman, G. C. Hartmann, H. W. Kendall, and R. Verdier, *Inelastic Electron-Proton Scattering at Large Momentum Transfers and the Inelastic Structure Functions of the Proton*, *Phys. Rev. D* **5** (1972) 528–544. <http://link.aps.org/doi/10.1103/PhysRevD.5.528>. 4
- [6] Particle Data Group Collaboration, *Review of Particle Physics*, *Phys. Rev. D* **86** (2012) 010001. <http://link.aps.org/doi/10.1103/PhysRevD.86.010001>. 4
- [7] C. G. Callan and D. J. Gross, *High-Energy Electroproduction and the Constitution of the Electric Current*, *Phys. Rev. Lett.* **22** (1969) 156–159. <http://link.aps.org/doi/10.1103/PhysRevLett.22.156>. 6
- [8] D. Griffiths, *Introduction to Elementary Particles*. Wiley-VCH, 2nd ed., Oct., 2008. <http://www.worldcat.org/isbn/3527406018>. vii, 6
- [9] A. Bodek, M. Breidenbach, D. Dubin, J. Elias, J. I. Friedman, et al., *Experimental Studies of the Neutron and Proton Electromagnetic Structure Functions*, *Phys.Rev.* **D20** (1979) 1471–1552. vii, 6
- [10] D. J. Gross and F. Wilczek, *Asymptotically Free Gauge Theories. I*, *Phys. Rev. D* **8** (1973) 3633–3652. <http://link.aps.org/doi/10.1103/PhysRevD.8.3633>. 6
- [11] S. Camarda, *Measurement of  $Z/\gamma^* + \text{Jets}$  Differential Cross Sections with the CDF Detector at  $\sqrt{s} = 1.96 \text{ TeV}$* . 7
- [12] S. Bethke, *The 2009 World Average of  $\alpha(s)$* , *Eur.Phys.J.* **C64** (2009) 689–703, [arXiv:0908.1135](https://arxiv.org/abs/0908.1135) [hep-ph]. vii, 8

- 
- [13] R. Placakyte, for the H1 Collaboration, and for the ZEUS Collaboration, *Parton Distribution Functions*, ArXiv e-prints (2011), [arXiv:1111.5452](https://arxiv.org/abs/1111.5452) [hep-ph]. 8
- [14] G. Altarelli and G. Parisi, *Asymptotic Freedom in Parton Language*, *Nucl.Phys.* **B126** (1977) 298. 8
- [15] V. Gribov and L. Lipatov, *Deep inelastic  $e p$  scattering in perturbation theory*, *Sov.J.Nucl.Phys.* **15** (1972) 438–450. 8
- [16] Y. L. Dokshitzer, *Calculation of the Structure Functions for Deep Inelastic Scattering and  $e^+ e^-$  Annihilation by Perturbation Theory in Quantum Chromodynamics.*, *Sov.Phys.JETP* **46** (1977) 641–653. 8
- [17] M. Aharrouche, A. Arbuzov, D. Bardin, et al., *Double differential  $Z, W$  cross sections and their ratios in the electron channels*, Tech. Rep. ATL-COM-PHYS-2010-325, CERN, Geneva, Jun, 2010. 11
- [18] ALEPH Collaboration, DELPHI Collaboration, L3 Collaboration, OPAL Collaboration, SLD Collaboration, LEP Electroweak Working Group, SLD Electroweak Group, SLD Heavy Flavour Group Collaboration, *Precision electroweak measurements on the  $Z$  resonance*, *Phys.Rept.* **427** (2006) 257–454, [arXiv:hep-ex/0509008](https://arxiv.org/abs/hep-ex/0509008) [hep-ex]. vii, 14
- [19] ATLAS Collaboration, *Measurement of the inclusive  $W^\pm$  and  $Z/\gamma^*$  cross sections in the  $e$  and  $\mu$  decay channels in  $pp$  collisions at  $\sqrt{s} = 7$  TeV with the ATLAS detector*, *Phys. Rev. D* **85** (2012) 072004. <http://link.aps.org/doi/10.1103/PhysRevD.85.072004>. 14, 87
- [20] CMS Collaboration, *Measurement of the differential and double-differential Drell-Yan cross sections in proton-proton collisions at  $\sqrt{s} = 7$  TeV*, *Journal of High Energy Physics* **2013** (2013). [http://dx.doi.org/10.1007/JHEP12\(2013\)030](http://dx.doi.org/10.1007/JHEP12(2013)030). 17
- [21] R. Gavin, Y. Li, F. Petriello, and S. Quackenbush, *FEWZ 2.0: A code for hadronic  $Z$  production at next-to-next-to-leading order*, *Comput.Phys.Commun.* **182** (2011) 2388–2403, [arXiv:1011.3540](https://arxiv.org/abs/1011.3540) [hep-ph]. 17, 53
- [22] T. Sjostrand, S. Mrenna, and P. Z. Skands, *PYTHIA 6.4 Physics and Manual*, *JHEP* **05** (2006) 026, [arXiv:hep-ph/0603175](https://arxiv.org/abs/hep-ph/0603175). 18
- [23] G. Corcella et al., *HERWIG 6.5: an event generator for Hadron Emission Reactions With Interfering Gluons (including supersymmetric processes)*, *JHEP* **01** (2001) 010, [arXiv:hep-ph/0011363](https://arxiv.org/abs/hep-ph/0011363). 18

- [24] P. Nason, *A New method for combining NLO QCD with shower Monte Carlo algorithms*, *JHEP* **0411** (2004) 040, [arXiv:hep-ph/0409146](#) [hep-ph]. 18
- [25] S. Frixione, P. Nason, and C. Oleari, *Matching NLO QCD computations with Parton Shower simulations: the POWHEG method*, *JHEP* **0711** (2007) 070, [arXiv:0709.2092](#) [hep-ph]. 18
- [26] S. Alioli, P. Nason, C. Oleari, and E. Re, *NLO vector-boson production matched with shower in POWHEG*, *JHEP* **0807** (2008) 060, [arXiv:0805.4802](#) [hep-ph]. 18
- [27] S. Alioli, P. Nason, C. Oleari, and E. Re, *A general framework for implementing NLO calculations in shower Monte Carlo programs: the POWHEG BOX*, *JHEP* **1006** (2010) 043, [arXiv:1002.2581](#) [hep-ph]. 18
- [28] S. Frixione and B. R. Webber, *Matching NLO QCD computations and parton shower simulations*, *JHEP* **06** (2002) 029, [arXiv:hep-ph/0204244](#). 18
- [29] E. Boos, M. Dobbs, W. Giele, I. Hinchliffe, J. Huston, et al., *Generic user process interface for event generators*, [arXiv:hep-ph/0109068](#) [hep-ph]. 18
- [30] L. Evans and P. Bryant, *LHC Machine*, *Journal of Instrumentation* **3** no. 08, (2008) S08001. <http://stacks.iop.org/1748-0221/3/i=08/a=S08001>. 19
- [31] ATLAS Collaboration, *ATLAS detector and physics performance: Technical Design Report, 1*. Technical Design Report ATLAS. CERN, Geneva, 1999. Electronic version not available. 20
- [32] CMS Collaboration, *CMS Physics: Technical Design Report Volume 1: Detector Performance and Software*. Technical Design Report CMS. CERN, Geneva, 2006. 20
- [33] CMS Collaboration, *CMS Physics: Technical Design Report Volume 2: Physics Performance*, *J. Phys. G* **34** no. CERN-LHCC-2006-021. CMS-TDR-8-2, (2006) 995–1579. 669 p. revised version submitted on 2006-09-22 17:44:47. 20
- [34] LHCb Collaboration, *LHCb : Technical Proposal*. Tech. Proposal. CERN, Geneva, 1998. 20
- [35] ALICE Collaboration, *ALICE: Technical proposal for a Large Ion collider Experiment at the CERN LHC*. LHC Tech. Proposal. CERN, Geneva, 1995. 20
- [36] Wikipedia, “Cern accelerator complex.” <http://en.wikipedia.org/wiki/File:Cern-accelerator-complex.svg>. Accessed: 2014-01-08. 20

- 
- [37] M. Benedikt, P. Collier, V. Mertens, J. Poole, and K. Schindl, *LHC Design Report*. CERN, Geneva, 2004. 20
- [38] ATLAS Collaboration, *Improved luminosity determination in pp collisions at  $\sqrt{s} = 7$  TeV using the ATLAS detector at the LHC*, [arXiv:1302.4393](https://arxiv.org/abs/1302.4393) [hep-ex]. 20, 33
- [39] J. Pequeno, “Computer generated image of the whole atlas detector.” Mar, 2008. viii, 22
- [40] M. Aleksa, F. Bergsma, L. Chevalier, et al., *Results of the ATLAS solenoid magnetic field map*, Journal of Physics: Conference Series **110** no. 9, (2008) 092018. <http://stacks.iop.org/1742-6596/110/i=9/a=092018>. 23
- [41] J. Pequeno, “Computer generated image of the atlas inner detector.” Mar, 2008. viii, 24
- [42] G. Aad, M. Ackers, F. Alberti, et al., *ATLAS pixel detector electronics and sensors*, Journal of Instrumentation **3** no. 07, (2008) P07007. <http://stacks.iop.org/1748-0221/3/i=07/a=P07007>. 25
- [43] ATLAS TRT Collaboration Collaboration, *The ATLAS transition radiation tracker*, [arXiv:hep-ex/0311058](https://arxiv.org/abs/hep-ex/0311058) [hep-ex]. 25
- [44] J. Pequeno, “Computer generated image of the atlas calorimeter.” Mar, 2008. viii, 27
- [45] *ATLAS liquid-argon calorimeter: Technical Design Report*. Technical Design Report ATLAS. CERN, Geneva, 1996. 28
- [46] A. Succurro, *The {ATLAS} Tile Hadronic Calorimeter performance in the {LHC} Collision Era*, *Physics Procedia* **37** no. 0, (2012) 229 – 237. <http://www.sciencedirect.com/science/article/pii/S1875389212016835>. <ce:title>Proceedings of the 2nd International Conference on Technology and Instrumentation in Particle Physics (TIPP 2011)</ce:title>. 29
- [47] J. Pequeno, “Computer generated image of the atlas muons subsystem.” Mar, 2008. viii, 30
- [48] *ATLAS Trigger Performance: Status Report*, Tech. Rep. CERN-LHCC-98-015, CERN, Geneva, Jun, 1998. 30
- [49] ATLAS Collaboration, *Improved luminosity determination in pp collisions at  $\sqrt{s} = 7$  TeV using the ATLAS detector at the LHC*, [arXiv:1302.4393](https://arxiv.org/abs/1302.4393) [hep-ex]. 34

- [50] *Performance of the ATLAS Electron and Photon Trigger in p-p Collisions at  $\sqrt{s} = 7$  TeV in 2011*, Tech. Rep. ATLAS-CONF-2012-048, CERN, Geneva, May, 2012. 38
- [51] A. Internal, “Electron reconstruction.” <https://twiki.cern.ch/twiki/bin/viewauth/AtlasProtected/ElectronReconstruction>. Accessed: 2014-01-09. 39
- [52] ATLAS Collaboration, *Electron performance measurements with the ATLAS detector using the 2010 LHC proton-proton collision data*, *Eur.Phys.J.* **C72** (2012) 1909, [arXiv:1110.3174](https://arxiv.org/abs/1110.3174) [hep-ex]. 40, 45, 46, 68
- [53] N. Lorenzo, D. Fournier, E. Richter-Was, and D. Froidevaux, *Various Reports on electron efficiency loss for  $1.65 < |\eta| < 1.70$* , tech. rep., 2011-2012. <http://indico.cern.ch/getFile.py/access?contribId=1&resId=0&materialId=slides&confId=205024>. 46
- [54] ATLAS Collaboration, *Measurement of angular correlations in Drell-Yan lepton pairs to probe  $Z/\gamma^*$  boson transverse momentum at  $\sqrt{s}=7$  TeV with the ATLAS detector*, *Phys.Lett.* **B720** (2013) 32–51, [arXiv:1211.6899](https://arxiv.org/abs/1211.6899) [hep-ex]. 49
- [55] J. Kretzschmar and L. Ionomidou-Fayard, *Electron performances measurements using the 2011 LHC proton-proton collisions*, Tech. Rep. ATL-COM-PHYS-2012-1024, CERN, Geneva, Jul, 2012. This is a draft of the CONF Note. 50
- [56] S. Moch and P. Uwer, *Heavy-quark pair production at two loops in QCD*, *Nucl.Phys.Proc.Suppl.* **183** (2008) 75–80, [arXiv:0807.2794](https://arxiv.org/abs/0807.2794) [hep-ph]. 53
- [57] U. Langenfeld, S. Moch, and P. Uwer, *New results for  $t$  anti- $t$  production at hadron colliders*, [arXiv:0907.2527](https://arxiv.org/abs/0907.2527) [hep-ph]. 53
- [58] ATLAS Collaboration, *Measurement of the top quark pair production cross section in  $pp$  collisions at  $\sqrt{s} = 7$  TeV in dilepton final states with ATLAS*, *Phys.Lett.* **B707** (2012) 459–477, [arXiv:1108.3699](https://arxiv.org/abs/1108.3699) [hep-ex]. 53
- [59] S. Schmitt, *Measurement of the Inclusive  $pp \rightarrow Z/\gamma^* \rightarrow e^+e^-$  Cross Section at  $\sqrt{s} = 7$  TeV with the ATLAS Experiment and Design Studies for a First Level Track Trigger for the ATLAS Trigger Upgrade at the future High Luminosity LHC.*, 54
- [60] ATLAS Collaboration, *Unfolding in ATLAS*, [arXiv:1104.2962](https://arxiv.org/abs/1104.2962) [hep-ex]. 61
- [61] K. Bierwagen, *Bayesian Unfolding*, in *Proc. Workshop on Statistical Issues Related to Discovery Claims in Search Experiments and Unfolding (PHYSTAT 2011)*, H. B. Prosper and L. Lyons, eds. CERN, Geneva, 2011. 61

- 
- [62] J. Kretzschmar, L. Iconomidou-Fayard, et al., *Supporting document on electron performance measurements using the 2011 LHC proton-proton collisions*, <https://cdsweb.cern.ch/record/1461217>. This is the draft of the supporting document. 67
- [63] A. e/gamma Combined Performance Group, ‘‘Energy scale and resolution recommendations.’’ <https://twiki.cern.ch/twiki/bin/viewauth/AtlasProtected/EnergyScaleResolutionRecommendations>. Accessed: 2010-09-30. 68
- [64] H.-L. Lai, M. Guzzi, J. Huston, Z. Li, P. M. Nadolsky, J. Pumplin, and C.-P. Yuan, *New parton distributions for collider physics*, *Phys. Rev. D* **82** (2010) 074024. <http://link.aps.org/doi/10.1103/PhysRevD.82.074024>. 69, 71, 76
- [65] J. Kretzschmar, M. Bellomo, et al., *Supporting document on ATLAS W and Z inclusive cross section measurements with 2011 data*, <https://cds.cern.ch/record/1517987>. This is the draft of the supporting document. 71
- [66] P. M. Nadolsky, H.-L. Lai, Q.-H. Cao, J. Huston, J. Pumplin, et al., *Implications of CTEQ global analysis for collider observables*, *Phys.Rev.* **D78** (2008) 013004, [arXiv:0802.0007](https://arxiv.org/abs/0802.0007) [hep-ph]. 75
- [67] J. Gao, M. Guzzi, J. Huston, H.-L. Lai, Z. Li, et al., *The CT10 NNLO Global Analysis of QCD*, [arXiv:1302.6246](https://arxiv.org/abs/1302.6246) [hep-ph]. 76
- [68] S. Alekhin, J. Blumlein, and S. Moch, *Parton Distribution Functions and Benchmark Cross Sections at NNLO*, *Phys.Rev.* **D86** (2012) 054009, [arXiv:1202.2281](https://arxiv.org/abs/1202.2281) [hep-ph]. 77
- [69] H1 and ZEUS Collaboration Collaboration, *Combined Measurement and QCD Analysis of the Inclusive  $e^+ - p$  Scattering Cross Sections at HERA*, *JHEP* **1001** (2010) 109, [arXiv:0911.0884](https://arxiv.org/abs/0911.0884) [hep-ex]. 77
- [70] H1 and ZEUS Collaboration, *Hera Precision Measurements and Impact for LHC Predictions*, [arXiv:1107.4193](https://arxiv.org/abs/1107.4193) [hep-ex]. HERAPDF 1.5 NLO and NNLO preliminary, H1prelim-10-142, ZEUS-prel-10-018, H1prelim-11-042, ZEUS-prel-11-002, Proceedings of Moriond 2011. 77
- [71] A. Martin, W. Stirling, R. Thorne, and G. Watt, *Parton distributions for the LHC*, *Eur.Phys.J.* **C63** (2009) 189–285, [arXiv:0901.0002](https://arxiv.org/abs/0901.0002) [hep-ph]. 77

- [72] A. Martin, A. T. Mathijssen, W. Stirling, R. Thorne, B. Watt, et al., *Extended Parameterisations for MSTW PDFs and their effect on Lepton Charge Asymmetry from W Decays*, *Eur.Phys.J.* **C73** (2013) 2318, [arXiv:1211.1215 \[hep-ph\]](#). 77
- [73] R. D. Ball, V. Bertone, S. Carrazza, C. S. Deans, L. Del Debbio, et al., *Parton distributions with LHC data*, *Nucl.Phys.* **B867** (2013) 244–289, [arXiv:1207.1303 \[hep-ph\]](#). 77
- [74] P. Jimenez-Delgado and E. Reya, *Dynamical NNLO parton distributions*, *Phys. Rev.* **D79** (2009) 074023, [arXiv:0810.4274 \[hep-ph\]](#). 77
- [75] ATLAS Collaboration, *Determination of the strange quark density of the proton from ATLAS measurements of the  $W \rightarrow l\nu$  and  $Z \rightarrow ll$  cross sections*, *Phys.Rev.Lett.* **109** (2012) 012001, [arXiv:1203.4051 \[hep-ex\]](#). 77, 96
- [76] A. Lewis, “ $W \rightarrow e\nu$  results.” Private Communication, 2014. 78
- [77] S. Schmitt, “ $Z \rightarrow ee$  results.” Private Communication, 2014. 78
- [78] M. Bellomo, “ $Z \rightarrow \mu\mu$  results.” Private Communication, 2014. 78
- [79] A. Kapliy, “ $W \rightarrow \mu\nu$  results.” Private Communication, 2014. 78
- [80] A. Glazov, *Averaging of DIS cross section data*, *AIP Conf. Proc.* **792** (2005) 237–240. 78
- [81] L. Dixon, “Vrap.” <http://www.slac.stanford.edu/~lance/Vrap/>. Accessed: 2014-01-19. 102

## Acknowledgements

I would like to extend my sincere thanks to my supervisor, Dr. Sasha Glazov, firstly for the extensive guidance and support throughout my PhD, and secondly for the opportunity to work under his supervision at DESY.

Bei Prof. Dr. Peter Schleper, bedanke ich mich für die Übernahme des Zweitgutachtens der Dissertation. My sincere thanks go to Prof. Dr. Erika Garutti, for refereeing my defence.

I would like to express my deepest gratitude in particular to my former officemate and good friend Dr. Mikhail Karnevskiy, who was always willing to answer my naive questions.

This work would not have been possible without the continuing patience of Dr. Sebastian Schmitt and his clear explanations, in particular with regards to the analysis software, and his guidance with regards to the analysis itself.

I thank also my colleagues in the ZeeD working group: Dr. Stefano Camarda, Dr. Voica Radescu, Dr. Pavel Starovoitov, Dr. Stanislav Shushkevich, Elena Yatsenko, George Sedov, Nataliia Kondrashova, and others, for the productive and stimulating discussions and working environment.

I would like to acknowledge my colleagues in the ATLAS group at DESY for the productive environment, stimulating discussions, and for their friendship, which has made working at DESY an extremely enjoyable experience.

I would like to thank all the members of the W, Z inclusive cross section group for the enjoyable working environment. Special thanks go to Dr. Jan Kretzschmar and Dr. Massimiliano Bellomo. Their guidance and support have made the analyses in this thesis possible.

My thanks go also to the members of the  $e/\gamma$  working group at CERN, and the members of the calibration subgroup, with whom I performed my authorship qualification work in ATLAS.

I thank the generous souls who acted as proofreaders and fact-checkers for this thesis! In no particular order: Misha K., Misha Lisovyi, Stefano C., and Phillip Hamnett.

I sincerely thank Dr. Barry King and Prof. Max Klein at the University of Liverpool for their encouragement and belief, without which I could not have come to DESY.

This analysis would not have been possible without the extremely generous support throughout my education from the Isle of Man Department of Education, and I wish to thank them sincerely.

To Dr. Anna Henrichs, for starting it all. For the first opportunity to work in Germany, and the first opportunity to work at CERN, and the many interesting and enjoyable talks on physics, football, music, and many other things. I owe you a huge debt of gratitude.

I thank my family, for the constant support through difficult times, and through good times. Thank you, Babbas, George, Beth, and Tracey.

Lastly, Ginni, I couldn't have done any of it without you. Thank you for being there for me, and inspiring me always.